

# Charge and Spin Fractionalization in Strongly Correlated 1D Systems

Von der Fakultät Mathematik und Physik der Universität Stuttgart

zur Erlangung der Würde eines

Doktors der Naturwissenschaften (Dr. rer. nat.)

genehmigte Abhandlung

Vorgelegt von

**Alexander Moreno**

aus Caracas (Venezuela)

Hauptberichter: Prof. Dr. rer. nat. Alejandro Muramatsu

Mitberichter: Prof. Dr. rer. nat. Günter Wunner

Tag der mündlichen Prüfung: 9. Juli 2013

Institut für Theoretische Physik III

2013



# Contents

<b>Zusammenfassung</b>	<b>7</b>
<b>1 Introduction</b>	<b>11</b>
<b>2 Luttinger Liquids</b>	<b>15</b>
2.1 Special features of 1D fermionic systems . . . . .	15
2.2 The Tomonaga-Luttinger model . . . . .	16
2.3 Effective quantum field theory . . . . .	19
2.4 Correlation functions and phase diagram . . . . .	21
2.5 One-particle spectral function . . . . .	22
2.6 Charge and spin fractionalization . . . . .	23
<b>3 The Density Matrix Renormalization Group Method</b>	<b>25</b>
3.1 Static DMRG . . . . .	28
3.1.1 Infinite DMRG . . . . .	28
3.1.2 Recursive relations for the Hamiltonian . . . . .	30
3.1.3 Quantum numbers conservation and the reduced density matrix . . . . .	36
3.1.4 Finite DMRG Algorithm . . . . .	39
3.1.5 Measurements and correlation functions . . . . .	42
3.2 Time-dependent DMRG . . . . .	43
3.2.1 Preparing the initial state for the time evolution . . . . .	45
<b>4 Ground-State Phase Diagram</b>	<b>49</b>
4.1 Metallic phase . . . . .	51
4.2 Singlet-superconductivity and spin-gap phase . . . . .	53
4.3 Phase separation . . . . .	54
4.4 Correlation functions and density in real space . . . . .	56
4.4.1 Structure factors . . . . .	56
4.4.2 Gapless superconducting phase . . . . .	60
4.4.3 Competing orders in the spin-gap phase. Charge density wave vs singlet superconductivity . . . . .	62
4.4.4 Phase separation and electron solid phase . . . . .	65
<b>5 Real-Time Dynamics</b>	<b>67</b>
5.1 Bethe-Ansatz . . . . .	67
5.1.1 Dispersion relations . . . . .	67
5.1.2 One-electron addition spectral function dispersion lines . . . . .	69
5.2 Time dependent DMRG simulations . . . . .	72

---

5.2.1	Validation of our t-DMRG code . . . . .	73
5.2.2	Supersymmetric point $J = 2$ . . . . .	75
5.2.3	Away from the supersymmetric point $J = 2$ . . . . .	80
<b>6</b>	<b>Summary and Conclusions</b>	<b>83</b>
	<b>Appendices</b>	<b>87</b>
<b>A</b>	<b>DMRG Method</b>	<b>89</b>
A.1	Optimization of the wave function . . . . .	89
A.2	Optimization of the entanglement . . . . .	90
<b>B</b>	<b>Creating the Gaussian Wavepacket</b>	<b>93</b>
B.1	Evolution of the wavepacket . . . . .	93
B.1.1	The state $c_k^\dagger G\rangle$ as a linear combination of wavepackets . . . . .	94
B.1.2	The state $c_k^\dagger G\rangle$ as a two parametric eigenstate of $H$ . . . . .	95
	<b>Acknowledgments</b>	<b>101</b>
	<b>Curriculum Vitae</b>	<b>103</b>

# List of Figures

1.1	Graphical picture of the kinetic and interacting term of the Hamiltonian 1.1. . . . .	12
2.1	Particle-hole excitation spectrum $\epsilon_{ph}(q)$ for the case of non-interacting fermions . . .	16
2.2	Linearized dispersion of the Tomonaga-Luttinger (TL) model. . . . .	17
2.3	Important low-energy interacting processes of any gapless fermionic system. . . . .	18
2.4	Phase diagram of the Hamiltonian (2.9) with isotropic couplings $g_{i\parallel} = g_{i\perp}$ . . . . .	22
2.5	One-particle spectral function $A(k, \omega)$ for a fixed $k$ such that $(k - k_F) > 0$ . . . . .	23
2.6	Schematic representation of charge and spin fractionalization in LL . . . . .	24
3.1	One dimensional chain. . . . .	25
3.2	The one-dimensional chain of atoms is divided into two parts. . . . .	26
3.3	The system is divided into 4 subspaces: . . . . .	28
3.4	The new left block and the new right block. . . . .	29
3.5	Change of the superblock going from one DMRG step to the next one. . . . .	30
3.6	Splitting of the Hamiltonian considering only nearest neighbor interactions. . . . .	31
3.7	Splitting of the Hamiltonian $H_F^{(l+1)}$ . . . . .	32
3.8	Splitting of the Hamiltonian $H_R^{(l+1)}$ . . . . .	34
3.9	$H_{FS1}$ acts only on the sites $ S_j\rangle_l$ and $ S_\beta\rangle_{l+1}$ . . . . .	35
3.10	Block diagonal form of the reduced density matrix. . . . .	38
3.11	The right-left sweep immediately after the infinite algorithm. . . . .	40
3.12	The left-right sweep. . . . .	40
3.13	The right-left sweep. . . . .	41
3.14	Relative error $\Delta e$ given by Eq. (3.52) as function of the sweep. . . . .	42
3.15	We divide the lattice into odd (blue) and even (red) bonds. . . . .	43
3.16	Relative deviations $\Delta H$ and $\Delta N$ of the energy and particle number . . . . .	47
3.17	Error estimation of the charge (full-black line) and spin (red-dashed line) densities . . . . .	47
4.1	Phase diagram of the 1D $t$ - $J$ model from DMRG . . . . .	50
4.2	Structure factor $N(k)$ of the density-density correlation function . . . . .	51
4.3	Extrapolation to the thermodynamic limit of $N(k = 2\pi/40)$ for $n = 0.5$ and $J = 2.0$ . . . . .	52
4.4	$K_\rho$ as function of $J$ for different densities $n$ . . . . .	52
4.5	$K_\rho$ as function of the density $n$ for $J = 2$ (supersymmetric point). . . . .	52
4.6	Regions with different Luttinger parameters $K_\rho(n, J)$ . . . . .	53
4.7	Energy comparison between systems containing four, six and eight particles . . . . .	53
4.8	$\Delta E_S$ vs $1/L$ for $n = 0.2$ and various values of $J$ . . . . .	54
4.9	Spin gap $\Delta E_S$ in the thermodynamic limit as a function of $J$ . . . . .	55
4.10	Spin gap $\Delta E_S$ in the thermodynamic limit as a function of $n$ for $J = 2.1 - 2.8$ . . . . .	55
4.11	Inverse of the compressibility $\kappa^{-1}$ . . . . .	55

4.12	Zoom of Fig. 4.11. . . . .	56
4.13	Structure factor $N(k)$ for the density-density correlation function . . . . .	57
4.14	Structure factor $S(k)$ for the spin-spin correlation function . . . . .	58
4.15	Structure factor $P_S(k)$ for the singlet-pair-pair correlation function . . . . .	59
4.16	Momentum distribution function $n(k)$ . . . . .	60
4.17	Singlet $P_S(x)$ and triplet $P_T(x)$ correlation functions . . . . .	61
4.18	Singlet $P_S(x)$ and triplet $P_T(x)$ correlation functions . . . . .	61
4.19	Triplet and singlet pair-pair structure factors for $n = 0.5$ , $J = 2.6$ and $L = 200$ . . . . .	62
4.20	Maxima of $P_S(x)$ and $-N(x)$ in real space . . . . .	62
4.21	Scaling of $P_S(k = 0)$ in the thermodynamic limit . . . . .	63
4.22	Density in real space $\rho(x)$ for $n = 0.1$ and (a): $L = 80$ , (b): $L = 160$ . . . . .	63
4.23	Density in real space $\rho(x)$ for $n = 0.1$ , $L = 160$ and different values of $J$ . . . . .	64
4.24	Magnetic structure factor $S(k)$ in the phase-separated region . . . . .	65
4.25	Phase diagram of Fig. 4.1 including the electron solid phase (ES). . . . .	66
5.1	Solution of the dispersion relations (5.1) and (5.2) . . . . .	69
5.2	Lines where $A(k, \omega)$ have divergences . . . . .	71
5.3	Non-interacting spinless fermions for $L = 160$ . . . . .	74
5.4	Charge (black-full line) and the spin (red-dashed line) densities given by Eq. (5.28). . . . .	75
5.5	Charge (black-full line) and spin (red-dashed line) densities given by Eq. (5.28) . . . . .	76
5.6	Charge (black-full line) and the spin (red-dashed line) densities given by Eq. (5.28) . . . . .	76
5.7	Charge density (color scale) as function of time and space for $n = 0.6$ and $k = 0.70\pi$ . . . . .	77
5.8	Derivative $v(k) = \partial\omega(k)/\partial k$ of the Bethe-Ansatz spectral lines . . . . .	77
5.9	Locus of the highest weight features of the electron addition . . . . .	78
5.10	Time evolution of $\rho_s(x_i, \tau)$ for a wavepacket initially at $x = 0$ , . . . . .	79
5.11	(a): Charge and the spin densities. (b): Charge $Q$ of the different wavepackets . . . . .	79
5.12	Fractionalized wavepackets for different values of $J/t$ away from the SUSY point . . . . .	80
5.13	As in Fig. 5.8 but for $J = 1.75$ and $J = 2.25$ . . . . .	81
5.14	Fractionalized wavepackets at $J/t = 1$ , $n = 0.5$ , $\tau = 50$ and $L = 200$ . . . . .	81

# Zusammenfassung

Die Frage, ob die Eigenschaften oder fundamentalen Bausteine unseres Universums eine diskrete oder kontinuierliche Natur haben, hat Wissenschaftler und Philosophen schon immer fasziniert. Ein bekanntes Beispiel ist die elektrische Ladung. Michael Faraday (1791-1867) war der Erste, der die diskrete Natur der elektrischen Ladung mit Elektrolyse Experimenten bemerkt hat. Einige Jahre später hat Robert Milikan (1868-1953) diese Diskretheit mit seinem berühmten Öltropfenversuch nachgewiesen und konnte sogar den Wert der fundamentalen elektrischen Ladung abmessen, b.z. die Ladung des Elektrons. Obwohl es wahr ist, dass der Wert der elektrischen Ladung ein ganzzahliges Vielfaches der fundamentalen Ladung sein muss (ausgeschlossen sind die Quarks, die einen Bruchteil  $1/3$  oder  $2/3$  von der elektronischen Ladung haben und wegen Color Confinement noch nicht isoliert beobachtet wurden), gibt es Fälle in der Physik der kondensierten Materie, in denen man von Entitäten sprechen kann, die einen Bruchteil von der elektronischen Ladung tragen. Ein prominentes Beispiel ist der fraktionierte Quanten-Hall-Effekt bei einer Füllung von  $1/3$  [1]. Dabei sind die so genannten Laughlin Quasiteilchen mit einem Drittel der fundamentalen Ladung, die elementaren Anregungen des Systems. Ein anderes Beispiel ist der Fall von wechselwirkenden Elektronen in einer Dimension, wobei nicht nur eine Fraktionalisierung der Ladung in Bruchteile [2] stattfindet, sondern auch eine ganze Entkopplung der Spin- und Ladungsfreiheitsgrade [3].

Auf der anderen Seite hat sich die wichtige Rolle der Korrelationen in Vielteilchensystemen mehr als gut etabliert. Das meistzitierte Beispiel in der Literatur ist das Phänomen von Hochtemperatursupraleitung [4]. Es kann gesagt werden, dass die Entdeckung von Hochtemperatursupraleitung war (und ist vielleicht immer noch) die Hauptmotivation für das Studium von stark korreliertem Vielteilchensystemen. Eine gemeinsame Eigenschaft der Hochtemperatursupraleiter sind die Kupfer-Sauerstoff-Ebenen, auf denen die Supraleitung stattfindet. Von daher ist die Hochtemperatursupraleitung als ein zweidimensionales Problem zu betrachten. Ein Effektiv-Modell, das für die Beschreibung der Hochtemperatursupraleitung verwendet wird, ist das so genannte  $t$ - $J$  Modell, das eine Starke-Kopplung-Variante des Hubbard Modells darstellt [5, 6]. Das  $t$ - $J$  Modell wurde auch von Zhang und Rice aus einem Zweiband-Hubbard-Hamiltonoperator [7] abgeleitet. Das  $t$ - $J$  Modell ist immer noch eine echte theoretische Herausforderung und seine vollständige Lösung ist noch nicht bekannt. Um einige Einblicke in das Problem zu bekommen, kann man mit dem eindimensionalen ( $1D$ ) Problem starten, das durch den folgenden Hamiltonoperator gegeben ist:

$$H = -t \sum_{i,\sigma}^{L-1} \left( \tilde{c}_{i,\sigma}^\dagger \tilde{c}_{i+1,\sigma} + \text{h.c.} \right) + J \sum_i^{L-1} \left( \vec{S}_i \cdot \vec{S}_{i+1} - \frac{1}{4} n_i n_{i+1} \right). \quad (1)$$

Die Operatoren  $\tilde{c}_{i,\sigma}^\dagger$  ( $\tilde{c}_{i,\sigma}$ ) erzeugen (vernichten) ein Fermion mit Spin  $\sigma = \uparrow, \downarrow$  auf dem Gitterplatz  $i$ . Sie sind keine Kanonischen-Fermionischen-Operatoren, weil sie auf einem beschränkten Hilbertraum wirken, auf dem keine Doppelbesetzung von Gitterplätzen erlaubt ist.  $\vec{S}_i = (S_i^x, S_i^y, S_i^z) = \tilde{c}_{i,\alpha}^\dagger \vec{\sigma}_{\alpha\beta} \tilde{c}_{i,\beta}$  ist der Spinoperator und  $\vec{\sigma} = (\sigma_x, \sigma_y, \sigma_z)$  sind die Pauli-Matrizen.  $n_i = \tilde{c}_{i,\sigma}^\dagger \tilde{c}_{i,\sigma}$  ist der Dichteoperator und  $L$  ist die Zahl der Gitterplätze. Die erste Summe entspricht der kinetischen

Energie von Elektronen, die zwischen nächsten Nachbarn hüpfen. Die zweite Summe ist die Austauschwechselwirkung, die die Ausbildung von Singulett-Elektronen-Paaren begünstigt.  $t$  und  $J$  sind die jeweilige Kontrollparameter für jede Summe. Trotz der Einfachheit des  $1D$   $t$ - $J$  Hamiltonians, beinhaltet dieses Modell bereits exotische Grundzustandsphasen wie, z.B. Supraleitung, Phasentrennung und Spin Lücke, die auch in den Hochtemperatursupraleitern zu finden sind.

Abgesehen vom  $1D$ - $t$ - $J$  Modell, gibt es weitere Motivationen für die Untersuchung von stark korrelierten eindimensionalen Systemen. Auf der analytischen Seite, kann die Niedrig-Energiephysik von  $1D$  Systemen mittels einer effektiven Quatenfeldtheorie beschrieben werden, die so genannte Theorie der Luttinger Flüssigkeit (LL) [3]. Außerdem existieren  $1D$ -Modelle, die mit dem Bethe-Ansatz [8–11] exakt gelöst werden können. Auf der numerischen Seite gibt es sehr effiziente und genaue Techniken, die für das Studium von eindimensionalen Systemen geeignet sind, wie z.B die Dichtematrix Renormierungsgruppen (DMRG) Methode [12, 13]. Auf der experimentellen Seite gibt es viele Systeme, die eindimensionale Eigenschaften zeigen, wie. z.B Spin-Ladungsentkopplung [14–16] und Ladungsfractionalisierung [17, 18]. Darüberhinaus wird die experimentelle Realisierung von eindimensionalen Systemen durch die technische Entwicklung von Experimenten mit Quantum Nanodrähte [19] und kalte Atome in optischen Gittern immer leichter [20, 21]. Zusammen mit den experimentellen Fortschritten wurde auch eine theoretische Beschreibung in Zusammenhang mit der Erweiterung der LL-Theorie mittels der Betrachtung von einer nichtlinearen Dispersion erreicht, die qualitative Änderungen der Spektralfunktion [22–25] und der Relaxation-Vorgänge [18] von  $1D$  elektronischen Systemen mit sich bringt.

Das Hauptziel dieser Arbeit ist die Untersuchung der Spin und Ladungsfractionalisierung von einem injizierten Elektron in einem starken korrelierten System, im  $t$ - $J$  Modell. Zur Berechnung wurde die zeitabhängige DMRG Methode [26] verwendet. Um unsere Ergebnisse vergleichen und interpretieren zu können, haben wir die LL Theorie und die exakte Lösung des Bethe-Ansatzes am supersymmetrischen Punkt als analytischen Rahmen verwendet. Wir zeigen, dass Fractionalisierung der Ladung und des Spins bei hohen Energien stattfindet, die von der LL-Theorie nicht beschrieben werden kann.

Vor der Untersuchung der dynamischen Eigenschaften haben wir zuerst die Grundzustandseigenschaften des  $t$ - $J$  Modells mit der statischen DMRG Methode studiert. Die relevantesten Ergebnisse dieses Teiles der Arbeit sind der engültige Beweis für eine endliche Spin Lücke, die eine Quelle von Kontroversen zwischen verschiedenen Autoren war [27–29], und die genaue Bestimmung des Grundzustandsphasendiagramms durch Messungen von Energien und Korrelationen und nach einer Extrapolation zum thermodynamischen Limes. Während dieser Bestimmung haben wir die LL-Parameter abgeleitet. Diese werden für den Vergleich unserer dynamischen Simulationen mit der LL-Theorie hilfreich sein, weil der Bruchteil der Ladung oder des Spins eine Funktion von diesen Parametern ist, wie wir in Kapitel 5 sehen werden.

Der Inhalt dieser Arbeit ist wie folgt organisiert: In Kapitel 2 geben wir eine kurze Einführung in die LL-Theorie, die die Physik von eindimensionalen Quantensystemen bei niedrigen Energien beschreibt. Wir starten mit der Diskussion von einigen besonderen Eigenschaften der  $1D$  Systeme. Motiviert durch die Tatsache, dass bei verschwindendem Impuls und verschwindender Energie die Teilchen-Loch-Anregungen in einem  $1D$  freien System eine wohldefinierte Dispersionsrelation haben, wird das Tomonaga-Luttinger (TL) Modell eingeführt. Dieses Modell war in der Tat der Ausgangspunkt für die Entwicklung einer bosonischen Theorie. Mit einer Renormierungsgruppenanalyse können zwei verschiedene asymptotische Theorien abgeleitet werden: eine Spin-lückenlose  $\Delta_\sigma = 0$  Theorie, die sogenannte Theorie der Luttinger Flüssigkeit (LL), und eine  $\Delta_\sigma \neq 0$  Theorie, die sogenannte Luther-Emery-(LE) Theorie. Ein Phasendiagramm für allgemeine eindimensionale Systeme mit Spin-Rotationsinvarianz wird präsentiert. Zum Schluss wird die Einteilchen Spektralfunktion und die Spin- Ladungsfractionalisierung diskutiert.

In Kapitel 3 wird die Dichtematrix Renormierungsgruppen (DMRG) Methode [12,13,26,30] beschrieben, die wir für unsere numerische Simulationen angewendet haben. Diese Methode ist ein sehr leistungsfähiges Werkzeug bei der Untersuchung von eindimensionalen Quanten Problemen, womit größere Systeme als mit den konventionellen Techniken, wie exakte Diagonalisierung (ED) oder Lanczos [31], erreicht werden können. In diesem Kapitel starten wir mit einer kurzen Einführung von den Grundlagen der DMRG Methode und danach wird der Algorithmus ausführlicher erklärt. In wenigen Worten ist die DMRG Technik erfolgreich aufgrund einer hocheffizienten Reduzierung des Hilbertraumes, die dieses exponentielle Problem in ein polynomielles umwandelt. Dies ermöglicht, dass man mit der gleichen Rechenleistung im Vergleich zur ED oder Lanczos größere Systeme mit hoher Genauigkeit behandeln kann. Die DMRG Methode ist in zwei Hauptalgorithmen aufgeteilt: Die statische und die zeitabhängige DMRG. Die statische Methode ist der Kern des Algorithmus und der zeitabhängige Teil ist nur eine Erweiterung der ersten Methode. Desweiteren wird der wichtige Punkt diskutiert, dass unter Berücksichtigung der Erhaltung der gesamten Teilchenzahl und der gesamten Magnetisierung, eine zusätzliche Abnahme des Hilbertraumes ermöglicht wird. Wir erklären, wie Ein- und Zweipunktkorrelationen berechnet werden, die für die Bestimmung vom Grundzustandsphasendiagramm des  $t$ - $J$  Modells von Bedeutung sind. Wir schließen dieses Kapitel mit der Diskussion über den zeitabhängigen DMRG-(t-DMRG) Algorithmus.

In Kapitel 4 wird die statische DMRG angewendet, um durch Messungen von Energie und Korrelationsfunktionen die Phasen des eindimensionalen  $t$ - $J$  Modells zu untersuchen [32, 33]. Vier verschiedene Phasen wurden gefunden: eine metallische Phase, eine supraleitende Phase mit Spin-Lücke, eine supraleitende Phase ohne Spin-Lücke, und Phasentrennung. Die metallische Phase wird von einer gleichmäßigen Verteilung der elektronischen Dichte und von einem abstoßenden LL-Parameter charakterisiert. Die supraleitenden Phasen werden von der Ausbildung von Elektronen-Paaren im Singulett-Zustand und von einem anziehenden LL-Parameter gekennzeichnet. Phasentrennung kann wegen der Entstehung von zwei Arten von Domains charakterisiert werden, leere Domains mit keinem Teilchen und Domains mit vielen Teilchen. Die Domains mit vielen Teilchen können von dem Heisenberg-Modell beschrieben werden. Bei sehr starker Wechselwirkung  $J$  gibt es eine zusätzliche Phase, Elektronensolide [34] genannt, wobei alle Elektronen in eine einzige Heisenberg-Insel zusammenfallen mit genau einem Teilchen pro Gitterplatz. Wie bereits erwähnt, sind die relevantesten Ergebnisse dieses Kapitels der engültige Beweis für eine endliche Spin-Lücke  $\Delta E_S$ , sowie die akkurate Bestimmung des Grundzustandsphasendiagramms. Im Unterschied zu anderen Studien, wurden unsere Ergebnisse mit einer Extrapolation zum thermodynamischen Limes bekommen und unsere Werte von der Spin-Lücke entsprechen zu unmittelbaren Messungen. Die Spin-Lücke hat einen maximalen Wert von  $\approx J/20$  bei niedrigen elektronischen Dichten und bei zunehmenden Werten von  $J$  (before die Phasentrennung erreicht wird). Da in einer Dimension Supraleitung nicht stattfinden kann, weil das Mermin-Wagner Theorem die spontane Symmetriebrechung von der  $U(1)$  Symmetrie verbietet, entspricht dieser endliche Wert von  $\Delta E_S$  der Energieskala für die Entstehung von Elektronen-Paaren im Singulett-Zustand. Diese Tatsache ist ein Zeichen für die Existenz von Preformed-Pairs in dem  $t$ - $J$  Modell.

Zum Abschluss wird in Kapitel 5 der t-DMRG Algorithmus angewendet, um die Zeitentwicklung von einem Elektron mit Spin up, das in das System addiert wurde, zu studieren. Als wichtige Observable betrachten wir die Ladungs- und Spindichte bezüglich des Grundzustandes. Das addierte Elektron hat die Form eines Gaußschen Wellenpakets mit einer angegebenen mittlere Position und einem angegebenen mittlere Impuls. Die Nutzung des t-DMRG Algorithmus hat den Vorteil, dass der Impuls nicht auf niedrige Werte beschränkt ist. Deshalb kann man das Problem sowohl bei niedrigen als auch bei hohen Energien untersuchen. Das Hauptergebnis dieses Kapitels (und auch dieser Arbeit) ist die Beobachtung von neuen Arten von Ladungs- und Spinfractionalisierung, die von der LL Theorie nicht erklärt werden können. Wenn  $k$  annähernd gleich dem Fermi Impuls

$k_F$  ist, erhalten wir die schon bekannten LL-Resultate, wie z.B Spin-Ladungsentkopplung [3] und die Fraktionalisierung der Ladung in zwei gegenpropagierende Wellenpakete [2]. Bei zunehmenden Werten von  $k$ , erscheinen zusätzliche Fraktionalisierung der Ladung und des Spins. Um die verschiedenen Bruchteile verstehen zu können, betrachten wir die Ladungsanregungen (Holons) und die Spinanregungen (Spinons) am supersymmetrischen Punkt (SUSY)  $J = 2t$ , wobei das Modell mittels Bethe-Ansatz exakt gelöst werden kann [8, 35, 36]. Wir haben innerhalb der metallischen Phase zwei verschiedene Regime festgelegt: Ein Regime mit  $v_\sigma > v_\rho$  und das andere mit  $v_\sigma < v_\rho$ , wo  $v_{\rho(\sigma)}$  die Ladungs- (Spin-)geschwindigkeit ist. Bei  $v_\sigma > v_\rho$  und  $k > k_F$  fängt das Spinon an, einen Bruchteil der Ladung zu tragen, der mit  $k$  zunimmt, während das Holon nur Ladung trägt. Bei  $v_\sigma < v_\rho$  und  $k > k_F$  tauschen die Ladung und der Spin die Rolle und nun fängt das Holon an, einen Bruchteil des Spins zu tragen, während das Spinon fast nur Spin trägt. Wenn man alle diese Tatsachen berücksichtigt, kann man argumentieren, dass bei hohen Energien eine komplette Spin-Ladungsentkopplung nicht mehr stattfinden kann und eine neue Art Anregung entsteht, das eine Mischung von beiden Freiheitsgraden trägt. Diese Beobachtung kann eine Tendenz zu Elektron-Rekombination bei hohen Energien vorschlagen. Dennoch ist diese Rekombination nicht total, weil es noch einen Teil der Ladung ohne Spin und mit umgekehrter Geschwindigkeit beobachtet wird.

# Chapter 1

## Introduction

The discreteness or continuity of the basic constituents or properties of our physical world has been always a fascinating issue among philosophers and scientists. One famous example is the electric charge. Michael Faraday (1791-1867) was the first to realize the discrete nature of the electric charge by means of his electrolysis experiments. Afterwards, Robert Millikan (1868-1953), with his well known experiment of the oil drop, could corroborate this discreteness and could even measure the fundamental unit of the electric charge, i.e. the charge of the electron. Therefore any direct measurement of the electric charge has to be an integer multiple of the electronic charge (excepting the quarks which have a fractional charge of either  $1/3$  or  $2/3$  and have not been observed isolated due to the color confinement). However there are some cases in condensed matter physics where we can speak of entities carrying fractional charge. These entities are excitations that are only possible inside the many body system. One of the most famous example is the fractional quantum hall effect at filling  $1/3$  [1], where the so called Laughlin quasiparticles, carrying one-third of the fundamental charge, are the elementary excitations of the system. Another example is the case of interacting one-dimensional systems where not only charge fractionalization [2] takes place but a complete decoupling of the spin and charge degrees of freedom is also possible at low energies [3]. On the other side, the important role of correlations in many physical phenomena has been more than well established. The most cited example in the literature is the phenomenon of high- $T_c$  superconductivity [4]. It can be said that its discovery has been the main motivation for the study of strongly correlated many-body quantum systems. A common feature of the high- $T_c$  superconducting materials is the presence of copper-oxide planes where superconductivity takes place making this a two-dimensional problem. One of the effective models used to describe this phenomenon is the so called  $t$ - $J$  model which is the strong-coupling version of the Hubbard model [5,6]. The  $t$ - $J$  model was also derived by Zhang and Rice starting from a two-band Hubbard Hamiltonian [7]. The  $t$ - $J$  model has been a real theoretical challenge and its solution is still unknown. In order to get some insights, one can start studying the one-dimensional (1D) case described by the following Hamiltonian

$$H = -t \sum_{i,\sigma}^{L-1} \left( \tilde{c}_{i,\sigma}^\dagger \tilde{c}_{i+1,\sigma} + \text{h.c.} \right) + J \sum_i^{L-1} \left( \vec{S}_i \cdot \vec{S}_{i+1} - \frac{1}{4} n_i n_{i+1} \right), \quad (1.1)$$

where the operator  $\tilde{c}_{i,\sigma}^\dagger$  ( $\tilde{c}_{i,\sigma}$ ) creates (destroys) a fermion with spin  $\sigma = \uparrow, \downarrow$  on the site  $i$ . They are not canonical fermionic operators since they act on a restricted Hilbert space without double occupancy.  $\vec{S}_i = (S_i^x, S_i^y, S_i^z) = \tilde{c}_{i,\alpha}^\dagger \vec{\sigma}_{\alpha\beta} \tilde{c}_{i,\beta}$  is the spin operator, where  $\vec{\sigma} = (\sigma_x, \sigma_y, \sigma_z)$  are the Pauli matrices.  $n_i = \tilde{c}_{i,\sigma}^\dagger \tilde{c}_{i,\sigma}$  is the density operator and  $L$  is the number of lattice sites. The first term represents the kinetic energy of electrons hopping between nearest-neighbor sites which is controlled by the constant  $t$ . The second term corresponds to exchange processes favoring the formation of

singlet-electron pairs in nearest-neighbor sites and it is controlled by the constant  $J$  (see Fig. 1.1). In spite of the simplicity of this Hamiltonian, it presents already in one dimension exotic ground-state phases like superconductivity, phase separation and spin gap, which are also phases found in high- $T_c$  cuprates. For this reason the one dimensional  $t$ - $J$  model is also an interesting problem to be considered as we will do throughout this work.

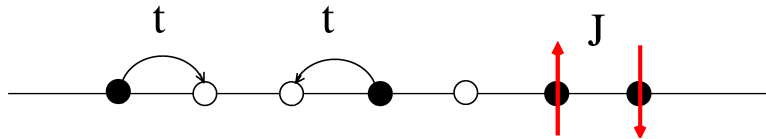


Figure 1.1: Graphical picture of the kinetic and interacting term of the Hamiltonian 1.1.  $t$  represents the tunneling probability for an electron (filled circle) to hop from one site to its nearest neighbor one.  $J$  controls exchange processes responsible for the formation of singlet-electron pairs in nearest neighbor sites.

Apart from the one-dimensional  $t$ - $J$  model, there are other motivations that have awakened the interest on 1D quantum systems. On the analytical side, the low-energy physics of any 1D quantum system can be well described by an effective quantum field theory namely the Luttinger liquid theory (LL) [3]. There are also cases of 1D models that can be solved exactly using Bethe-Ansatz [8–11]. On the numerical side, there are very efficient and precise techniques to study 1D systems like, for example, the DMRG algorithm (Density Matrix Renormalization Group) [12, 13]. And from the experimental point of view, there are several examples where indications of 1D quantum phenomena have been observed, like spin-charge separation [14–16] and charge fractionalization [17, 18]. Moreover the experimental realization of 1D systems is becoming more accessible, for example, in the case of quantum nanowires [19] and cold atoms in optical lattices [20, 21]. Along the experimental advances also theoretical progress was recently achieved pertaining extensions beyond the LL limit by incorporating nonlinearity of the dispersion, leading to qualitative changes in the spectral function [22–25] and relaxation processes of 1D electronic systems [18].

The main goal of our work is to investigate the phenomenon of spin and charge fractionalization of an electron injected into a strongly correlated chain, namely the 1D  $t$ - $J$  model, by means of the time-dependent DMRG method [26]. In order to compare and interpret our results we use the LL theory and the exact solution of the model at the supersymmetric point [8] as analytical framework. We show that fractionalization of charge and spin beyond the forms described by LL theory takes place at high energies, when a spin-1/2 fermion is injected into the  $t$ - $J$  model.

Before going into the real time dynamic, first, we study the ground-state properties by means of the static DMRG algorithm measuring energies and correlations. The most relevant results of this part are the demonstration of a finite spin gap, which was a source of controversy in previous works [27–29], and the precise determination of the ground-state phase diagram after extrapolating to the thermodynamic limit. One benefit of studying the zero temperature phase diagram is that the Luttinger parameter obtained during its determination is going to be useful when comparing with the low energy results of the real time dynamics, where the fractions of charge are given in terms of this parameter as we will see in Ch. 5.

The content of this work is organized as follows: In Ch. 2 we give a brief introduction to the Luttinger Liquid theory which is used to describe the low energy physics of one-dimensional systems and will be useful for our study of the 1D  $t$ - $J$  model. We start discussing some special features of 1D systems. Then motivated by the fact that particle-hole excitations for non-interacting 1D fermions have a well defined dispersion relation at low energies and in the limit of zero momentum, we introduce

the Tomonaga-Luttinger (TL) model. Taking this last fact as starting point, a low energy bosonic theory is derived. By means of renormalization group analysis, two asymptotic theories are found: a spin-gapless  $\Delta_\sigma = 0$  theory called Luttinger liquid (LL) and a spin-gapped theory called Luther-Emery (LE) theory. Using the correlation functions derived from these two theories we present a general phase diagram of the 1D systems with spin-rotational invariance at low energies. Finally we discuss the one-particle spectral function and spin and charge fractionalization in LL's

Chapter 3 is dedicated to the numerical method that we use for our simulations, namely, the Density Matrix Renormalization Group (DMRG) algorithm [12, 13, 26, 30]. This method is a very powerful tool to study the physics of one-dimensional problems allowing larger system sizes than other conventional methods like exact diagonalization (ED) or Lanczos [31]. First, we introduce the basic concept on which the DMRG is based on and then we proceed to explain the method in more detail. In few words, the success of the DMRG algorithm is due to a highly efficient reduction of the Hilbert space which converts this exponential problem into a polynomial one, such that it is now possible to deal with large systems (one or two order of magnitude larger in comparison to ED) using much less computational resources. The DMRG is mainly divided into a static and time-dependent DMRG. The static algorithm is actually the main core of the DMRG while the time-dependent method is an extension of it. We also discuss an important issue of the DMRG concerning the implementation of symmetries like the conservation of the total number of particles and the total magnetization. This last point is crucial for introducing an additional reduction of the Hilbert space and thus allowing to reach even larger systems. We explain how to measure one and two-points correlation functions, an issue that is going to be relevant for the determination of the phase diagram of the 1D  $t$ - $J$  model (Ch. 4). Finally we close the chapter by developing the time-dependent DMRG (t-DMRG) that can be seen as a particular case of a measurement, namely, that of the evolution operator. We use the adaptive t-DMRG [26] which is adaptive in the sense that the best representation of the Hilbert space is dynamically adapted to the current state of the system.

In Ch. 4 we apply the static DMRG method to measure energies and correlation functions in order to investigate the different phases of the one-dimensional  $t$ - $J$  model (1.1) [32, 33]. Four different phases are found: a metallic phase, a superconducting phase with spin gap, a gapless superconducting phase and phase separation. The metallic phase is characterized by a uniform distribution of the electronic density and by a repulsive Luttinger parameter; the superconducting phases by the formation of singlet-electron pairs and by an attractive Luttinger Liquid parameter; and phase separation by the formation of hole-rich and particle-rich domains with the latter being well described by the antiferromagnetic Heisenberg model. For very strong interactions there is also an additional phase called electron solid [34] where all electrons collapse into a single antiferromagnetic island with exactly one particle per lattice site. As we had mentioned before, the main results of this chapter are the precise determination of the ground-state phase diagram in the thermodynamic limit and the demonstration of a phase with a finite spin gap  $\Delta E_S$ . In contrast to previous studies [27–29], the measurement of our spin gap is a direct measurement.  $\Delta E_S$  reaches its largest value,  $\Delta E_S \approx J/20$ , as  $J$  increases for the limit of vanishing densities and before entering into phase separation. Since in a one-dimensional quantum system superconductivity cannot set in due to the Mermin-Wagner theorem<sup>1</sup>, such a finite value of the gap gives the energy scale at which pairs form, signaling the

---

<sup>1</sup>Any  $d$ -dimensional quantum system can be mapped to a  $d+1$ -dimensional classical system using the path integral representation. In this mapping the quantum fluctuations in the quantum system play the role of temperature in the classical system, therefore the latter is always at finite temperature. Then the Mermin-Wagner theorem (which states that continuous symmetries cannot be spontaneously broken at finite temperature in dimensions  $d \leq 2$ ) prevents any 1D quantum system to break spontaneously any continuous symmetry even at zero temperature (in the case of superconductivity the  $U(1)$  symmetry).

existence of preformed pairs in this regime. This very important result can be considered for future experimental realizations of the  $t$ - $J$  model.

Finally in Ch. 5 we apply the t-DMRG algorithm to study the real time evolution of the problem of one electron with spin up injected to the  $t$ - $J$  chain. The observables of interest are the charge and spin densities relative to the ground state of the system. The electron is injected in the form of a gaussian wavepacket with a certain average position and momentum. Using the t-DMRG has the advantage that we are not restricted to small momenta of the injected electron, i.e. to low energies. The main result of this chapter and also of our work is the observation of a novel kind of fractionalization of charge and spin which goes beyond the LL paradigm. When  $k$  is close to the Fermi wavevector  $k_F$ , the known features from LL theory, like spin-charge separation [3] and fractionalization of charge into two chiral modes (left- and right-going) [2], result. On increasing  $k$ , a further fractionalization of charge and spin appears, in forms that depend on the strength of the exchange interaction  $J$  or the density  $n$ . Their dynamics can be understood at the supersymmetric (SUSY) point  $J = 2t$  in terms of charge excitations (holons) and spin excitations (spinons) of the Bethe-Ansatz solution [8, 35, 36]. For the region of the phase diagram, where the ground state corresponds to a repulsive LL, two main regimes are identified: one regime where  $v_\sigma > v_\rho$  and another where  $v_\sigma < v_\rho$ , where  $v_{\rho(\sigma)}$  is the charge (spin) velocity. For  $v_\sigma > v_\rho$  and  $k > k_F$  the spinon starts to carry a fraction of charge that increases with  $k$  while the holon still carries only charge. For  $v_\sigma < v_\rho$  and  $k > k_F$  the situation is reversed and the holon carries a fraction of spin that increases with  $k$  while the spinon carries almost no charge. From these facts we can argue that at high energies complete spin-charge separation is no more possible and that a new kind of excitation, different from the holon or spinon and with mixed degrees of freedom of charge and spin, arises. This phenomenon may suggest a tendency of the system to recombine the electron at high energy. However this recombination is not total because we still observe a portion of charge without accompanying spin and moving with opposite velocity.

## Chapter 2

# Luttinger Liquids

In this chapter we introduce the theoretical framework used to describe the low energy physics of one-dimensional systems which will be useful for our study of the 1D  $t$ - $J$  model. First we discuss the special features of 1D systems that make them different from high dimensional ones. Then taking into account that particle-holes excitations for non-interacting 1D fermions have a well defined dispersion relation in the limit of zero energies and momenta, we introduce the Tomonaga-Luttinger (TL) model. Taking this latter as starting point, a low energy bosonic quantum field theory can be derived. By means of renormalization group analysis, two asymptotic theories are found: a spin-gapless theory  $\Delta_\sigma = 0$  called Luttinger liquid (LL) and a spin-gapped theory called Luther-Emery (LE) theory. Using the correlation functions derived from these two theories we present a general phase diagram of 1D systems with spin-rotational invariance at low energies. Finally we discuss the one-particle spectral function and spin and charge fractionalization in LL's. This chapter is focused mainly on the physical results. For more detailed calculations we refer the reader to Giamarchi's book [3].

### 2.1 Special features of 1D fermionic systems

Let us consider the Fermi gas as a starting reference model. In this model free electrons are the exact eigenstates of the Hamiltonian, i.e. excitations with infinite lifetime and well-defined energy and momentum.

After switching on the interactions, the electron are no longer exact eigenstates and in the case of systems with more than one dimension the physics is explained in terms of the so called quasiparticles. These quasiparticles are objects with the same charge and spin of the electron and they behave like free particles but with a renormalized mass. They are not exact eigenstates and this gives them a finite lifetime which goes to infinite at the Fermi surface. Therefore the name of quasiparticles. In contrast to the free gas, now the amplitude of the discontinuity in the momentum distribution is less than one (this quantity is also called quasiparticle weight) and there is a broadening of the delta peak in the one-particle spectral function. This physical description in terms of quasiparticles is well known as Landau's Fermi Liquid theory [37] and it relies mainly on the Pauli principle which is responsible for the presence of a well defined Fermi surface and for the above-mentioned physical properties. This theory has been successful in describing the properties of metallic materials in more than one dimension and it is not restricted to weak interaction, i.e. the quasiparticles are robust in most of the cases.

As for higher dimensions, we could also apply perturbation theory to the 1D Fermi gas. However, since the Fermi surface now consists only of two points, the nesting condition is always fulfilled.

This leads to singularities in the susceptibility which measures the response of the density to an applied external potential. A divergent perturbation theory is an indication that we are using the wrong reference state and this means that the perturbed system is entirely different from the initial reference state, in this case, the Fermi gas. One of the most popular ways to overcome this problem is the so called bosonization method [3]. However, this method is only valid in the low energy limit. In few words, bosonization consists in finding a transformation that allows to write the Hamiltonian of the interacting fermions in terms of some new bosonic operators representing density fluctuations. In this new basis the Hamiltonian can be easily diagonalized and all correlation functions and other physical properties can be computed. In the next sections we will develop more precisely the basic concepts of bosonization.

## 2.2 The Tomonaga-Luttinger model

Let us start considering the particle-hole excitation spectrum of non-interacting fermions in a lattice shown in Fig. 2.1. In 1D and at zero energy there are excitations only for momenta  $q = 0$  and  $\pm 2k_F$  while in 2D excitations with momenta in the whole range  $q = 0, \dots, \pm 2k_F$  are possible. This is due to the fact that in 1D the Fermi surface consists only of two points. Another particular characteristic

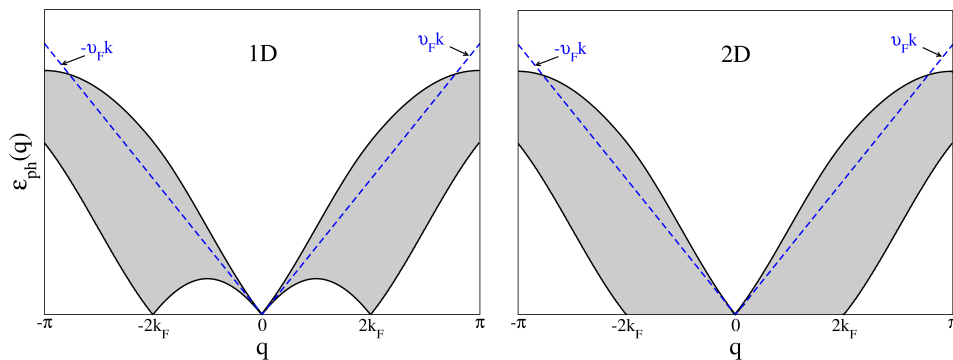


Figure 2.1: Particle-hole excitation spectrum  $\epsilon_{ph}(q)$  for the case of non-interacting fermions in a 1D and 2D lattice. At zero energy and in 1D there are excitations only for momenta  $q = 0, \pm 2k_F$ . This is one the characteristic difference between 1D and higher dimensional systems. Another special feature in 1D is that in the low energy limit the spectrum  $\epsilon_{ph}(q)$  corresponds to a well defined linear-dispersion relation.

in 1D, that we can observe in Fig. 2.1, is that the particle-holes excitation spectrum has a well defined linear dispersion relation in the limit of zero momentum and zero energy, i.e. they are well defined excitations. Note that we can make this condition perfect by assuming a linear dispersion relation  $\epsilon(k)$  because the particle-hole excitation spectrum,  $\epsilon_{ph}(q) = \epsilon(k + q) - \epsilon(k)$ , becomes  $k$ -independent. Since particle-holes are composed of two fermionic operators, they can be used in order to define some new operators obeying bosonic statistic [3]. Inspired by these facts, one can propose a model where the kinetic term contains a perfect linear dispersion (Tomonaga-Luttinger (TL) model)(see Eq. (2.1) and Fig. 2.2) and one can investigate whether this model would be able to describe the low-energy physics of any gapless 1D system. This linearization forces the extension of the dispersion to infinity with all negative-energy states filled. Therefore two different branches, R and L, have to be introduced: one for electrons created at  $+k_F$  (right movers) and another for those created at  $-k_F$  (left movers). The Hamiltonian of this model is given by the following kinetic

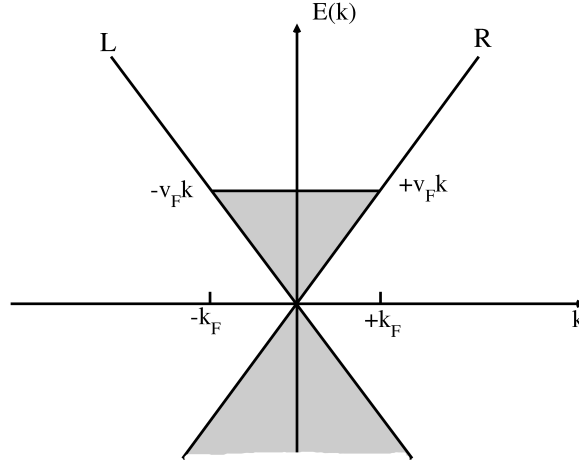


Figure 2.2: Linearized dispersion of the Tomonaga-Luttinger (TL) model. There are two different branches L and R for left and right propagating electrons, respectively. Similarly to the case of Dirac equation, all negative-energy states are filled (Dirac sea).

and interacting terms,  $H_0$  and  $H_{int}$ ,

$$H_0 = \sum_{k;r=\pm;\sigma=\uparrow,\downarrow} v_F(rk - k_F)c_{r,k,\sigma}^\dagger c_{r,k,\sigma}, \quad (2.1)$$

$$H_{int} = \frac{1}{2L} \sum_{\substack{q,k',k,r''', \\ r'',r',r,\sigma',\sigma}} V(q)c_{r''',k+q,\sigma}^\dagger c_{r'',k'-q,\sigma'}^\dagger c_{r',k',\sigma'} c_{r,k,\sigma}, \quad (2.2)$$

where  $c_{r,k,\sigma}^\dagger$  and  $c_{r,k,\sigma}$  are the canonical fermionic operators with chirality  $r = \pm$  (where  $+(-)$  stands for right(left) movers), momentum  $k$  and spin  $\sigma$ .  $L$  is the length of the system and  $V(q)$  is the Fourier transform of some kind of interaction that depends only on the distance between particles. At low energies the interaction part can be approximated to few processes with coupling constants  $g_{1||}$ ,  $g_{1\perp}$ ,  $g_{2||}$ ,  $g_{2\perp}$ ,  $g_{4||}$  and  $g_{4\perp}$ . The subindex  $||$  ( $\perp$ ) stands for the case where the two particles have the same (opposite) spin. In Fig. 2.3 we illustrate the physical meaning of these processes. In the  $g_2$  processes the two particles have initially different chirality and each of them conserves its chirality after the interaction. The  $g_4$  interaction corresponds to processes with two particles in the same branch and staying there after the interaction. In the  $g_1$  processes the two particles are initially in different branches and after the interaction each of them changes its chirality. Note that since  $g_2$  and  $g_4$  do not change their chirality (forward scattering), they have momentum  $q \sim 0$ , while for  $g_1$ , where the particles do change their branch (backward scattering), we have that  $q \sim 2k_F$ . Since for 1D spinless fermions one particle in the chain cannot move without pushing the others, only collective excitations are possible and therefore density fluctuations are a good candidate for the excitations of the TL model. In fact, density fluctuations can be written as a linear combination of particle-holes as follows [3, 38]

$$\nu_r(q) = \frac{1}{\sqrt{2}} \sum_k (c_{r,k+q,\uparrow}^\dagger c_{r,k,\uparrow} \pm c_{r,k+q,\downarrow}^\dagger c_{r,k,\downarrow}) \quad (2.3)$$

where  $\nu = \rho$  ( $\sigma$ ) denotes charge (spin) density fluctuations. The sign  $+$  ( $-$ ) corresponds to  $\rho$  ( $\sigma$ ). Since these density fluctuations are composed of the product of two fermionic operators, they have bosonic nature.

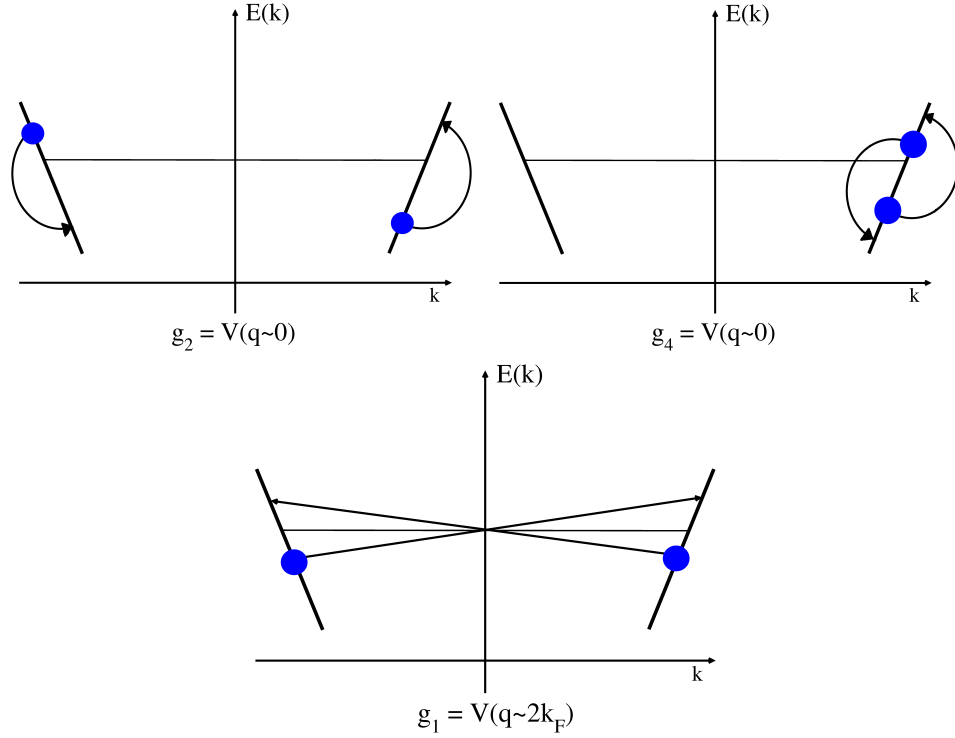


Figure 2.3: Important low-energy interacting processes of any gapless fermionic system. For simplicity we have not considered the spins variables  $\sigma'$  and  $\sigma$  and therefore each coupling constant  $g_i$  represents actually two more quantities:  $g_{i\parallel}$  for processes with the same spin ( $\sigma' = \sigma$ ) and  $g_{i\perp}$  for processes with opposite spin ( $\sigma' = -\sigma$ ).

Let us consider the situation with no backward scattering ( $g_1 = 0$ ). The kinetic term  $H_0$  and the interacting terms corresponding to the processes  $g_2$  and  $g_4$  can be rewritten in terms of these density fluctuations as [3, 38]

$$H_0 = \frac{\pi v_F}{L} \sum_{\nu=\rho,\sigma} \sum_q [\nu_+(q)\nu_+(-q) + \nu_-(q)\nu_-(-q)], \quad (2.4)$$

$$H_2 = \frac{2}{L} \sum_{\nu=\rho,\sigma} \sum_q g_{2\nu} \nu_+(q)\nu_-(-q), \quad (2.5)$$

$$H_4 = \frac{1}{L} \sum_{\nu=\rho,\sigma} \sum_q g_{4\nu} [\nu_+(q)\nu_+(-q) + \nu_-(-q)\nu_-(q)], \quad (2.6)$$

where the effective couplings  $g_{i\nu}$  are defined as

$$g_{i\nu} = \frac{1}{2}(g_{i\parallel} \pm g_{i\perp}). \quad (2.7)$$

In the absence of interactions ( $H_2 = H_4 = 0$ )  $H_0$  describes bosonic modes of charge and spin both propagating with the same velocity  $v_F$ . Note that  $H_0$  and  $H_4$  correspond to interaction of density fluctuations with the same chirality and therefore the effect of  $H_4$  is just to renormalize the Fermi velocity to  $v_\nu = v_F + g_{4\nu}/\pi$ . Hence it is interesting to remark that a system described only by  $H = H_0 + H_4$  can already contain charge and spin modes propagating with different velocities  $v_\rho$  and

$v_\sigma$ , respectively, as long as  $g_{4\rho} \neq g_{4\sigma}$ . For this reason,  $H = H_0 + H_4$  is called the minimal model for spin-charge separation. Therefore, we conclude that the  $g_4$  processes alone contribute to the effect of spin-charge separation. Let us now also include the term  $H_2$ , which represents interactions of density fluctuations with different chirality. Note that  $H = H_0 + H_2 + H_4$  is quadratic in the bosonic operators  $\nu_r(q)$  and therefore it can be diagonalized via a Bogoliubov transformation resulting in a free-bosonic Hamiltonian with renormalized velocities

$$v_\nu = \sqrt{(v_F + g_{4\nu}/\pi)^2 - (g_{2\nu}/\pi)^2}. \quad (2.8)$$

From this last expression we realize that the  $g_2$  processes are also responsible for spin-charge separation because they also contribute to make the spin and charge velocities different from each other. Note also that  $H = H_0 + H_2 + H_4$  can be rewritten as  $H = H_\rho + H_\sigma$  where  $H_\rho$  ( $H_\sigma$ ) involves only charge (spin) degrees of freedom. Since these two terms commute, they can be separately solved and therefore all the eigenstates can be expressed as a tensor product of a pure charge state and a pure spin state. This is in fact the explanation for having the above-mentioned spin-charge separation. Experimental evidences of its existence have been observed in quasi-1D organic conductors [16], semiconductor quantum wires [39], and quantum chains on semiconductor surfaces [19].

## 2.3 Effective quantum field theory

Starting from the TL model (2.1), (2.2), a low energy quantum field theory can be derived given by the following Hamiltonian [3]

$$\begin{aligned} H &= \frac{1}{2\pi} \int dx v_\rho [K_\rho (\pi \Pi_\rho(x))^2 + \frac{1}{K_\rho} (\nabla \phi_\rho(x))^2] \\ &+ \frac{1}{2\pi} \int dx v_\sigma [K_\sigma (\pi \Pi_\sigma(x))^2 + \frac{1}{K_\sigma} (\nabla \phi_\sigma(x))^2] \\ &+ \frac{2g_{1\perp}}{(2\pi\alpha)^2} \int dx \cos(2\sqrt{2}\phi_\sigma), \end{aligned} \quad (2.9)$$

where the bosonic fields  $\Pi_\nu$  and  $\phi_\nu$  satisfy canonical commutation relations

$$[\Pi_\nu(x_1), \phi_{\nu'}(x_2)] = i\delta_{\nu,\nu'}\delta(x_1 - x_2)$$

and  $v_\nu$  and  $K_\nu$  are parameter of the model.  $v_\nu$  has dimension of velocity and  $K_\nu$  is a dimensionless parameter that controls the long-distance power law decay of all correlation functions (2.18-2.29). As we explained before for the TL model,  $g_{1\perp}$  is the coupling constant associated with interacting processes involving backward scattering of two particles with opposite spin. The constant  $\alpha$  is an arbitrary short distance cutoff that regularizes the largest momentum. Strictly speaking one should take the limit  $\alpha \rightarrow 0$  in order to obtain physical properties that are independent of  $\alpha$ , however, keeping  $\alpha$  finite is a good way to introduce an artificial finite bandwidth [3]. The Luttinger parameters  $v_\nu$  and  $K_\nu$  can be written as a function of the interaction constants of TL model (see Fig. 2.3) as follows:

$$v_\nu = \sqrt{(v_F + g_{4\nu}/\pi)^2 - (g_\nu/\pi)^2}, \quad (2.10)$$

$$K_\nu = \sqrt{\frac{\pi v_F + g_{4\nu} - g_\nu}{\pi v_F + g_{4\nu} + g_\nu}}, \quad (2.11)$$

with  $g_{i\nu}$  given by Eq. (2.7) and  $g_\nu = g_{2\nu} - \frac{1}{2}g_{1\parallel}$ . Note very generally from Eq. (2.11) that for  $g_\nu > 0$  ( $g_\nu < 0$ ), that is, repulsive (attractive) interactions in the coupling  $g_\nu$ , we have that  $K_\nu < 1$  ( $K_\nu > 1$ ); and for  $g_\nu = 0$  (no interactions in  $g_\nu$ ) then  $K_\nu = 1$ . At this point it is important to take the word “interaction” with special care and to remark that this latter does not necessarily correspond to the electron interactions. For example, although the case  $K_\nu = 1$  (i.e.  $g_\nu = 0$ ) would reproduce the correlations functions of the free-electron problem (see Eqs. (2.18)-(2.23) with  $K_\nu = 1$ ), as long as  $g_{4\nu} \neq 0$ , then the spin and charge velocities,  $v_\sigma$  and  $v_\rho$ , are different and this does not correspond to the case of non-interacting electrons. For this reason, this last situation with the particular values  $g_{2\nu} = g_{1\parallel} = g_{1\perp} = 0$  is called the minimal model for spin-charge separation, as we have mentioned before.

As in the TL model, the Hamiltonian (2.9) can be split into a pure charge and pure spin part (spin-charge separation). In the case when  $g_{1\perp} = 0$ , the Hamiltonian (2.9) just represents two free bosonic theories (one for the charge and one for the spin degree of freedom) with modes propagating with velocities  $v_\rho$  and  $v_\sigma$ , respectively.

The fields  $\Pi_\nu$  and  $\phi_\nu$  can be written in terms of the density fluctuation of the TL model as

$$\Pi_\nu(x) = \frac{1}{L} \sum_{q \neq 0} e^{-\alpha|q|x/2 - iqx} [\nu_+(q) - \nu_-(q)] + \frac{J_\nu}{\sqrt{2}L}, \quad (2.12)$$

$$\phi_\nu(x) = -\frac{i\pi}{L} \sum_{q \neq 0} \frac{1}{q} e^{-\alpha|q|x/2 - iqx} [\nu_+(q) + \nu_-(q)] - N_\nu \frac{\pi x}{\sqrt{2}L}, \quad (2.13)$$

where the total charge  $N_\rho$ , the total spin  $N_\sigma$ , the charge current  $J_\rho$  and the spin current  $J_\sigma$  are given by

$$N_\nu = Q_\uparrow \pm Q_\downarrow, \quad (2.14)$$

$$J_\nu = J_\uparrow \pm J_\downarrow, \quad (2.15)$$

with

$$Q_\uparrow = N_{+\uparrow} + N_{-\uparrow}, \quad Q_\downarrow = N_{+\downarrow} + N_{-\downarrow}, \quad (2.16)$$

$$J_\uparrow = N_{+\uparrow} - N_{-\uparrow}, \quad J_\downarrow = N_{+\downarrow} - N_{-\downarrow}, \quad (2.17)$$

and the operator  $N_{r\sigma}$  counts the total number of particles with chirality  $r$  and spin  $\sigma$  relative to the ground state.

Renormalization group theory can be used in order to deal with the sine Gordon term (third integral of Eq. (2.9)) [3]. The renormalization flow presents two different situations: flow either to zero or to strong  $g_{1\perp}$  coupling. In the first case the renormalization flow tells us that the couplings  $g_{1\perp}$  and  $K_\sigma$  go to the fixed point  $g_{1\perp} = 0$  and  $K_\sigma = 1$  and then the sine-Gordon term is irrelevant. In this case we have a free-gapless-bosonic theory that is known as Luttinger Liquid (LL) theory. In the second case the renormalization flow goes to strong coupling and the sine-Gordon term gives rise to the opening of a spin gap (Note that if we exchange the spin and charge degrees of freedom, a model with charge gap results. This can be related to the Mott-insulator transition which is explained in detail in the reference [3]). This gap as a function of the coupling constant  $g_{1\perp}$  is exponentially small for system with spin rotational invariance and it is a power law for very strong coupling. This massive theory is separately known as a Luther-Emery liquid.

Haldane [40] has derived the same Hamiltonian (2.9) from phenomenological but more general considerations showing that all properties of the TL model are in fact also present in any one-dimensional system at low energy. The physical reason for this is that, similarly as in the Fermi liquid theory, the Luttinger liquid theory is an effective field theory that is the fixed point of all gapless one-dimensional theories.

## 2.4 Correlation functions and phase diagram

For any model described by the LL theory, the long distance behavior of the most significant correlations functions is given by [3]

$$\langle n(x)n(0) \rangle = K_\rho(\pi x)^{-2} + A_1 \cos(2k_F x) \ln^{-3/2}(x) x^{-(K_\sigma+K_\rho)} + A_2 \cos(4k_F x) x^{-4K_\rho} \quad (2.18)$$

$$\langle S^x(x)S^x(0) \rangle = K_\sigma(\pi x)^{-2} + B_1 \ln^{1/2}(x) \cos(2k_F x) x^{-(K_\rho+1/K_\sigma)}, \quad (2.19)$$

$$\langle S^y(x)S^y(0) \rangle = K_\sigma(\pi x)^{-2} + B_1 \ln^{1/2}(x) \cos(2k_F x) x^{-(K_\rho+1/K_\sigma)}, \quad (2.20)$$

$$\langle S^z(x)S^z(0) \rangle = K_\sigma(\pi x)^{-2} + B_1 \ln^{1/2}(x) \cos(2k_F x) x^{-(K_\rho+K_\sigma)}, \quad (2.21)$$

$$\langle \Delta_S^\dagger(x)\Delta_S(0) \rangle = C_0 x^{-(K_\sigma+1/K_\rho)} \ln^{-3/2}(x) + C_1 \cos(2k_F x) x^{-(K_\rho+1/K_\rho)}, \quad (2.22)$$

$$\langle \Delta_T^\dagger(x)\Delta_T(0) \rangle = D_0 x^{-(K_\sigma+1/K_\rho)} \ln^{1/2}(x) + D_1 \cos(2k_F x) x^{-(K_\rho+1/K_\rho+K_\sigma+1/K_\sigma)}, \quad (2.23)$$

where  $\langle n(x)n(0) \rangle$  is the density-density correlation function,  $\langle S^z(x)S^z(0) \rangle$  is the spin-spin correlation function in the z-direction,  $\langle \Delta_S^\dagger(x)\Delta_S(0) \rangle$  is the singlet-pair correlation function and  $\langle \Delta_T^\dagger(x)\Delta_T(0) \rangle$  is the triplet-pair correlation function.  $A_i, B_i, C_i$  and  $D_i$  are constants that depend on the particular model to be considered. Note that the first term (zero momentum term) of the density-density and spin-spin correlation functions has the same power-law behavior  $(1/x)^2$  as in the free-electron case and only the amplitude is renormalized by  $K_\nu$  as an effect of the interactions. Note also that, since for a system with spin-rotational invariance the spin correlation functions have to be the same in all space directions, then Eqs. (2.19)-(2.21) imply that  $K_\sigma = 1$  in this case. This can also be seen by setting  $g_{i\perp} = g_{i\parallel}$  (i.e. spin rotational invariance) and  $g_{1\perp} = g_{1\parallel} = 0$  (i.e. LL) in Eq. (2.11). The different operators are defined as a function of fermionic field operators  $\psi_\sigma(x) = (1/\sqrt{\Omega}) \sum e^{ikx} c_{k\sigma}$  as follows:

$$n(x) = \psi_\uparrow^\dagger(x)\psi_\uparrow(x) + \psi_\downarrow^\dagger(x)\psi_\downarrow(x), \quad (2.24)$$

$$\vec{S}(x) = \psi_{\sigma'}^\dagger(x)\vec{\sigma}_{\sigma'\sigma}\psi_\sigma(x), \quad (2.25)$$

$$\Delta_S^\dagger(x) = \frac{1}{\sqrt{2}}(\psi_\downarrow^\dagger(x)\psi_\uparrow^\dagger(x) - \psi_\uparrow^\dagger(x)\psi_\downarrow^\dagger(x)), \quad (2.26)$$

$$\Delta_T^\dagger(x) = \psi_\uparrow^\dagger(x)\psi_\uparrow^\dagger(x), \quad (2.27)$$

where  $\vec{\sigma} = (\sigma^x, \sigma^y, \sigma^z)$  are the Pauli matrices.

In the LE theory the spin-spin and triplet-pair correlations are exponentially suppressed due to the opening of the spin gap and the other two correlation functions are given by

$$\langle n(x)n(0) \rangle = A_0 x^{-2} + A_1 \cos(2k_F x) x^{-K_\rho}, \quad (2.28)$$

$$\langle \Delta_S^\dagger(x)\Delta_S(0) \rangle = C'_0 x^{-1/K_\rho} + C'_1 \cos(2k_F x) x^{-(K_\rho+1/K_\rho)}. \quad (2.29)$$

Note that in both theories (LL and LE) there is more than one correlation with power-law decay, i.e. there are competing orders. The exponents for this power-law decay are given in terms of the Luttinger parameters  $K_\rho$  and  $K_\sigma$  which depend on the interactions of the particular model. Therefore they are not universal exponents. However the LL theory (and also the LE theory) is universal in the sense that once we have found a way to compute the parameters  $K_\rho$  and  $K_\sigma$ , then we can know about all the low energy properties of the system. In a one-dimensional quantum system (i.e 1 + 1-dim classical system) the Mermin-Wagner theorem prevents any continuous symmetry to be spontaneously broken (an intuitive explanation for this is that in 1D the fluctuations are so strong that they do not allow the system to order). Therefore in 1D the closest situation to long-range order is a power-law decay (also called quasi-long-range order).

However, for a system with spin rotational invariance (i.e. isotropic couplings  $g_{i||} = g_{i\perp}$  and  $K_\sigma$  is renormalized to one in the massless phase) we can plot the phase diagram (Fig. 2.4) considering the most dominant order given by the correlation function with the slowest decay. In Fig. 2.4 the notation CDW stands for charge density wave, SDW for spin density wave, SS for singlet superconductivity and TS for triplet superconductivity. In this phase diagram the region denoted by CDW means that the density-density correlation is the dominant correlation, similarly, SDW for the spin-spin correlation, SS for the singlet-pair correlation, and TS for the triple-pair correlation function. The subdominant orders are denoted in parenthesis. In the case of CDW and SDW phases the density fluctuations have a wavelength of  $2k_F$  (i.e. the second term in Eqs. (2.18)-(2.21) is the strongest divergence) while the fluctuations in the superconducting phases SS and TS have wavelength equal to zero. Note from Eqs. (2.18)-(2.21) that for  $K_\sigma = 1$  the CDW and SDW orders have the same power law decay and it is only the logarithmic factor that makes the SDW order to be the dominant one. A similar situation occurs between the TS and SS orders. In Ch. 4 we are going to consider the behavior of all these correlations in order to identify the different phases of the  $t$ - $J$  model.

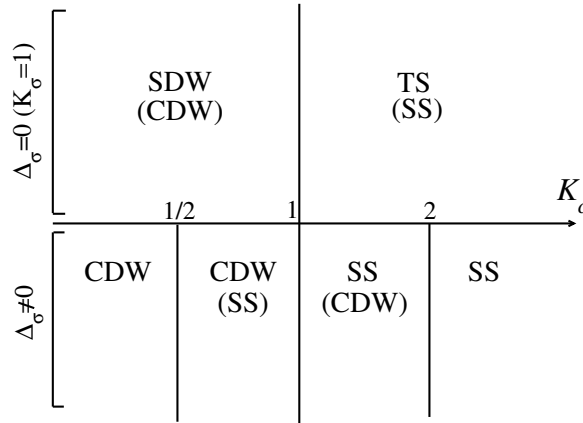


Figure 2.4: Phase diagram of the Hamiltonian (2.9) with isotropic couplings  $g_{i||} = g_{i\perp}$  (spin rotational invariance) [3]. The phases correspond to the most dominant order depending on the values of the parameter  $K_\rho$ . The subdominant kind of order for a given phase is indicated in parenthesis. In the upper part the spin degree of freedom is gapless ( $\Delta_\sigma = 0$ ) while in the lower part the spin excitations are gapped ( $\Delta_\sigma \neq 0$ ).

## 2.5 One-particle spectral function

Another important physical quantity to be considered is the one-particle spectral function  $A(k, \omega)$  which represents the probability for adding (removing) a particle with energy  $\omega > 0$  ( $\omega < 0$ ) and momentum  $k$  into the system. For a spin rotational invariant Luttinger liquid ( $g_1 = 0$  and  $g_{i||} = g_{i\perp}$ ) this quantity was analytically calculated in previous studies [38,41]. In Fig. 2.5  $A(k, \omega)$  is plotted for a fixed  $k$  such that  $(k - k_F) > 0$ . The different exponents are functions of  $K_\nu$  through the relation  $\gamma_\nu = (K_\nu + K_\nu^{-1} - 2)/8$ . For  $\omega > 0$ , in contrast to the Fermi liquid theory where  $A(k, \omega)$  consists of a single-Lorentzian quasiparticle peak, in the LL case there are two power-law singularities at energies  $v_\sigma(k - k_F)$  and  $v_\rho(k - k_F)$ , respectively. This is a signature of spin-charge separation and that single-particle excitations do not exist, that is, one electron injected to the LL chain will split into two different collective modes of spin and charge density fluctuations propagating with

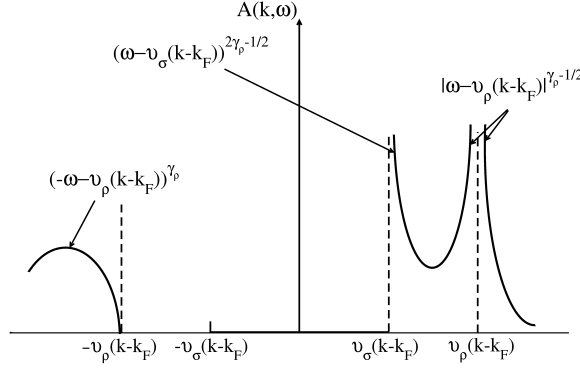


Figure 2.5: One-particle spectral function  $A(k, \omega)$  for a fixed  $k$  such that  $(k - k_F) > 0$  [38, 41]. The different exponents are functions of  $K_\nu$  through the relation  $\gamma_\nu = (K_\nu + K_\nu^{-1} - 2)/8$ . Note that for  $\omega > 0$  there are two power-law singularities at energies  $v_\sigma(k - k_F)$  and  $v_\rho(k - k_F)$ , respectively, in contrast to the Fermi liquid case.

different velocities. In Sec. 5.2.2 we will corroborate this fact by means of time-dependent numerical simulation. As is explained in reference [38], the finite spectral weight present at  $\omega < 0$  is due to interaction between density fluctuations on the two different branches (right and left movers), i. e., due to  $g_2$  processes. Note that in this case  $K_\rho \neq 1$  and therefore this finite weight at  $\omega < 0$  is an effect of the anomalous exponent  $K_\rho$ .

## 2.6 Charge and spin fractionalization

Additionally to spin-charge separation the LL Hamiltonian (Eq. (2.9) with  $g_{1\perp} = 0$ ) presents also chiral separation [2]. In order to explain this feature we introduce the following fields:

$$\Theta_\pm(x, t) = \phi(x, t) \mp \frac{\Phi(x, t)}{K}, \quad (2.30)$$

where  $\Phi(x, t)$  is defined through the relation  $\Pi(x, t) = \nabla\Phi(x, t)$ . We have omitted spin and charge indices for simplicity. Using these fields, each part (charge and spin parts) of the LL Hamiltonian can be split as follows:

$$H = H_+ + H_-, \quad (2.31)$$

with

$$H_\pm = \frac{vK}{4\pi} \int dx [\partial_x \Theta_\pm(x, t)]^2. \quad (2.32)$$

From the commutation relations of the fields  $\Pi$  and  $\phi$  and from the definition of  $\Theta$  it can be proven that  $[H_+, H_-] = 0$ . Moreover the equations of motion fulfilled by the fields  $\Theta_\pm(x, t)$  are

$$v\partial_x \Theta_\pm(x, t) = \mp \partial_t \Theta_\pm(x, t), \quad (2.33)$$

which implies that in fact  $\Theta_\pm(x, t) = \Theta_\pm(x \mp vt)$  are chiral fields, i.e. they represent two counter-propagating modes. As it is explained in more detail in Ref. [2] the chiral separation induces a

fractionalization of charge (and spin) into two fractions  $Q_{\rho,+}$  and  $Q_{\rho,-}$  ( $Q_{\sigma,+}$  and  $Q_{\sigma,-}$ ), which move with opposite velocities  $v_\rho$  and  $-v_\rho$  ( $v_\sigma$  and  $-v_\sigma$ ), given by

$$Q_{\rho,\pm} = \frac{Q_\uparrow + Q_\downarrow}{2} \pm K_\rho \frac{J_\uparrow + J_\downarrow}{2}, \quad Q_{\sigma,\pm} = \frac{Q_\uparrow - Q_\downarrow}{2} \pm K_\sigma \frac{J_\uparrow - J_\downarrow}{2}, \quad (2.34)$$

where the sign  $+$  ( $-$ ) stands for right (left) movers and  $Q_\uparrow$ ,  $Q_\downarrow$ ,  $J_\uparrow$ ,  $J_\downarrow$  are defined in Eqs. (2.16, 2.17) in terms of the number of particles injected into the system.

In particular, we are interested in the case of one right-propagating electron with spin up injected to a LL (Fig. 2.6), that is,  $N_{+\uparrow} = 1$  and  $N_{+\downarrow} = N_{-\uparrow} = N_{-\downarrow} = 0$ . Using Eqs. (2.16, 2.17) this

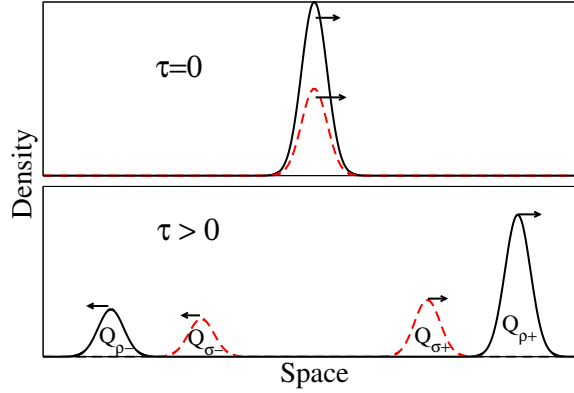


Figure 2.6: Schematic representation of charge (black line) and spin (red-dashed line) fractionalization of a single right-propagating electron with spin up injected at  $\tau = 0$  into a LL.  $Q_{\nu,\pm}$  stands for the different fractions of charge and spin.

translates into  $Q_\uparrow = J_\uparrow = 1$ ,  $Q_\downarrow = J_\downarrow = 0$  and if we assume spin rotational invariance (i.e.  $K_\sigma = 1$ ), then Eqs. (2.34) become

$$Q_{\rho,\pm} = \frac{1 \pm K_\rho}{2}, \quad Q_{\sigma,\pm} = \frac{1 \pm 1}{2}. \quad (2.35)$$

Note that  $Q_{\sigma,+} = 1$  and  $Q_{\sigma,-} = 0$ , i.e. for a LL with spin rotational invariance the initially injected right-propagating spin does not split into chiral fractions. On the other hand, the charge  $Q_{\rho,\pm}$  does fractionalize into two parts with opposite chirality and such fractionalization is mediated by the Luttinger parameter  $K_\rho$ , that is, the more different is  $K_\rho$  from one, the larger is the fractionalization. This fractionalization of charge has been recently experimentally confirmed in quantum nanowires [17].

Taking the low energy processes discussed for the TL model as a reference, note that for a LL with spin rotational invariance (i.e.  $g_{1\parallel} = g_{1\perp} = 0$ ) the Luttinger parameter  $K_\rho$  is different from one only when the interactions  $g_2$  are non-zero (see Eq. (2.11) and Fig. 2.3), in other words, only when the interaction between density fluctuations with different chirality are not negligible (see  $H_2$  in Eq. (2.5)). Hence, in a LL only  $g_2$  processes are responsible for spin and charge fractionalization whereas both  $g_2$  and  $g_4$  processes might be responsible for spin-charge separation. In Ch. 5 we will carry out this kind of theoretical experiment using the time-dependent DMRG numerical method in order to investigate spin and charge fractionalization as well as spin-charge separation at low and at high energies.

## Chapter 3

# The Density Matrix Renormalization Group Method

In general, the quantum problem consists mainly in finding the eigenvalues and eigenvectors of the Hamiltonian operator  $H$ . This is equivalent to diagonalize the matrix representation of  $H$ , which is written in a certain basis of the Hilbert space. In particular, we are interested in a one-dimensional quantum system composed of many identical particle. The Fock space basis of this problem is given by the set of vectors

$$\{|S_{i_1}\rangle|S_{i_2}\rangle\cdots|S_{i_L}\rangle\},$$

where  $i_j = 1, \dots, d$  and  $d$  is the number of states that can assume each vector  $|S_{i_j}\rangle$ . Since each basis vector is a tensor product of  $L$  vectors, then the dimension of space of states is  $d^L$ . With this notation we say that the system has  $L$  sites and that the site 1 is in the state  $|S_{i_1}\rangle$ , the site 2 is in the state  $|S_{i_2}\rangle$ , and so on (Fig. 3.1). For instance, in the case of spinless fermions each site can assume only two ( $d = 2$ ) different states:  $|0\rangle$  (no fermions or vacuum) or  $|1\rangle$  (one fermion in the site).

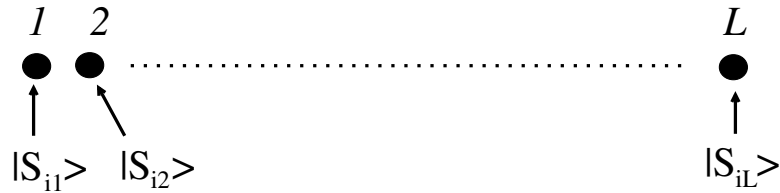


Figure 3.1: One dimensional chain.

Since the dimension of the Hilbert space grows exponentially with the size of the system, it is not possible to solve this problem exactly for a large number of particles due to the limited capacity of the computer. In order to overcome this problem, efficient numerical techniques have to be developed. One of these techniques is the so called Density Matrix Renormalization Group (DMRG) [12, 13, 30, 42]). The DMRG algorithm can be understood in terms of the Matrix Product State (MPS) [30] formalism, that is, each coefficient of any state can be written as product of a set of matrices. However in this work I will focus only on the conventional DMRG as it was initially presented by White [12] and which I have used to developed my computational code.

In general words the DMRG algorithm consists in reducing the Hilbert space as much as possible in such a way that important physical quantities can be still computed with very high precision for

system sizes larger than those solved with exact diagonalization. The criteria for the truncation of the Hilbert space is based on the eigenvectors and eigenvalues of the so called reduced density matrix. In the following we will develop in more detail this general idea.

Let us start dividing the system into two parts as is shown in Fig. 3.2. Let us assume that the set

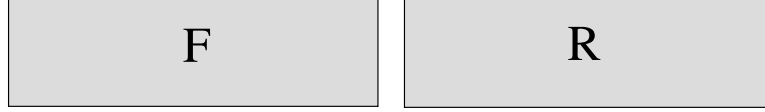


Figure 3.2: The one-dimensional chain of atoms is divided into two parts.

of vectors  $|i\rangle$  is a basis for the subspace  $F$  and the set  $|j\rangle$  for the subspace  $R$ . Then a basis of the entire system is just given by the set  $|i\rangle|j\rangle$  (tensor product). Therefore any state of the system can be expressed as

$$|\psi\rangle = \sum_i^{d_F} \sum_j^{d_R} \psi_{ij} |i\rangle|j\rangle, \quad (3.1)$$

where  $d_F$  ( $d_R$ ) is the dimension of the subspace  $F$  ( $R$ ) and  $\psi_{ij}$  are in general complex coefficients. In order to reduce the Hilbert space of the problem we can define a truncated state

$$|\tilde{\psi}\rangle = \sum_\alpha^m \sum_j^{d_R} a_{\alpha j} |\alpha\rangle|j\rangle, \quad (3.2)$$

with  $m < d_F$  and the vectors  $|\alpha\rangle$  come from a change of basis in the left part. Hence our purpose would be to find a new basis  $|\alpha\rangle$  that produces a truncated state (3.2) which is the best representation of the exact state  $|\psi\rangle$ . For this reason the state  $|\psi\rangle$  is denoted as the target state. In other words we have to find  $|\alpha\rangle$  such that the distance  $\| |\tilde{\psi}\rangle - |\psi\rangle \|$  is minimum. It can be proved (see appendix A.1) that the set of  $|\alpha\rangle$  fulfilling this condition are given by the eigenvectors with the highest eigenvalues of the reduced density matrix operator, which is defined by

$$\rho = Tr_R |\psi\rangle\langle\psi|, \quad (3.3)$$

where the matrix representation of the trace,  $Tr_R$ , of any operator  $O$  is given by

$$[Tr_R O]_{i',i} = \sum_j^{d_R} \langle i'| \langle j| O |i\rangle |j\rangle. \quad (3.4)$$

Note that Eqs. (3.4) and (3.3) correspond to operators acting only on the left part because we have traced out all the degrees of freedom of right part. In a similar way the truncation of the right part can be done by exchanging right for left and left for right. One important property of  $\rho$  is that the mean value of an operator  $A$  can be written as

$$\langle\psi|A|\psi\rangle = Tr_L(\rho A) = \sum_i^{d_F} \nu_i \langle\nu_i|A|\nu_i\rangle, \quad (3.5)$$

where  $\nu_i$  and  $|\nu_i\rangle$  are the eigenvalues and eigenvectors of  $\rho$ , respectively. The eigenvalues satisfy  $\nu_i > 0$  and  $\sum \nu_i = 1$ , that is,  $\nu_i$  represents the probability of measuring  $\langle\nu_i|A|\nu_i\rangle$ . If we assume

that  $\nu_i$  decays very fast, then we can compute the mean value (3.5) by taking only the  $m$  largest eigenvalues  $\nu_i$ ,

$$\langle \psi | A | \psi \rangle = \text{Tr}_L(\rho A) = \sum_{i=1}^m \nu_i \langle \nu_i | A | \nu_i \rangle. \quad (3.6)$$

This truncation generates an error that, using the property  $\sum \nu_i = 1$ , can be defined as

$$\epsilon \equiv \sum_{i=m+1}^{d_F} \nu_i = 1 - \sum_{i=1}^m \nu_i. \quad (3.7)$$

In order to understand the entanglement between the left and right part (Bipartite entanglement), Eq. (3.1) can be rewritten in terms of the eigenvectors of  $\rho$  using the singular value decomposition (SDV) (see appendix A.2) as follows,

$$|\psi\rangle = \sum_{\alpha=1}^{N_{\text{Schmidt}}} \sqrt{\nu_\alpha} |\nu_\alpha^F\rangle |\nu_\alpha^R\rangle, \quad (3.8)$$

where  $|\nu_\alpha^F\rangle$  and  $|\nu_\alpha^R\rangle$  are the eigenvectors of  $\rho$  for the left and right parts, respectively. SVD assures that the density matrices for both parts have the same eigenvalues  $\nu_\alpha$ . The number of coefficients is reduced from  $d_F d_R$  to  $N_{\text{Schmidt}} \leq \min(d_F, d_R)$  and in this manner an upper bound for the entanglement has been found. Eq. (3.8) is also known as the Schmidt decomposition and from it we can easily note that the number of non-zero eigenvalues is a measure of the entanglement. In other words, if there is only one eigenvalue different from zero, then we see that  $|\psi\rangle$  is a simple product of the left and right part and no entanglement is present between these two parts; this is not the case when the number of non-zero eigenvalues is larger than one and, therefore, there is entanglement. A more quantitative measure of the entanglement is given by the von Neumann entropy,

$$S \equiv -\text{Tr} \hat{\rho} \log_2 \hat{\rho} = - \sum_i^{N_{\text{Schmidt}}} \nu_i \log_2(\nu_i), \quad (3.9)$$

where  $\hat{\rho}$  stands for the reduced density matrix. In general we cannot know the behavior of the eigenvalues  $\nu_i$ . However, Eq. (3.9) can be used in order to get some insight. Note that since  $\nu_i > 0$  and  $\sum \nu_i = 1$ , then  $S \geq 0$  (that is the reason of the minus sign in the definition of  $S$ ). For an extremely fast decay, let us say  $\nu_1 = 1$  and the rest is zero, we have that  $S = 0$ . For the slowest decay case, where all  $\nu_i$  are the same,  $S = \log_2(d_F)$  is maximum. Note that  $S$  is not only a measure of the entanglement but it has also the typical behavior of an entropy:  $S = 0$  when the probability is one for one single outcome (no uncertainty), and  $S$  is maximum when the probabilities are equally distributed among all the outcomes (maximal uncertainty). Therefore we can say that the larger  $S$  is, the slower is the decay of the eigenvalues  $\nu_i$  and as a consequence we need a larger truncated dimension  $m$  in order to compute mean values with high precision. In other words, we can say that the number of eigenvectors we need to correctly describe the system is given by  $m \sim 2^S$ .

The behavior of  $S$  for systems with short range interactions can be derived using the area laws [30, 43–47]: 1) For ground state of systems with gap excitations, the entanglement entropy  $S$  is proportional to the area separating the system from its environment, that is,  $S \sim L^{D-1}$  with  $L$  the length of the system and  $D$  the spatial dimension. In this case and for 1D systems  $S$  is independent of  $L$  and then  $m$  is also constant. In more than 1D we have that  $S$  scales with  $L$  and hence the system is much more difficult to simulate. 2) For critical systems, conformal field theory [48, 49] predicts: in 1D,  $S \sim \log_2(L)$ ; for fermions in 2D,  $S \sim L \log_2(L)$ ; and for bosons in 2D,  $S \sim L$  is

not affected by criticality. In conclusion, in 1D, in one of the worse scenarios (i.e. at criticality) we have that  $S$  scales logarithmically with  $L$  in contrast to more than 1D where the scaling is linear. Therefore, the number of states  $m \sim 2^S$  needed to describe the system is constant (gapped systems) or increases linearly (at criticality) with  $L$  while in more than 1D  $m$  increases exponentially. This is the reason why DMRG is so successful in one dimension. The effect of long-range interactions is to increase  $S$ . An intuitive explanation is that, for example, a 1D lattice with long-range interaction can also be thought as a 2D lattice with short-range interactions.

Up to this point we have presented an introduction motivating the main features of the DMRG method. In the next section we are going deeper into the technical details. We divided this algorithm into two main parts: the static DMRG and the time-dependent DMRG (t-DMRG). In the static DMRG we focus in computing the ground-state properties of the system like the energy and correlation functions. In the t-DMRG we consider the time evolution of the system given by certain Hamiltonian and having prepared it in certain initial state.

### 3.1 Static DMRG

In this section we explain many technical details of how the DMRG method manages to compute ground-state properties of a one-dimensional system. We divide the static DMRG into an infinity algorithm, where the system size  $L$  is increased after every DMRG step, and a finite DMRG, where  $L$  is kept constant.

#### 3.1.1 Infinite DMRG

The main idea of the infinite DMRG consists of starting with a system small enough such that it can be solved exactly and then at every step we increase the system size by keeping only a reduced representation of the Hilbert space. As we explained before, this optimal representation is given by the eigenvectors of the reduced density matrix.

Let us divide the system into four parts: two sites and two blocks with the same size  $l$ , as it is shown in Fig. 3.3

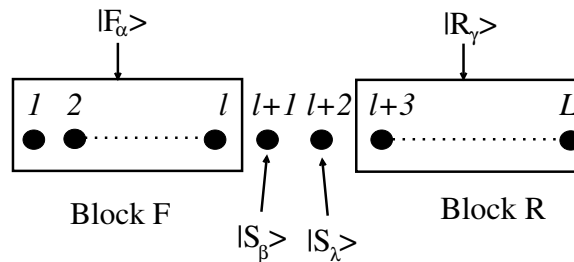


Figure 3.3: The system is divided into 4 subspaces: two blocks with the same size and two sites. Since each block has size  $l$ , the system size is  $L = 2l + 2$ .

Let us reduce the Hilbert space by associating to each block a set of  $m$  vectors, where  $m$  is smaller than the original dimension of the block subspace. We say that the set  $\{|F_\alpha\rangle\}$  represents the block F subspace and the set  $\{|R_\gamma\rangle\}$  represents the block R subspace. The indices  $\alpha$  and  $\gamma$  run from 1 to  $m$ . The sets  $\{|S_\beta\rangle\}$  and  $\{|S_\lambda\rangle\}$ , with  $\beta, \lambda = 1, \dots, d$ , represent the site subspace. Then, we can form a reduce space given by the set of vectors

$$\{|F_\alpha\rangle|S_\beta\rangle|S_\lambda\rangle|R_\gamma\rangle\}, \quad (3.10)$$

which we called superblock vectors. We can project the Hamiltonian  $H$  onto this reduced space by finding its matrix elements

$$H_{(\alpha' \beta' \lambda' \gamma'), (\alpha \beta \lambda \gamma)} = \langle F_{\alpha'} | \langle S_{\beta'} | \langle S_{\lambda'} | \langle R_{\gamma'} | H | F_{\alpha} \rangle | S_{\beta} \rangle | S_{\lambda} \rangle | R_{\gamma} \rangle. \quad (3.11)$$

We can diagonalize this projection of  $H$  using the Lanczos method [31, 50] to obtain the reduced ground state  $|\psi\rangle$  and its energy. In this basis  $|\psi\rangle$  can be written as

$$|\psi\rangle = \sum_{\alpha\beta\lambda\gamma} \psi_{\alpha\beta\lambda\gamma} |F_{\alpha}\rangle |S_{\beta}\rangle |S_{\lambda}\rangle |R_{\gamma}\rangle. \quad (3.12)$$

Let us define the new block as a block composed of one previous block (which comes from the previous DMRG step) and one more site (Fig. 3.4).

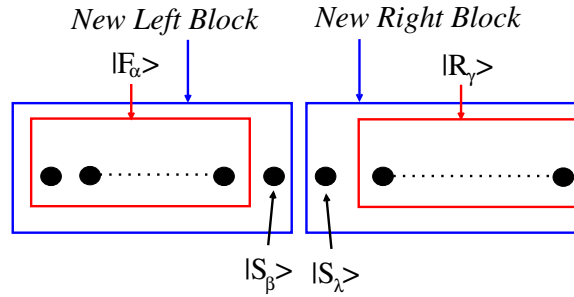


Figure 3.4: The new left block and the new right block.

Let us define  $|i\rangle \equiv |F_{\alpha}\rangle |S_{\beta}\rangle$  for the new left block and  $|j\rangle \equiv |S_{\lambda}\rangle |R_{\gamma}\rangle$  for the new right block, where  $i, j = 1, \dots, md$ . Since the vector set  $\{|i\rangle |j\rangle\}$  is also a basis of the superblock, we can rewrite the ground state  $|\psi\rangle$  in this basis as

$$|\psi\rangle = \sum_{i,j} \psi_{ij} |i\rangle |j\rangle. \quad (3.13)$$

As before, we define the reduced density matrix of the left block as

$$\rho = Tr_R |\psi\rangle \langle \psi|, \quad (3.14)$$

where the operator  $Tr_R$  is given by Eq. (3.4). Note that  $\rho$  acts only on the new left block because we have eliminated the part which acts on the right block by taking the trace over the new right block. After some algebra we can obtain the matrix elements of  $\rho$ :

$$\rho_{ii'} = \langle i | \rho | i' \rangle = \sum_{k=1}^{md} \psi_{ik} \psi_{i'k}^*. \quad (3.15)$$

We can diagonalize  $\rho$  and obtain its eigenvectors  $|\nu_i\rangle$  and its eigenvalues  $\nu_i$  with  $i = 1, \dots, md$ . At this point we truncate the new left block subspace by keeping only  $m'$  of the largest eigenvalues  $\nu_i$  instead of all  $md$ . In order to have a criteria of how many eigenvalues we should keep, we can take into account that the trace of  $\rho$  is equal to one. Therefore, the sum of its eigenvalues  $\nu_i$  is equal to one:

$$\sum_{i=1}^{md} \nu_i = 1 \quad \Rightarrow \quad \sum_{i=1}^{m'} \nu_i + \sum_{i=m'+1}^{md} \nu_i = 1. \quad (3.16)$$

If we define

$$\epsilon \equiv \sum_{i=m'+1}^{md} \nu_i \Rightarrow \epsilon = 1 - \sum_{i=1}^{m'} \nu_i, \quad (3.17)$$

as the error, then we can determinate  $m'$  for a given  $\epsilon$ . The error  $\epsilon$  is also called discarded weight. Now we associate the first  $m'$  eigenvectors  $|\nu_i\rangle$  with the new left block, i.e.  $|F_\alpha\rangle_{l+1} = |\nu_i\rangle$  where now  $\alpha$  runs from 1 to  $m'$  and the subindex  $l+1$  just refers to the corresponding DMRG step (Note that  $|F_\alpha\rangle$  has an implicit subindex  $l$  but we have avoided it to not overload notation. Similarly,  $m$  and  $m'$  correspond to the DMRG steps  $l$  and  $l+1$ , respectively). To find out  $|R_\gamma\rangle_{l+1}$  we can do the same as for  $|F_\alpha\rangle_{l+1}$  but, instead of taking the trace over the right block in Eq. (3.14), we take the trace over the left block, which defines the reduced density matrix of the right block.

Now we increase the system size by adding two more site in the middle of the chain and then we can define the new superblock basis as

$$\{|F_\alpha\rangle_{l+1}|S_\beta\rangle_{l+1}|S_\lambda\rangle_{l+1}|R_\gamma\rangle_{l+1}\}. \quad (3.18)$$

We can now find the matrix elements (Eq. 3.11) of the Hamiltonian using this new superblock basis and repeat everything again and again until we reach the desired system size. In the next section we will explain how to obtain these new matrix elements in terms of the previous ones.

The above described procedure of going from a reduced Hilbert space, labeled by  $l$ , to the next one is what we called a DMRG step. This is summarized in Fig. 3.5. Since, at the beginning of the DMRG method the block's size  $l = 1$  and after every DMRG step each block has one more site, we can identify the DMRG step with the block's size.

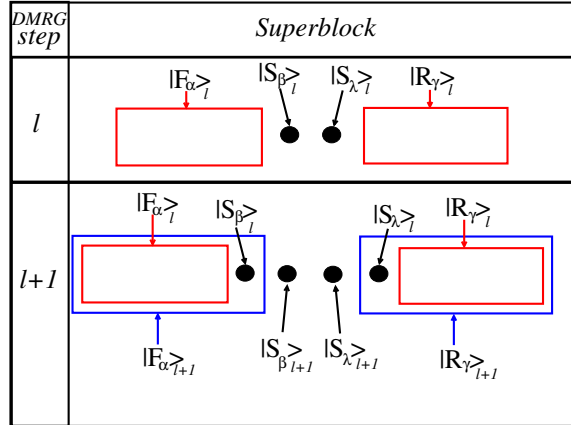


Figure 3.5: Change of the superblock going from one DMRG step to the next one. The red blocks stand for the old blocks and the blue blocks for the new ones (after adding one more site to each of them).  $|F_\alpha\rangle$  and  $|R_\gamma\rangle$  are given by the eigenvectors of the reduced density matrix of the corresponding block. The superblock increases by two sites after each DMRG step.

### 3.1.2 Recursive relations for the Hamiltonian

In this section we will discuss the iterative relations for the Hamiltonian in order to show how we can proceed from one DMRG step to the next one.

Let us assume that we have only nearest neighbor interactions. Then, we can split the Hamiltonian in several terms:

$$H = \underbrace{H_F + H_{S1} + H_{S2} + H_R}_{\text{non-interacting terms}} + \underbrace{H_{FS1} + H_{S1S2} + H_{S2R}}_{\text{interacting terms}}. \quad (3.19)$$

This splitting of  $H$  is also shown in Fig. 3.6.  $H_F$  is the part of  $H$  that acts only on the left block  $F$ ,  $H_R$  acts only on the right block  $R$ ,  $H_{S1}$  acts only on the site  $S1$ , and  $H_{S2}$  acts only on the site  $S2$ .  $H_{FS1}$  represents the interaction between the left block  $F$  and the site  $S1$ ,  $H_{S1S2}$  represents the interaction between the two sites, and  $H_{S2R}$  represents the interaction between the site  $S2$  and the right block  $R$ .

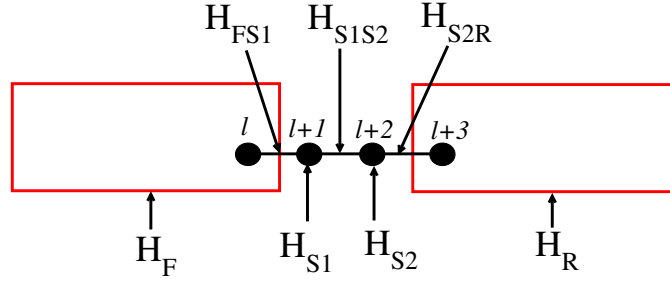


Figure 3.6: Splitting of the Hamiltonian considering only nearest neighbor interactions.

We recall that the basis for the superblock is given by the set of vectors  $\{|F_\alpha\rangle|S_\beta\rangle|S_\lambda\rangle|R_\gamma\rangle\}$  where  $\alpha, \gamma = 1, \dots, m$  and  $\beta, \lambda = 1, \dots, d$ . Each of these vectors can be labeled by  $(\alpha, \beta, \lambda, \gamma)$ . The matrix elements of  $H$  in this basis are given by

$$\begin{aligned} [H]_{(\alpha'\beta'\lambda'\gamma'),(\alpha\beta\lambda\gamma)} &\equiv \langle F_{\alpha'} | \langle S_{\beta'} | \langle S_{\lambda'} | \langle R_{\gamma'} | H | F_\alpha \rangle | S_\beta \rangle | S_\lambda \rangle | R_\gamma \rangle \\ &= [H_F]_{\alpha'\alpha} \delta_{\beta'\beta} \delta_{\lambda'\lambda} \delta_{\gamma'\gamma} + [H_{S1}]_{\beta'\beta} \delta_{\alpha'\alpha} \delta_{\lambda'\lambda} \delta_{\gamma'\gamma} + [H_{S2}]_{\lambda'\lambda} \delta_{\alpha'\alpha} \delta_{\beta'\beta} \delta_{\gamma'\gamma} + [H_R]_{\gamma'\gamma} \delta_{\alpha'\alpha} \delta_{\beta'\beta} \delta_{\lambda'\lambda} \\ &\quad + [H_{FS1}]_{(\alpha'\beta'),(\alpha\beta)} \delta_{\lambda'\lambda} \delta_{\gamma'\gamma} + [H_{S1S2}]_{(\beta'\lambda'),(\beta\lambda)} \delta_{\alpha'\alpha} \delta_{\gamma'\gamma} + [H_{S2R}]_{(\lambda'\gamma'),(\lambda\gamma)} \delta_{\alpha'\alpha} \delta_{\beta'\beta}, \end{aligned} \quad (3.20)$$

where we have used the fact that each part of  $H$  acts in its particular subspace and we have defined the following matrices

$$[H_F]_{\alpha'\alpha} \equiv \langle F_{\alpha'} | H_F | F_\alpha \rangle, \quad (3.21)$$

$$[H_{S1}]_{\beta'\beta} \equiv \langle S_{\beta'} | H_{S1} | S_\beta \rangle, \quad (3.22)$$

$$[H_{S2}]_{\lambda'\lambda} \equiv \langle S_{\lambda'} | H_{S2} | S_\lambda \rangle, \quad (3.23)$$

$$[H_R]_{\gamma'\gamma} \equiv \langle R_{\gamma'} | H_R | R_\gamma \rangle, \quad (3.24)$$

$$[H_{FS1}]_{(\alpha'\beta'),(\alpha\beta)} \equiv \langle F_{\alpha'} | \langle S_{\beta'} | H_{FS1} | F_\alpha \rangle | S_\beta \rangle, \quad (3.25)$$

$$[H_{S1S2}]_{(\beta'\lambda'),(\beta\lambda)} \equiv \langle S_{\beta'} | \langle S_{\lambda'} | H_{S1S2} | S_\beta \rangle | S_\lambda \rangle, \quad (3.26)$$

$$[H_{S2R}]_{(\lambda'\gamma'),(\lambda\gamma)} \equiv \langle S_{\lambda'} | \langle R_{\gamma'} | H_{S2R} | S_{\lambda} \rangle | R_{\gamma} \rangle. \quad (3.27)$$

The advantage of writing the Hamiltonian in this form is that now we have to diagonalize few matrices which are smaller than the entire matrix representation of the Hamiltonian. In this form, we can save memory and time during the diagonalization procedure.

Let us assume that we know the matrices (3.21) - (3.27) in the DMRG step  $l$  and we want to find the same matrices but in the step  $l + 1$ . Let us start with the matrix

$$\left[ H_F^{(l+1)} \right]_{\alpha'\alpha} \equiv {}_{l+1} \langle F_{\alpha'} | H_F | F_{\alpha} \rangle_{l+1}, \quad (3.28)$$

where  $\alpha$  and  $\alpha'$  go from 1 to  $m'$ .  $m$  and  $m'$  are the number of eigenvectors of the reduced density matrix which were chosen to represent the block in the step  $l$  and the block in the step  $l + 1$ , respectively. Since the set  $\{|F_i\rangle_l | S_j\rangle_l\}$  forms a basis for the new left block, we can write  $|F_{\alpha}\rangle_{l+1}$  as

$$|F_{\alpha}\rangle_{l+1} = \sum_{i=1}^m \sum_{j=1}^d a_{ij}^{\alpha} |F_i\rangle_l |S_j\rangle_l. \quad (3.29)$$

We have to keep in mind that the coefficients  $a_{ij}^{\alpha}$  depend also on the DMRG step  $l$ . Since  $H_F^{(l+1)}$  acts on the new left block space, we can also split it as

$$H_F^{(l+1)} = H_F^{(l)} + H_{S1}^{(l)} + H_{FS1}^{(l)}. \quad (3.30)$$

We can see in Fig. 3.7 how we can make this splitting. By inserting Eq. 3.29 and 3.30 into Eq. 3.28

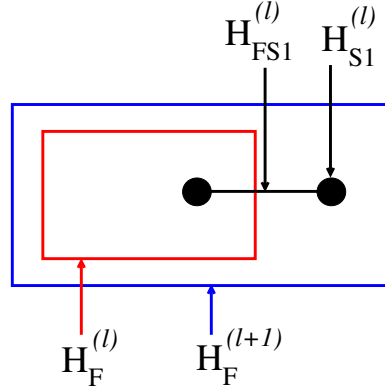


Figure 3.7: Splitting of the Hamiltonian  $H_F^{(l+1)}$ .

we obtain

$$\begin{aligned} \left[ H_F^{(l+1)} \right]_{\alpha'\alpha} &= \sum_{i,k=1}^m \sum_{j,q=1}^d a_{ij}^{\alpha} (a_{kq}^{\alpha'})^* {}_l \langle F_k | {}_l \langle S_q | H_F^{(l+1)} | F_i \rangle_l | S_j \rangle_l \\ &= \sum_{i,k=1}^m \sum_{j,q=1}^d a_{ij}^{\alpha} \left[ a_{kq}^{\alpha'} \right]^* \left\{ {}_l \langle F_k | H_F^{(l)} | F_i \rangle_l \delta_{qj} + {}_l \langle S_q | H_{S1}^{(l)} | S_j \rangle_l \delta_{ki} + {}_l \langle F_k | {}_l \langle S_q | H_{FS1}^{(l)} | F_i \rangle_l | S_j \rangle_l \right\}. \end{aligned} \quad (3.31)$$

If we define

$$\begin{aligned} \left[ \hat{H}_F^{(l+1)} \right]_{(kq)(ij)} &\equiv {}_l \langle F_k | {}_l \langle S_q | H_F^{(l+1)} | F_i \rangle_l | S_j \rangle_l, \\ \left[ H_F^{(l)} \right]_{ki} &\equiv {}_l \langle F_k | H_F^{(l)} | F_i \rangle_l, \\ \left[ H_{S1}^{(l)} \right]_{qj} &\equiv {}_l \langle S_q | H_{S1}^{(l)} | S_j \rangle_l, \\ \left[ H_{FS1}^{(l)} \right]_{(kq)(ij)} &\equiv {}_l \langle F_k | {}_l \langle S_q | H_{FS1}^{(l)} | F_i \rangle_l | S_j \rangle_l, \end{aligned}$$

then, from Eq. (3.31) we can obtain

$$\left[ \hat{H}_F^{(l+1)} \right]_{(kq)(ij)} = \left[ H_F^{(l)} \right]_{ki} \delta_{qj} + \left[ H_{S1}^{(l)} \right]_{qj} \delta_{ki} + \left[ H_{FS1}^{(l)} \right]_{(kq)(ij)}, \quad (3.32)$$

where  $i, k = 1, \dots, m$  and  $j, q = 1, \dots, d$ . We have put a hat on  $H_F$  to distinguish the matrix  $\left[ \hat{H}_F^{(l+1)} \right]_{(kq)(ij)}$ , which represents the operator  $H_F$  before truncation, from the matrix  $\left[ H_F^{(l+1)} \right]_{\alpha'\alpha}$ , which represents  $H_F$  after truncation.

Let us associate with each vector  $|F_i\rangle_l |S_j\rangle_l$  an index  $p(i, j)$  which determines the order of the elements of this basis. Then, the relation  $(i, j) \rightarrow p$  is an one to one function. We will see in Sec. 3.1.3 that this relation is useful for considering the conservation of quantum numbers. Therefore, we can say  $|p\rangle_l \equiv |F_i\rangle_l |S_j\rangle_l$  and  $a_{ij}^\alpha \rightarrow a_p^\alpha$  and rewrite the Eq. (3.29) as

$$|F_\alpha\rangle_{l+1} = \sum_p a_p^\alpha |p\rangle_l.$$

We can also redefine  $\left[ \hat{H}_F^{(l+1)} \right]_{(kq)(ij)} \rightarrow \left[ \hat{H}_F^{(l+1)} \right]_{p'p}$ . Inserting into Eq. (3.28) we obtain

$$\left[ H_F^{(l+1)} \right]_{\alpha'\alpha} = \sum_{p'} \sum_p (a_{p'}^{\alpha'})^* \left[ \hat{H}_F^{(l+1)} \right]_{p'p} a_p^\alpha. \quad (3.33)$$

It is important to remark that the indices  $\alpha'$  and  $\alpha$  run from 1 to  $m^{l+1}$ , where  $m^{l+1}$  is different from  $m$ . Remember that  $m$  corresponds to the step  $l$ , whereas  $m^{l+1}$  to the step  $l+1$ . We can define the matrix  $\left[ O_F^{(l)} \right]_{p\alpha} \equiv a_p^\alpha$  and rewrite Eq. (3.33) in matrix notation as

$$\left[ H_F^{(l+1)} \right] = \left[ O_F^{(l)} \right]^* \left[ \hat{H}_F^{(l+1)} \right] \left[ O_F^{(l)} \right]. \quad (3.34)$$

The subindex  $F$  denotes that we are working on the left block. We have assumed that  $\left[ O_F^{(l)} \right]$  depends on  $l$  because we have to remember that the coefficients  $a_p^\alpha$  depend on  $l$ . Note that the columns of the matrix  $\left[ O_F^{(l)} \right]$  are the eigenvectors of the reduced density matrix. In Eq. (3.34) the matrix  $\left[ H_F^{(l+1)} \right]$  corresponds to the reduced Hamiltonian  $H_F$  which is truncated by using the matrix  $\left[ O_F^{(l)} \right]$ .

To summarize, if we know  $\left[ H_F^{(l)} \right]_{ki}$ ,  $\left[ H_{S1}^{(l)} \right]_{qj}$  and  $\left[ H_{FS1}^{(l)} \right]_{(kq)(ij)}$  from the previous step, we can obtain  $\left[ \hat{H}_F^{(l+1)} \right]_{p'p}$  by using the Eq. (3.32) and the relation  $(i, j) \rightarrow p$ ; and if we know  $\left[ \hat{H}_F^{(l+1)} \right]_{p'p}$  and the coefficients  $a_p^\alpha$  of the vector  $|F_\alpha\rangle_{l+1}$ , we can calculate  $\left[ H_F^{(l+1)} \right]_{\alpha'\alpha}$  by using Eq. (3.33).

The matrices  $\left[ H_{S1}^{(l)} \right]_{qj}$  and  $\left[ H_{S2}^{(l)} \right]_{qj}$  do not depend on the DMRG step, then we just have to store them only once at the beginning. Since  $\left[ H_{S1}^{(l)} \right]_{qj} = \left[ H_{S2}^{(l)} \right]_{qj}$ , only one of them needs to be stored.

In order to find out the recursive relation for  $H_R^{(l+1)}$ , we can proceed in the same manner as in  $H_F^{(l+1)}$ . Since  $\{|S_i\rangle_l |R_j\rangle_l\}$  form a basis of the new right block,  $|R_\gamma\rangle_{l+1}$  can be written as

$$|R_\gamma\rangle_{l+1} = \sum_{i=1}^d \sum_{j=1}^m b_{ij}^{\gamma'} |S_i\rangle_l |R_j\rangle_l. \quad (3.35)$$

We can split the  $H_R^{(l+1)}$  into (see Fig. 3.8)

$$H_R^{(l+1)} = H_R^{(l)} + H_{S2}^{(l)} + H_{S2R}^{(l)} \quad (3.36)$$

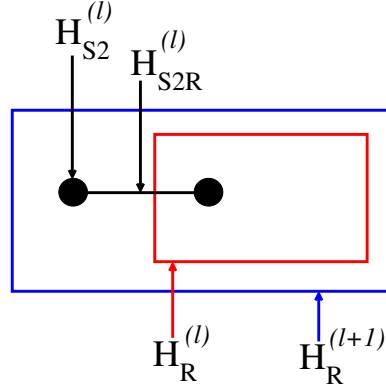


Figure 3.8: Splitting of the Hamiltonian  $H_R^{(l+1)}$ .

$$\begin{aligned} &\Rightarrow \left[ H_R^{(l+1)} \right]_{\gamma'\gamma} \equiv {}_{l+1}\langle R_{\gamma'} | H_R^{(l+1)} | R_\gamma \rangle_{l+1} \\ &= \sum_{i,k=1}^d \sum_{j,q=1}^m b_{ij}^{\gamma'} (b_{kq}^{\gamma'})^* \left\{ {}_l\langle R_q | H_R^{(l)} | R_j \rangle_l \delta_{ki} + {}_l\langle S_k | H_{S2}^{(l)} | S_i \rangle_l \delta_{qj} + {}_l\langle S_k | {}_l\langle R_q | H_{S2R}^{(l)} | S_i \rangle_l | R_j \rangle_l \right\}. \quad (3.37) \\ &= \sum_{i,k=1}^d \sum_{j,q=1}^m b_{ij}^{\gamma'} (b_{kq}^{\gamma'})^* \left\{ {}_l\langle R_q | H_R^{(l)} | R_j \rangle_l \delta_{ki} + {}_l\langle S_k | H_{S2}^{(l)} | S_i \rangle_l \delta_{qj} + {}_l\langle S_k | {}_l\langle R_q | H_{S2R}^{(l)} | S_i \rangle_l | R_j \rangle_l \right\}. \end{aligned}$$

We define

$$\begin{aligned} \left[ \hat{H}_R^{(l+1)} \right]_{(kq)(ij)} &\equiv {}_l\langle S_k | {}_l\langle R_q | H_R^{(l+1)} | S_i \rangle_l | R_j \rangle_l, \\ \left[ H_R^{(l)} \right]_{qj} &\equiv {}_l\langle R_q | H_R^{(l)} | R_j \rangle_l, \\ \left[ H_{S2}^{(l)} \right]_{ki} &\equiv {}_l\langle S_k | H_{S2}^{(l)} | S_i \rangle_l, \\ \left[ H_{S2R}^{(l)} \right]_{(kq)(ij)} &\equiv {}_l\langle S_k | {}_l\langle R_q | H_{S2R}^{(l)} | S_i \rangle_l | R_j \rangle_l. \end{aligned}$$

From this definitions and from Eq. (3.37) we can obtain

$$\left[ \hat{H}_R^{(l+1)} \right]_{(kq)(ij)} = \left[ H_R^{(l)} \right]_{qj} \delta_{ki} + \left[ H_{S2}^{(l)} \right]_{ki} \delta_{qj} + \left[ H_{S2R}^{(l)} \right]_{(kq)(ij)}. \quad (3.38)$$

As we illustrated before, we define the relation  $p(i, j)$  which gives us the order of the basis  $\{|p\rangle_l\} \equiv \{|S_i\rangle_l |R_j\rangle_l\}$ . We replace also  $b_{ij}^\gamma \rightarrow b_p^\gamma$  and  $\left[ H_R^{(l+1)} \right]_{(kq)(ij)} \rightarrow \left[ H_R^{(l+1)} \right]_{p'p}$ . Inserting them into Eq. (3.37) and using Eq. (3.38) we obtain

$$\left[ H_R^{(l+1)} \right]_{\gamma'\gamma} = \sum_{p'} \sum_p (b_{p'}^{\gamma'})^* \left[ \hat{H}_R^{(l+1)} \right]_{p'p} b_p^\gamma, \quad (3.39)$$

where  $\gamma', \gamma = 1, \dots, m^{l+1}$ . By using Eq. (3.38) and (3.39), we can obtain  $\left[ H_R^{(l+1)} \right]_{\gamma'\gamma}$ .

We can also define the matrix  $\left[ O_R^{(l)} \right]_{p\gamma} \equiv b_p^\gamma$  and rewrite Eq. (3.39) in matrix notation as

$$\left[ H_R^{(l+1)} \right] = \left[ O_R^{(l)} \right]^* \left[ \hat{H}_R^{(l+1)} \right] \left[ O_R^{(l)} \right]. \quad (3.40)$$

At this point, we have all the recursive relations in order to obtain the non-interacting terms. Let us see now the interacting terms. We start with the matrix

$$\left[ H_{FS1}^{(l+1)} \right]_{(\alpha'\beta'),(\alpha\beta)} \equiv {}_{l+1}\langle F_{\alpha'} | {}_{l+1}\langle S_{\beta'} | H_{FS1}^{(l+1)} | F_{\alpha} \rangle_{l+1} | S_{\beta} \rangle_{l+1}. \quad (3.41)$$

Since we have only nearest neighbor interactions,  $H_{FS1}$  acts only on the sites  $|S_j\rangle_l$  and  $|S_{\beta}\rangle_{l+1}$  (Fig. 3.9).

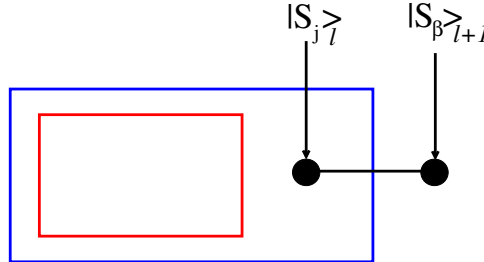


Figure 3.9:  $H_{FS1}$  acts only on the sites  $|S_j\rangle_l$  and  $|S_{\beta}\rangle_{l+1}$ .

Therefore  $H_{FS1} \equiv H_{SS'}$ , where  $S$  corresponds to the site  $|S_j\rangle_l$  and  $S'$  to the site  $|S_{\beta}\rangle_{l+1}$ . After writing  $|F_{\alpha}\rangle_{l+1}$  in the basis  $\{|F_i\rangle_l |S_j\rangle_l\}$  and inserting into Eq. (3.41) we obtain:

$$\begin{aligned} \left[ H_{FS1}^{(l+1)} \right]_{(\alpha'\beta'),(\alpha\beta)} &= \sum_{i,k=1}^m \sum_{j,q=1}^d a_{ij}^\alpha (a_{kq}^{\alpha'})^* {}_l\langle F_k | {}_l\langle S_q | {}_{l+1}\langle S_{\beta'} | H_{SS'} | F_i \rangle_l | S_j \rangle_l | S_{\beta} \rangle_{l+1} \\ &= \sum_{i,k=1}^m \sum_{j,q=1}^d a_{ij}^\alpha (a_{kq}^{\alpha'})^* {}_l\langle S_q | {}_{l+1}\langle S_{\beta'} | H_{SS'} | S_j \rangle_l | S_{\beta} \rangle_{l+1} \delta_{ki}. \end{aligned} \quad (3.42)$$

Since, in most of the cases, the basis for each site and the actual action of  $H_{SS'}$  do not depend on the sites, then the matrix

$$\left[ H_{SS'} \right]_{(q\beta')(j\beta)} \equiv {}_l\langle S_q | {}_{l+1}\langle S_{\beta'} | H_{SS'} | S_j \rangle_l | S_{\beta} \rangle_{l+1}, \quad (3.43)$$

does not depend on the DMRG step and stands only for the interaction between two sites as we have already seen in Eq. (3.20). With this notation and taking into account the action of  $\delta_{ki}$ , Eq. (3.42) becomes

$$\left[ H_{FS1}^{(l+1)} \right]_{(\alpha'\beta'),(\alpha\beta)} = \sum_{i=1}^m \sum_{j,q=1}^d a_{ij}^\alpha (a_{iq}^{\alpha'})^* [H_{SS'}]_{(q\beta')(j\beta)}, \quad (3.44)$$

where  $\alpha', \alpha = 1, \dots, m^{l+1}$  and  $\beta', \beta$  are the indices for the new left block. We could think that Eq. (3.44) does not depend on the DMRG step but it is not true because we have to keep in mind that the coefficients  $a_{ij}^\alpha$  do depend on the DMRG step.

In the same way as in  $\left[ H_{FS1}^{(l+1)} \right]_{(\alpha'\beta')}$ , we can find out the recursive relation for the interaction between the site  $|S_\lambda\rangle$  and the right block:

$$\begin{aligned} \left[ H_{S2R}^{(l+1)} \right]_{(\lambda'\gamma')(\lambda\gamma)} &\equiv {}_{l+1}\langle S_{\lambda'} | {}_{l+1}\langle R_{\gamma'} | H_{S2R}^{(l+1)} | S_\lambda \rangle_{l+1} | R_\gamma \rangle_{l+1} \\ &= \sum_{i,k=1}^d \sum_{j=1}^m b_{ij}^\gamma (b_{kj}^{\gamma'})^* [H_{SS'}]_{(\lambda'k)(\lambda i)}, \end{aligned} \quad (3.45)$$

where  $\gamma', \gamma = 1, \dots, m^{l+1}$  and  $\lambda', \lambda$  are the indices for the new right block. Finally, with Eqs. (3.33), (3.39), (3.44) and (3.45) we have obtained all the recursive relations necessary to obtain the Hamiltonian  $H^{(l+1)}$  given by Eq. (3.20).

### 3.1.3 Quantum numbers conservation and the reduced density matrix

We can reduce even more the size of the space of states, if we use the conservation of quantum numbers. In this way, we restrict the problem to a certain sector with a defined set of quantum numbers. Let us start considering only the conservation of the particle number (i.e. assuming that  $[H, N] = 0$ ). The magnetization conservation can be treated in the same manner and we will include it latter on.

First of all, let us remind that the ground state can be written as:

$$|\psi\rangle = \sum_{i,j} \psi_{ij} |i\rangle |j\rangle, \quad (3.46)$$

where  $|i\rangle$  represents the new left block and  $|j\rangle$  represents the new right block. At the beginning of the DMRG, we choose an initial superblock basis such that its vectors are eigenvectors of the number operator  $\hat{N}$  with a specific number of particles  $N$ . The vectors  $|i\rangle$  and  $|j\rangle$  have also a defined quantum number when the DMRG starts. After diagonalizing the reduced density matrix  $\rho$  for the left block, its eigenvectors can be written as a linear combination of  $|i\rangle$ :

$$|F_\alpha\rangle = \sum_i c_i |i\rangle. \quad (3.47)$$

Since the set  $\{|i\rangle\}$  is the basis for a block, not all the  $|i\rangle$  belong to the same subspace with a given quantum number. Therefore, it is not obvious that  $|F_\alpha\rangle$  has a defined quantum number because it could be a linear combination of vector with different quantum numbers.

For instance, the vectors

$$\{|1100\rangle, |1010\rangle, |1001\rangle, |0110\rangle, |0101\rangle, |0011\rangle\},$$

are all the possible superblock vectors for a system with 4 sites and 2 particles; and the vectors

$$\{|i\rangle\} = \left\{ \underbrace{|00\rangle}_{n=0}, \underbrace{|10\rangle}_{n=1}, \underbrace{|01\rangle}_{n=1}, \underbrace{|11\rangle}_{n=2} \right\},$$

are the block vectors for the same system and they have quantum numbers between  $n = 0$  and  $n = 2$ . Then,  $|F_\alpha\rangle$  might be a linear combination of vectors with different quantum numbers.

In order to answer the question whether the eigenvectors of  $\rho$  have well defined quantum numbers or not [34], we know that the number operator  $\hat{N}$  is an observable (that is, its eigenvectors form a complete basis of the Hilbert space), therefore, we can write the ground state  $|\psi\rangle$  as a linear combination of the eigenvectors of  $\hat{N}$ :

$$|\psi(N)\rangle = \sum_{\substack{n_1, n_2 \\ n_1 + n_2 = N}} \sum_{\alpha, \beta} c(n_1, \alpha; n_2, \beta) |n_1, \alpha\rangle |n_2, \beta\rangle, \quad (3.48)$$

where  $n_1$  is the quantum number of the vector  $|n_1, \alpha\rangle$  and  $n_2$  for the vector  $|n_2, \beta\rangle$ , i.e.

$$\hat{N}|n_1, \alpha\rangle = n_1|n_1, \alpha\rangle \text{ and } \hat{N}|n_2, \beta\rangle = n_2|n_2, \beta\rangle.$$

The vector  $|n_1, \alpha\rangle$  stands for the left block and the vector  $|n_2, \beta\rangle$  for the right block. The indices  $\alpha$  and  $\beta$  stand for additional quantum numbers. If the constraint  $n_1 + n_2 = N$  is not fulfilled, then  $c(n_1, \alpha; n_2, \beta) = 0$ .

Similarly to Eq. (3.15), the matrix elements of  $\rho$  are given by

$$\rho_{(n_1, \alpha)(n'_1, \alpha')} = \sum_{n_2, \beta} c(n_1, \alpha; n_2, \beta) c(n'_1, \alpha'; n_2, \beta)^*. \quad (3.49)$$

If  $\rho$  is different from zero, then  $c(n_1, \alpha; n_2, \beta)$  and  $c(n'_1, \alpha'; n_2, \beta)$  have to be also different from zero for at least one index  $(n_1, \alpha; n_2, \beta)$  and  $(n'_1, \alpha'; n_2, \beta)$ , respectively. We also know that

$$c(n_1, \alpha; n_2, \beta) \neq 0 \iff n_1 + n_2 = N$$

and

$$c(n'_1, \alpha'; n_2, \beta) \neq 0 \iff n'_1 + n_2 = N$$

$$\implies N = n_1 + n_2 = n'_1 + n_2 \implies n'_1 = n_1.$$

Hence, the unique non-zero matrix elements  $\rho_{(n_1, \alpha)(n'_1, \alpha')}$  are those that satisfy  $n'_1 = n_1$ . In other words,  $\rho$  is block diagonal in the quantum numbers (or eigenvalues)  $n_1$ . Then, a common basis of eigenvector of  $\hat{N}$  and  $\rho$  exist and, for this reason, these eigenvectors have well defined quantum number  $n_1$ . Another consequence of this fact is that  $\rho$  and  $\hat{N}$  commute.

If we now include the magnetization, we can prove in the same way that  $[\rho, M_z] = 0$ , where  $M_z = \sum S_i^z$ . This last relation gives us the same consequences (obtained for the particle number) for the z-magnetization conservation.

In order to obtain the block diagonal form of  $\rho$  (Fig. 3.10) we have to arrange the basis, in which  $\rho$  is written, such that all the vectors with a given pair of quantum numbers  $(n_i, m_j)$  are in consecutive order. This form of writing  $\rho$  has the advantage that we can diagonalize each block separately instead of diagonalize the entire matrix. In this manner, we can save even more memory and time.

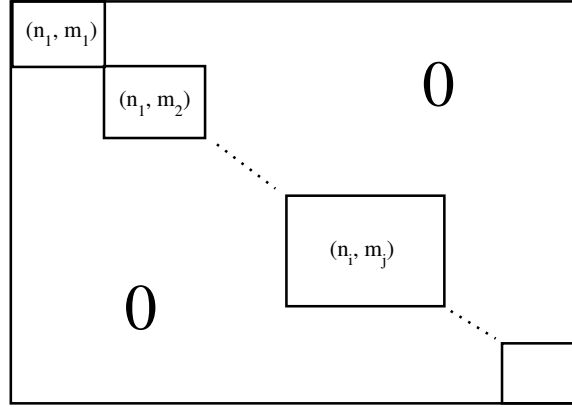


Figure 3.10: Block diagonal form of the reduced density matrix. Each block is labeled by a pair of indices  $(n_i, m_j)$ , where  $n_i$  is the quantum number for the number of particles and  $m_j$  is the quantum number for the z-magnetization.

Therefore, we can carry out the DMRG in a restricted subspace (with constant  $N$  and  $M_z$ ) because in every DMRG step we have always states  $|F_\alpha\rangle$ ,  $|S_\beta\rangle$ ,  $|S_\lambda\rangle$  and  $|R_\gamma\rangle$  with well defined quantum numbers.

In order to build up the superblock basis, we have to make the tensor product  $|F_\alpha\rangle|S_\beta\rangle|S_\lambda\rangle|R_\gamma\rangle$  taking into account the constraints

$$n_\alpha + n_\beta + n_\lambda + n_\gamma = N, \quad (3.50)$$

and

$$m_\alpha + m_\beta + m_\lambda + m_\gamma = M_z, \quad (3.51)$$

where  $n_\alpha$  and  $m_\alpha$  are the quantum numbers (particle number and magnetization, respectively) for the vector  $|F_\alpha\rangle$ ,  $n_\beta$  and  $m_\beta$  for  $|S_\beta\rangle$ ,  $n_\lambda$  and  $m_\lambda$  for  $|S_\lambda\rangle$ ,  $n_\gamma$  and  $m_\gamma$  for  $|R_\gamma\rangle$ .

We remind that each vector  $|F_\alpha\rangle|S_\beta\rangle|S_\lambda\rangle|R_\gamma\rangle$  can be labeled by a set of indices  $(\alpha, \beta, \lambda, \gamma)$ . However, and for computational reasons, we need a one to one relation  $(\alpha, \beta, \lambda, \gamma) \leftrightarrow p$  in order to arrange the superblock basis. The index  $p$  stores the order of the elements of the basis. If a given superblock vector fulfills the constraint, we store its position in  $p$  (starting from 1). If the constraint is not fulfilled, we set  $p = 0$ . In this manner, we can select and identify which vectors do satisfy the constraints and which ones do not. Actually, we do not need the superblock basis but only the relation  $(\alpha, \beta, \lambda, \gamma) \leftrightarrow p$ , which is needed to perform the Lanczos multiplication and to obtain the reduced density matrix.

The quantum number conservation can also be taken into account for the new blocks basis due to the block diagonal structure of  $\rho$ . In that case, we need also a relation  $(\alpha, \beta) \longleftrightarrow p_{left}$  for the new left block basis, and a relation  $(\lambda, \gamma) \leftrightarrow p_{right}$  for the new right block basis, to help us to identify the different subsectors with quantum numbers  $(n_\alpha + n_\beta, m_\alpha + m_\beta)$  for the new left block, and  $(n_\lambda + n_\gamma, m_\lambda + m_\gamma)$  for the new right block.

Hence, the restriction to a certain subspace of the superblock space and the block diagonal form of the reduced density matrix make the quantum numbers conservation an important aspect of the DMRG because it allow us to increase substantially the number of sites and particles to be treated.

### 3.1.4 Finite DMRG Algorithm

The steps of this algorithm are similar to the infinite DMRG. In this case, and during each DMRG step, we keep the size of the system constant by increasing one block and decreasing the another one. In order to have a system with finite size, we grow the system by using the infinite algorithm until the desired number of sites is reached. There is no reflection symmetry any more.

When the left block is growing, we say that the system is swept from the left to the right (Fig. 3.12). In the same manner, we define the right-left sweep (Fig. 3.13). When one system's extreme is reached, we switch the sweep direction. By sweeping several times, the ground state and its energy can be improved.

We denote the new left block information as  $I^{left}$ , which contains the matrix  $\hat{H}_F$  (Eq. (3.32)), the block dimension  $m_{left}$ , the indices relations  $(\alpha, \beta) \longleftrightarrow p_{left}$  and the quantum numbers for each vector  $|F_\alpha\rangle$ . Similarly, we denote the new right block information as  $I^{right}$ , which contains the matrix  $\hat{H}_R$  (Eq. (3.38)), the block dimension  $m_{right}$ , the indices relations  $(\lambda, \gamma) \leftrightarrow p_{right}$  and the quantum numbers for each vector  $|R_\gamma\rangle$ .

Since the one-site basis does not change during the whole DMRG procedure, the matrices  $H_{S1}$ ,  $H_{S2}$  and  $H_{S1S2}$  do not change either.

In the following we explain in more detail this algorithm which consist mainly of three parts: the right-left sweep immediately after the infinite algorithm, the left-right sweep, and the right-left sweep.

- The right-left sweep immediately after the infinite algorithm:
  1. Firstly, we carry out the infinite DMRG until the desired system size  $L$  is reached. Store the informations  $I^{left}[l]$  and  $I^{right}[l]$  for  $l = 1, \dots, \frac{L}{2} - 1$ . In this part, the left block size  $l$  and the right block size  $l'$  are the same ( $l = l'$ )(see Fig. 3.11). Note that  $L = 2l + 2$ .
  2. Use  $I^{left}[l]$ ,  $I^{right}[l']$  (with  $l = l' = \frac{L}{2} - 1$ ) and the superblock indices relation  $(\alpha, \beta, \lambda, \gamma) \leftrightarrow p$  (with this relation the quantum number conservation is taken into account) to obtain the superblock Hamiltonian (3.20). Diagonalize  $H$  by using the Lanczos method and obtain the ground state  $|\psi\rangle$  and its energy  $E_0$ . (Although the truncation allows a significant reduction of the Hilbert space, its dimension is still too large to use full exact diagonalization; for this reason we use the Lanczos method).
  3. Obtain  $I^{right}[l' + 1]$  from  $I^{right}[l']$  and store it. In order to perform this task, we use  $|\psi\rangle$  to build the reduced density matrix  $\tilde{\rho}$  of the right block. Obtain the eigenvectors of  $\tilde{\rho}$  which stand for the new vectors  $|R\rangle_{l'+1}$ . Then, we use the recursive relation (3.39) and  $\hat{H}_R^{(l')}$  (store it in  $I^{right}[l']$ ) to obtain  $H_R^{(l')}$ . Use (3.38) to get  $\hat{H}_R^{(l'+1)}$ . (Note that we do not use a similar procedure to obtain  $I^{left}[l - 1]$  from  $I^{left}[l]$  because we cannot renormalize to a smaller block. Instead, we use all the  $I^{left}$ 's stored in the previous DMRG step in order to carry out the step 2).
  4. Delete  $I^{left}[l]$  (for this object, it is not necessary anymore to allocate memory on the computer).
  5. Increase by one site the right block ( $l'$  is replaced by  $l' + 1$ ) and decrease by one site the left block ( $l$  is replaced by  $l - 1$ ) and repeat everything from step 2 to step 5 until the left block size is  $l = 1$  and the right block size is  $l' = L - 3$ .

When this part is finished, every  $I^{right}[l']$  with  $l' = 1, \dots, L - 3$  has been stored and all they will be needed for the next sweep.

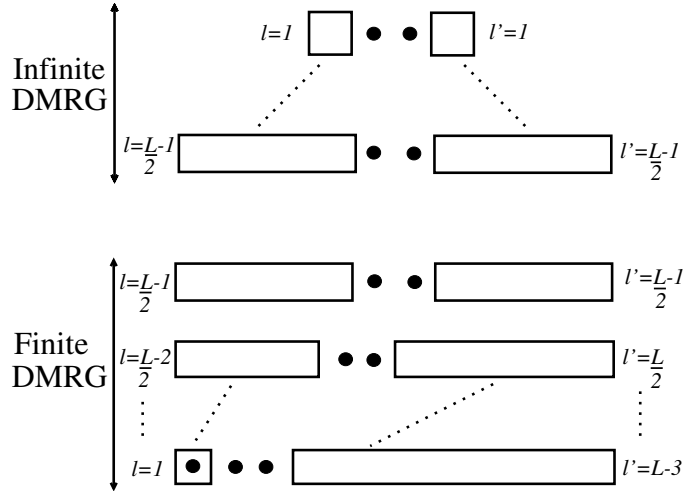


Figure 3.11: The right-left sweep immediately after the infinite algorithm.

- The left-right sweep:

1. At this point,  $l = 1$  and  $l' = L - 3$  (see Fig. 3.12). Use  $I^{left}[l]$ ,  $I^{right}[l']$  and the superblock indices relation  $(\alpha, \beta, \lambda, \gamma) \leftrightarrow p$  to obtain the superblock Hamiltonian (3.20). By diagonalizing  $H$ , get the ground state  $|\psi\rangle$  and its energy  $E_0$ .
2. Obtain  $I^{left}[l+1]$  from  $I^{left}[l]$  and store it. In order to perform this, we use  $|\psi\rangle$  to build the reduced density matrix  $\tilde{\rho}$  of the left block. Obtain the eigenvectors of  $\tilde{\rho}$  which stand for the new vectors  $|F\rangle_{l+1}$ . Then, we use the recursive relation (3.33) to obtain  $H_F^{(l)}$  and (3.32) to get  $\hat{H}_F^{(l+1)}$ .
3. Delete  $I^{right}[l']$ .
4. Increase by one site the left block ( $l$  is replaced by  $l+1$ ) and decrease by one site the right block ( $l'$  is replaced by  $l'-1$ ) and repeat everything from step 1 to step 4 until the right block size is  $l = 1$  and the left block size is  $l' = L - 3$ .

When this part is finished, every  $I^{left}[l]$  with  $l = 1, \dots, L - 3$  have been stored. All the left block informations will be needed for the next sweep.

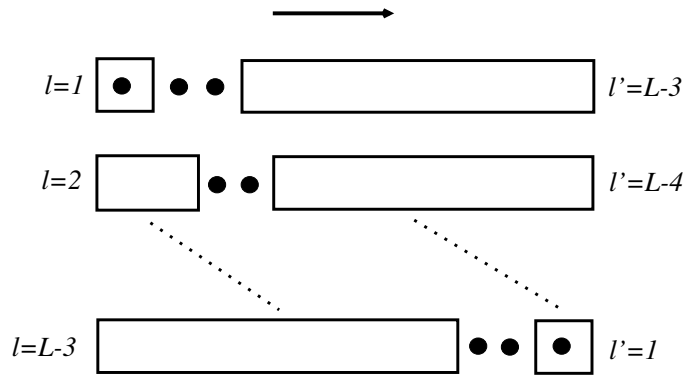


Figure 3.12: The left-right sweep.

- The right-left sweep (Fig. 3.13):
  1. At this point,  $l' = 1$  and  $l = L - 3$ . Use  $I^{right}[l']$  and  $I^{left}[l]$  and the superblock indices relation  $(\alpha, \beta, \lambda, \gamma) \leftrightarrow p$  to obtain the superblock Hamiltonian (3.20). By diagonalizing  $H$ , get the ground state  $|\psi\rangle$  and its energy  $E_0$ .
  2. Obtain  $I^{right}[l' + 1]$  from  $I^{right}[l']$  and store it.
  3. Delete  $I^{left}[l]$ .
  4. Increase by one site the right block ( $l'$  is replaced by  $l' + 1$ ) and decrease by one site the left block ( $l$  is replaced by  $l - 1$ ) and repeat everything from step 1 to step 4 until the left block size is  $l = 1$  and the right block size is  $l' = L - 3$ .

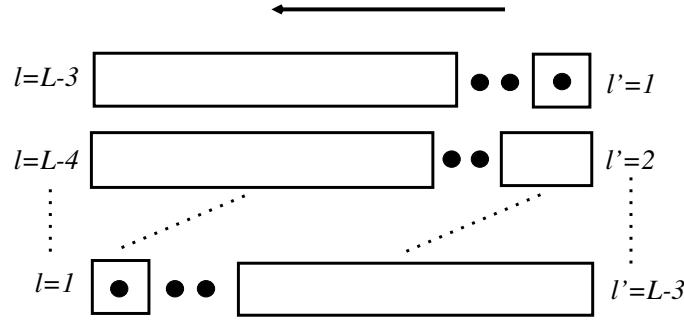


Figure 3.13: The right-left sweep.

Now we repeat everything starting from the left-right sweep until the energy converges. This variational feature of the conventional DMRG can be understood in terms of matrix product states (MPS) [51]. We define one DMRG sweep as a one right-left sweep plus one left-right sweep, i.e. the system is completely swept, firstly in one direction and then in the opposite one. In Fig. 3.14 we show the relative error  $\Delta e$  of the ground-state energy  $E_0$  as function of the number of sweeps and for different values of  $m$  for free spinless fermions (Fig. 3.14(a)) and for the  $t$ - $J$  model (Fig. 3.14(b)). We define  $\Delta e$  as

$$\Delta e = \frac{|E_0 - E_0^{exact}|}{|E_0^{exact}|}, \quad (3.52)$$

where  $E_0^{exact}$  is the exact ground-state energy in the case of free-spinless fermions and for the  $t$ - $J$  model it corresponds to a very large  $m = 1000$  at the last sweep where we can assume that this energy is very close to the exact value. The sweep number 0 denotes the ending point of the infinite DMRG and the starting point of the finite DMRG. Sweep number 1 means that the first sweep (forth and back) was terminated and then the second sweep can start. Note that convergence is already reached at the second sweep. In the case of free-spinless fermions we observe extremely precise results for already  $m = 100$ . In the  $t$ - $J$  model the relative error is of the order of  $10^{-5}$ , for  $m = 200$ . Therefore using  $m = 200$  and four sweeps will be enough for most of our static simulations.

The finite DMRG also allows one to perform measurements of observables and correlation functions and it is also the platform where the time-dependent DMRG is based on as we will see in the following sections.

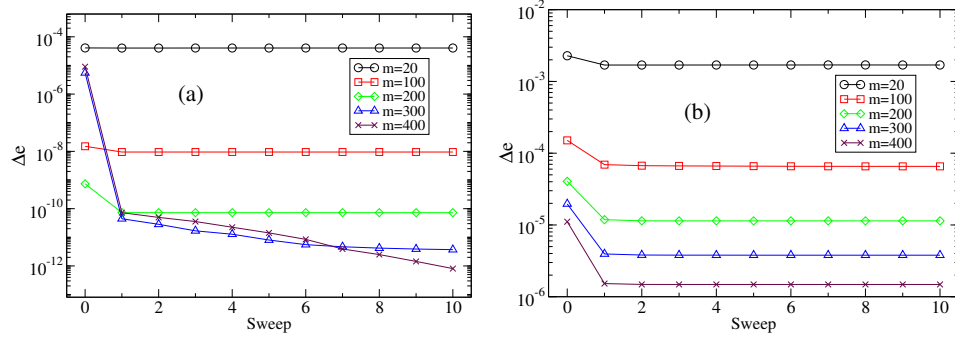


Figure 3.14: Relative error  $\Delta e$  given by Eq. (3.52) as function of the sweep and for different values of  $m$  for density  $n = N/L = 0.5$  and  $L = 200$  sites for: a) free-spinless fermions, b) the  $t$ - $J$  model with  $J = 2t$ .

### 3.1.5 Measurements and correlation functions

Once we are sure that the system has converged into its ground state by sweeping back and forth, we continue this sweeping in order to perform measurements.

Let us start remembering that the ground state for a certain DMRG step is given by

$$|\psi\rangle = \sum_{\alpha\beta\lambda\gamma} \psi_{\alpha\beta\lambda\gamma} |F_\alpha\rangle |S_\beta\rangle |S_\lambda\rangle |R_\gamma\rangle. \quad (3.53)$$

Using this structure, then the mean values  $\langle\psi|O|\psi\rangle$  of an operator  $O$  can be calculated via

$$\langle O \rangle \equiv \langle\psi|O|\psi\rangle = \sum_{\alpha'\beta'\lambda'\gamma'} \sum_{\alpha\beta\lambda\gamma} \psi_{\alpha'\beta'\lambda'\gamma'}^* \psi_{\alpha\beta\lambda\gamma} \langle F_{\alpha'} | \langle S_{\beta'} | \langle S_{\lambda'} | \langle R_{\gamma'} | O | F_\alpha \rangle | S_\beta \rangle | S_\lambda \rangle | R_\gamma \rangle. \quad (3.54)$$

In the case of one-point correlation functions, i.e. when  $O = O_i$  is a local operator acting only on one site, let us say the middle site  $|S_\beta\rangle$ , then it is easy to prove that

$$\langle\psi|O_i|\psi\rangle = \sum_{\beta'} \sum_{\beta} \psi_{\alpha\beta'\lambda\gamma}^* \psi_{\alpha\beta\lambda\gamma} \langle S_{\beta'} | O_i | S_\beta \rangle, \quad (3.55)$$

where the matrix  $\langle S_{\beta'} | O_i | S_\beta \rangle$  is constant during the whole DMRG because the one-site basis  $\{|S_\beta\rangle\}$  does not change. For example, for free-spinless fermions, where  $\{|S_\beta\rangle\} = \{|0\rangle, |1\rangle\}$  with  $|0\rangle, |1\rangle$  denoting a non-occupied and occupied site, respectively, the number operator  $n_i$ , counting the number of particles in the site  $i$ , is represented by the matrix

$$n_i = \begin{pmatrix} 0 & 0 \\ 0 & 1 \end{pmatrix}. \quad (3.56)$$

Therefore, while sweeping the system via the finite algorithm, we can make use of Eq. (3.55) to compute  $\langle\psi|O_i|\psi\rangle$  for the lattice sites  $i = 2, \dots, L-2$ . Similar formulas as Eq. (3.55) can be derived for the rest of the lattice sites,  $i = 1, L-1, L$ . For the site  $i = 1$ , we use the first DMRG step of a left-right sweep where the left block has only one site allowing us to write the matrix representation of  $O_1$ . Similarly, we wait until the right block has only one site in order to compute  $O_{L-1}$  and  $O_L$ . In this way we can obtain  $\langle O_i \rangle$  for all lattice sites and therefore important physical quantities like, e.g. particle and spin densities can be obtained.

In the case of two-point correlation functions where  $O = O_i O_j$  and assuming that  $i$  corresponds to the middle site  $|S_\lambda\rangle$  and that  $j$  corresponds to right block  $|R_\gamma\rangle$ , it is straightforward to prove that

$$\langle\psi|O_i O_j|\psi\rangle = \sum_{\lambda'\gamma'} \sum_{\lambda\gamma} \psi_{\alpha\beta\lambda'\gamma'}^* \psi_{\alpha\beta\lambda\gamma} \langle S_{\lambda'}|O_i|S_\lambda\rangle \langle R_{\gamma'}|O_j|R_\gamma\rangle. \quad (3.57)$$

Similar to the previous case, the matrix  $\langle S_{\lambda'}|O_i|S_\lambda\rangle$  is constant in contrast to  $\langle R_{\gamma'}|O_j|R_\gamma\rangle$  that does depend on the DMRG step. This last matrix can be found recursively (similarly to the recursive procedure explained in Sec. 3.1.2 for the Hamiltonian) starting up from a DMRG step where the site  $j$  is not inside the block but it is one of the middle sites. Hence we have illustrated in this section the basic ideas of how to measure correlation functions. This procedure was used to compute the correlation functions in Ch. 4 which help us to determine the ground-state phase diagram of the one-dimensional  $t$ - $J$  model

## 3.2 Time-dependent DMRG

In this section we present the basic concepts of how the finite DMRG algorithm can be extended in order to carry out the time evolution. We focus here on the so called adaptive t-DMRG [26, 52] which is the most efficient version for performing the time evolution of systems with nearest neighbor interactions. The word ‘‘adaptive’’ refers to the fact that at every time step the Hilbert space is adapted to be the best representation of the evolved state at that time, making this method extremely efficient. In order to do the time evolution of a quantum system we have to carry out the following operation

$$|\psi(\tau + \Delta\tau)\rangle = \exp(-iH\Delta\tau)|\psi(\tau)\rangle, \quad (3.58)$$

this means that the state of the system at time  $\tau + \Delta\tau$  is obtained by applying the evolution operator  $\exp(-iH\Delta\tau)$  on the state at time  $\tau$ . We have assumed that the Hamiltonian  $H$  is time-independent. In order to accomplish this goal we start dividing the lattice into odd and even bonds as is shown in Fig. 3.15

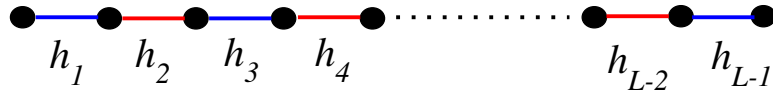


Figure 3.15: We divide the lattice into odd (blue) and even (red) bonds.

Since we are considering only nearest neighbor interactions, the Hamiltonian can be written as

$$H = H_1 + H_2, \quad (3.59)$$

where

$$H_1 = \sum_{i=1}^{L/2} h_{2i-1} \quad \text{and} \quad H_2 = \sum_{i=1}^{L/2-1} h_{2i}, \quad (3.60)$$

$H_1$  corresponding to the odd-bond operators  $h_{2i-1}$  and  $H_2$  to the even-bond operators  $h_{2i}$ . Since  $H_1$  and  $H_2$  share sites, they do not commute, i.e.  $[H_1, H_2] \neq 0$ . We know that  $\exp(A + B) =$

$\exp(A)\exp(B)$  only if  $[A, B] = 0$ . However we can use the Suzuki-Trotter decomposition to approximate the evolution operator as

$$\exp(-iH\Delta\tau) = \exp(-iH_1\Delta\tau)\exp(-iH_2\Delta\tau) + O(\Delta\tau^2). \quad (3.61)$$

Although we have to pay with an error of the order of  $\sim \Delta\tau^2$ , the factors  $\exp(-iH_1\Delta\tau)$  and  $\exp(-iH_2\Delta\tau)$  can be computed exactly as follows

$$\exp(-iH_1\Delta\tau) = \exp(-ih_1\Delta\tau)\exp(-ih_3\Delta\tau)\cdots\exp(-ih_{L-1}\Delta\tau), \quad (3.62)$$

$$\exp(-iH_2\Delta\tau) = \exp(-ih_2\Delta\tau)\exp(-ih_4\Delta\tau)\cdots\exp(-ih_{L-2}\Delta\tau), \quad (3.63)$$

because the odd bonds commute among themselves,  $[h_{2i-1}, h_{2i-1}] = 0$ , and the same for the even bonds,  $[h_{2i}, h_{2i}] = 0$ . This commutations relations are due to the fact that bonds with the same parity do not share sites (see Fig. 3.15).

This decomposition of the evolution operator can be implemented into the finite DMRG. Basically what we have to do is to sweep the system in one direction to operate on all even bonds using Eq. (3.63) and obtain  $\exp(-iH_2\Delta\tau)|\psi(\tau)\rangle$ , and then by sweeping in the opposite direction we operate on all odd bonds using Eq. (3.62) to finally obtain  $|\psi(\tau+\Delta\tau)\rangle \approx \exp(-iH_1\Delta\tau)\exp(-iH_2\Delta\tau)|\psi(\tau)\rangle$ . In order to carry out the basic operation,  $\exp(-ih_i\Delta\tau)$ , in Eqs. (3.62) and (3.63) we use the two middle sites. Then we repeat the same procedure again and again until we have reached the desired time. In principle we could do this just by keeping the superblock basis that we have obtained after the finite DMRG convergence and that is optimal for the initial state. However, after some time this basis will no longer be able to represent the evolved state giving rise to strong errors. The most efficient way to overcome this problem is to adapt the basis to the evolved states, in other words, during each DMRG step we use the resulting state of operating with  $\exp(-ih_i\Delta\tau)$  as target state for computing the density matrix and thus the new superblock basis will be dynamically adapted. The basic operation to be carried out is of the form  $A_i|\phi\rangle$ , where in our particular case  $A_i = \exp(-ih_i\Delta\tau)$ . We assume that  $A_i$  is an operator acting only on the two middle sites. Both states  $|\phi\rangle$  and  $A_i|\phi\rangle$  can be written in the superblock basis as

$$|\phi\rangle = \sum_{\alpha\beta\lambda\gamma} \phi_{\alpha\beta\lambda\gamma} |F_\alpha\rangle |S_\beta\rangle |S_\lambda\rangle |R_\gamma\rangle,$$

$$A_i|\phi\rangle = \sum_{\alpha\beta\lambda\gamma} C_{\alpha\beta\lambda\gamma}^i |F_\alpha\rangle |S_\beta\rangle |S_\lambda\rangle |R_\gamma\rangle.$$

It can be easily proved that the coefficients  $C_{\alpha\beta\lambda\gamma}^i$  of the resulting vector  $A_i|\phi\rangle$  can be obtained using the following matrix-vector multiplication

$$C_{\alpha\beta\lambda\gamma}^i = \sum_{\beta',\lambda'} [A_i]_{(\beta'\lambda')(\beta\lambda)} \phi_{\alpha\beta'\lambda'\gamma}, \quad (3.64)$$

where  $[A_i]_{(\beta'\lambda')(\beta\lambda)}$  is the matrix representation of the operator  $A_i$ . This matrix can be easily computed because it lives only in the subspace of two site. In the case of the time evolution, we have to compute all the matrices  $\exp(-ih_i\Delta\tau)$  which have the form  $f(O)$  where  $O = -ih_i\Delta\tau$  and  $f$  is some complex function. This can be done by using the old trick that the diagonal of the operator  $f(O)$  is just the function  $f$  evaluated at the eigenvalues of  $O$ .

With this we have presented all the fundamental concepts needed for the implementation of the real-time evolution into the DMRG. We have illustrated the procedure using the first order Suzuki-Trotter decomposition (3.61). However, in our code we use the second order version,

$$\exp(-iH\Delta\tau) = \exp(-iH_1\Delta\tau/2) \exp(-iH_2\Delta\tau) \exp(-iH_1\Delta\tau/2) + O(\Delta\tau^3)$$

which is more precise. Note that in this case 1.5 sweeps are needed for carrying out the operation  $\exp(-iH\Delta\tau)$  instead of only 1 sweep. However, one order of magnitude in precision is gained.

### 3.2.1 Preparing the initial state for the time evolution

We have many possibilities in order to perform a non-trivial time evolution of the system, i.e. we have to prepare the system in an initial state which is different from one of the eigenvectors of the Hamiltonian  $H$  used for carrying out the time evolution, otherwise no change in the initial state takes place. For example, we can start by using the static DMRG to obtain the ground state of the Hamiltonian  $H$  and then use another Hamiltonian  $H_t$  during the evolution. Another possibility is to use  $H_t = H$  but we change the ground state via the application of some operation before performing the evolution. In this section we will focus on this last situation with an operation of the following form

$$|\phi\rangle = \sum_{i=1}^L O_i |G\rangle, \quad (3.65)$$

where  $O_i$  is some local operator acting on the single site  $i$  and  $|G\rangle$  is the ground state. Note from Eq. (B.1) of appendix B that the creation of a gaussian wavepacket has the same structure as Eq. (3.65). Then we can sweep the system in one direction and use one of the two middle sites to compute each summand of Eq. (3.65). What we actually do during the sweeping at each DMRG step  $l$  is to compute the cumulative vector

$$|\xi_l\rangle = \sum_{i=1}^l O_i |G\rangle.$$

We also have to adapt the basis of all the DMRG blocks to the resulting vector  $|\phi\rangle$ . In principle this could be managed by computing the reduced density matrix using  $|\xi_l\rangle$  as a target state at each DMRG step. However, it could happen that, for example, the first term  $|\xi_1\rangle = 0$  and then considering this as the unique target state would kill the entire simulation. Therefore while computing  $|\xi_l\rangle$  at each DMRG step we include also the ground state  $|G\rangle$  as a target state in the reduced density matrix. In order to include more than one target state we use the following reduced density matrix

$$\rho = \text{Tr}_R(w_1 |\xi_l\rangle \langle \xi_l| + w_2 |G\rangle \langle G|), \quad (3.66)$$

which considered a statistical mixture of the two states  $|\xi_l\rangle$  and  $|G\rangle$ . We choose the statistical weights as  $w_1 = w_2 = 1/2$  (note that  $w_1 + w_2 = 1$ ). Only after the end of the sweep, when  $|\phi\rangle = |\xi_L\rangle$  have been finally obtained, we carry out another complete sweep (back and forth) taking  $|\phi\rangle$  as the only target state in order to optimize the basis of the blocks.

Another point that might be considered while computing  $|\phi\rangle$  is the conservation of the quantum numbers. In the case that the operation (3.65) produces a change in the quantum numbers we have to relax the constraint of considering only one sector in order to take also into account those sectors where  $|\phi\rangle$  belongs to. This is because  $|\phi\rangle$  and  $|G\rangle$ , which belong to different sectors, have to be included in the reduced density matrix as target states while computing  $|\phi\rangle$ . As before, only after  $|\phi\rangle$  has been completely obtained, we can again restrict the DMRG only to the sectors corresponding to  $|\phi\rangle$ . For example, in our particular case of creating a wavepacket (see Eq. B.1), we have that  $O_i$  is proportional to the creation operator  $c_i^\dagger$  and then during its creation we have to keep the sectors

$N$  and  $N + 1$  and only after we have finished and from then on we can restrict the DMRG to the sector  $N + 1$ .

Another important technicality that arises in the case that  $O_i \propto c_i^\dagger$  is the implementation of the fermionic phase (sign factor). In fact, as we will see next, it is not totally true that we can use Eq. (3.65) when  $O_i$  contains a fermionic phase. We will illustrate here the main idea of how this phase can be taken into account for the case of spinless fermions. For spinfull fermions the procedure is similar. Let us assume the following order for creating particles in the Fock space

$$(c_1^\dagger)^{n_1} \dots (c_L^\dagger)^{n_L} |0\rangle, \quad (3.67)$$

where  $n_i = 0, 1$  is the number of fermions on the site  $i$  and  $|0\rangle$  is the vacuum state with no particles. During the creation of the wavepacket we have to perform the operation

$$c_i^\dagger |F_\alpha\rangle |S_\beta\rangle |S_\lambda\rangle |R_\gamma\rangle. \quad (3.68)$$

Since the vectors (3.67) form a basis of the Hilbert space, then the superblock vectors  $|F_\alpha\rangle |S_\beta\rangle |S_\lambda\rangle |R_\gamma\rangle$  can be written as a linear combination of them. Therefore, Eq. (3.68) contains operations of the form

$$c_i^\dagger (c_1^\dagger)^{n_1} \dots (c_L^\dagger)^{n_L} |0\rangle. \quad (3.69)$$

Let us assume that the index  $i$  corresponds to the middle site  $S_\beta$ . Then using the fermionic commutation relations we obtain that

$$c_i^\dagger (c_1^\dagger)^{n_1} \dots (c_L^\dagger)^{n_L} |0\rangle = (-1)^{n_1 + \dots + n_{i-1}} (c_1^\dagger)^{n_1} \dots c_i^\dagger (c_i^\dagger)^{n_i} \dots (c_L^\dagger)^{n_L} |0\rangle. \quad (3.70)$$

Since the sites,  $1, \dots, i - 1$ , belong to the left block, then the sign  $(-1)^{n_1 + \dots + n_{i-1}}$  lives only inside this subspace. Therefore, according to Eq. (3.70), we can write the component of the vector  $c_i^\dagger |G\rangle$  as

$$[c_i^\dagger |G]_{\alpha\beta\lambda\gamma} = \sum_{\alpha'} [Sign^{(i-1)}]_{\alpha\alpha'} \sum_{\beta'} \langle S_\beta | c_i^\dagger | S'_\beta \rangle G_{\alpha'\beta'\lambda\gamma} \quad (3.71)$$

where  $\langle S_\beta | c_i^\dagger | S'_\beta \rangle$  is the matrix representation of  $c_i^\dagger$  in one-single site subspace (then this matrix is independent of  $i$  and does not contain information of the fermionic sign because for one site problem there is no phase factor coming from the exchange of particles) and  $G_{\alpha'\beta'\lambda\gamma}$  are the components of the ground state. The matrix  $[Sign^{(l)}]$  contains all the information about the fermionic sign. After some algebra, similar to that of the recursive relations for the Hamiltonian in Sec. 3.1.2, we find the following recursive relation for the matrix  $[Sign^{(l)}]$

$$[Sign^{(l+1)}]_{\alpha'\alpha} = \sum_k^m \sum_q^m \sum_j^d a_{kj}^{\alpha'} a_{qj}^\alpha [Sign^{(l)}]_{kq} (-1)^{n_j}, \quad (3.72)$$

where the components  $a_{qj}^\alpha$  are given by Eq. (3.29). It is easy to see from Eq. (3.70) that the initial condition for the recursive relation (3.72) is given by the matrix  $[Sign^{(1)}]_{\alpha'\alpha} = (-1)^{n_\alpha} \delta_{\alpha'\alpha}$  where at this point of the DMRG the left block has only one site.

With this we have collected all the essential ingredients for preparing the system in a non-trivial initial state, that in our particular case, consists of a state representing one spin-up electron in form of a gaussian wavepacket.

Before concluding this chapter it is important to estimate the error of the time dependent simulations. There are two sources of error, one coming from the Suzuki-Trotter decomposition and

another coming from the increase of the entanglement entropy with time. In order to make an estimation of the error we can consider the time evolution of conserved quantities like the total energy  $\langle H \rangle$  and the total particle number  $\langle N \rangle$ , which in principle should not change in time  $\tau$ . In Fig. 3.16 we measure the relative errors

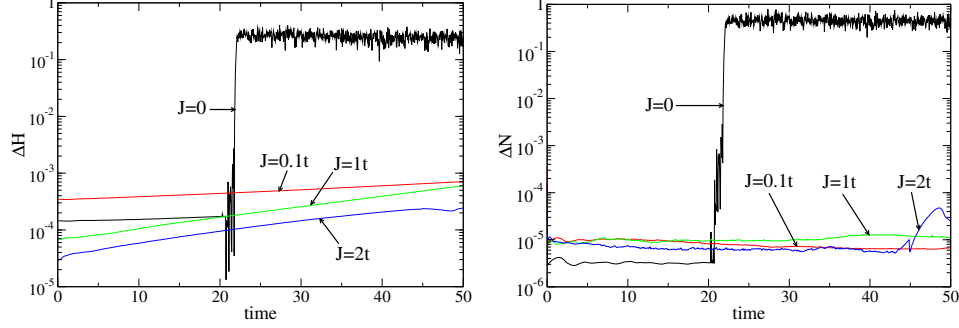


Figure 3.16: Relative deviations  $\Delta H$  and  $\Delta N$  of the energy and particle number, respectively, as function of time for the  $t$ - $J$  model. Time is measure in units of  $1/t$ , where  $t$  is the hopping constant. We observe that for a finite value of  $J$  the error is of the order  $10^{-4}$  which we consider as enough for our numerical simulations.

$$\Delta H = \frac{\langle \psi(\tau) | H | \psi(\tau) \rangle - \langle \psi(0) | H | \psi(0) \rangle}{\langle \psi(0) | H | \psi(0) \rangle} \quad \text{and} \quad \Delta N = \frac{\langle \psi(\tau) | N | \psi(\tau) \rangle - \langle \psi(0) | N | \psi(0) \rangle}{\langle \psi(0) | N | \psi(0) \rangle}, \quad (3.73)$$

for the  $t$ - $J$  model with  $n = 0.6$ ,  $L = 160$  sites,  $\Delta\tau = 0.05$ , and  $m = 450$ .  $|\psi(0)\rangle$  is the initial state after injecting one more electron in form of wavepacket, with momentum  $k = 0.7\pi$  and width  $\Delta x = 5$  lattice sites, into the system. We observe that for  $J = 0$  and at  $\tau \sim 20$  the error increases extremely fast and it fluctuates very strongly for further times. The reason for that is that the

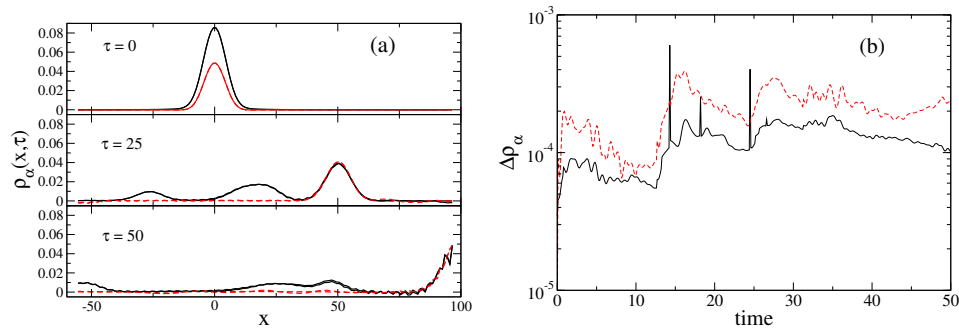


Figure 3.17: Error estimation of the charge (full-black line) and spin (red-dashed line) densities for the  $t$ - $J$  model for  $J = 2.0t$ ,  $n = 0.6$ ,  $k = 0.6\pi$  and  $L = 160$ . (a): charge and spin densities at different times  $\tau$ . There are two full-black lines for the charge (one line for  $m = 450$  and another for  $m = 1000$ ) and similarly two red-dashed lines for the spin. Note that any difference can be barely observed. (b): the error  $\Delta\rho$ , given by Eq. (3.74), is of the order of  $10^{-4}$ .

entanglement entropy increases linearly with time and therefore the number of DMRG vectors  $m$  to describe the system correctly increases exponentially with time. This critical time where the error

explodes is also called runaway time [52]. However for a finite value of  $J$  we observe that the error is of the order  $10^{-4}$  which we consider as enough for our numerical simulations up to  $\tau = 50$ . The case  $J = 0$  is very sensitive because it corresponds to a highly degenerate system and there the entanglement entropy is larger than for the case of a finite  $J$ . It is also important to estimate the error of the charge and spin densities relative to the ground state (see Eq. (5.28)), we assume that the densities for  $m = 1000$  are close to the exact value and then we compare to the densities for  $m = 450$ . In Fig. 3.17(a) we observe no significant difference between the densities for  $m = 450$  and for  $m = 1000$ . In order to be more quantitative we compute the deviation

$$\Delta\rho_\alpha = \frac{1}{L} \sqrt{\sum_i [\rho_\alpha^{m_1}(x_i) - \rho_\alpha^{m_2}(x_i)]^2}, \quad (3.74)$$

where  $\rho_\alpha^{m_1}$  stands for the density for  $m = 1000$  and  $\rho_\alpha^{m_2}$  corresponds to  $m = 450$ . The subindex  $\alpha = c, s$  denotes the charge and the spin density, respectively. In Fig. 3.17(b) we observe that this deviation is of the order of  $10^{-4}$  which is a good indication of convergence to the exact value.

## Chapter 4

# Ground-State Phase Diagram

The main goal of this chapter is to present a precise determination of the phase diagram of the 1D  $t$ - $J$  model, described by the following Hamiltonian,

$$H = -t \sum_{i,\sigma}^{L-1} \left( \tilde{c}_{i,\sigma}^\dagger \tilde{c}_{i+1,\sigma} + \text{h.c.} \right) + J \sum_i^{L-1} \left( \vec{S}_i \cdot \vec{S}_{i+1} - \frac{1}{4} n_i n_{i+1} \right), \quad (4.1)$$

where the operator  $\tilde{c}_{i,\sigma}^\dagger$  ( $\tilde{c}_{i,\sigma}$ ) creates (destroys) a fermion with spin  $\sigma = \uparrow, \downarrow$  on the site  $i$ . They are not canonical fermionic operators since they act on a restricted Hilbert space without double occupancy.  $\vec{S}_i = (S_i^x, S_i^y, S_i^z) = \tilde{c}_{i,\alpha}^\dagger \vec{\sigma}_{\alpha\beta} \tilde{c}_{i,\beta}$  is the spin operator, where  $\vec{\sigma} = (\sigma_x, \sigma_y, \sigma_z)$  are the Pauli matrices.  $n_i = \tilde{c}_{i,\sigma}^\dagger \tilde{c}_{i,\sigma}$  is the density operator and  $L$  is the number of lattice sites. The first term represents the kinetic energy of electrons hopping between nearest-neighbor sites which is controlled by the constant  $t$ . The second term corresponds to exchange processes favoring the formation of singlet-electron pairs in nearest-neighbor sites and it is controlled by the constant  $J$ .

The results are obtained using the DMRG method [12, 13, 42], explained in Ch. 3, on lattices with up to  $L = 200$  sites, by performing finite-size extrapolations to the thermodynamic limit for the correlation functions and energy differences relevant for the different phases [33]. We have to choose values of  $n$  and  $L$  such that the total particle number  $N = nL$  is an integer number. In most of the results we extrapolate to the thermodynamic limit using system sizes  $L = 40, 80, 120, 160$ , and  $200$ . These values of  $L$  allow us a discretization in density of  $\Delta n = 0.05$  which is consistent with  $N$  being an even integer, and hence, the ground state corresponds to  $S_{tot}^z = \sum S_i^z = 0$ . All the results were obtained using at least 200 DMRG vectors, 4 sweeps, and a discarded weight of  $10^{-8}$ . This translates into errors in energy of the order of  $10^{-5}$  and in correlation functions of the order of  $10^{-4}$  at the largest distances.

The phase diagram for the 1D  $t$ - $J$  model obtained by Ogata et al. [32] is based on exact diagonalization (ED) on systems with up to 16 lattice sites. They found three phases: a repulsive LL phase (metal), an attractive LL phase (superconductor) and phase-separation. At that time they suspected the existence of a spin gap at low density but they could not prove its existence due to the limitation to small system sizes. Posterior works [27, 28] found evidences of the spin gap using variational methods. However, Nakamura *et al.* [29] found based on an RG analysis that the spin-gap region is larger than expected. Here we present results from a direct measurement of the spin gap and an extrapolation to the thermodynamic limit. Details for it will be discussed in Sec. 4.2.

Our results can be summarized in the phase diagram shown in Fig. 4.1. We obtained four phases: a metallic phase (M) or repulsive LL, a gapless superconducting (SC) region, a singlet-superconducting phase with spin gap (SG + SS), and phase-separation (PS), where the system separates into a

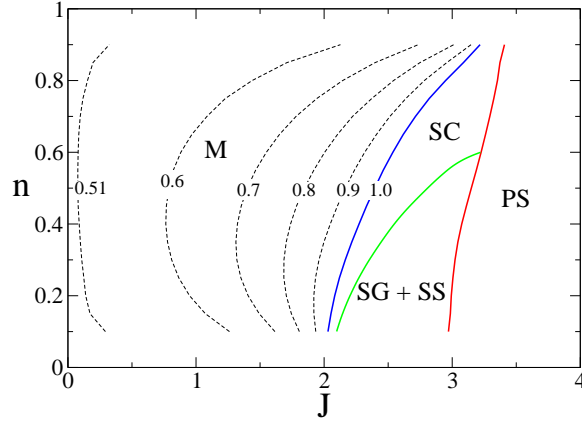


Figure 4.1: Phase diagram of the 1D  $t$ - $J$  model from DMRG for densities  $0.1 \leq n \leq 0.9$  and in the range  $0 < J \leq 4$ , where we set  $t = 1$ .  $n = N/L$  is the electronic density ( $N$  is the total number of particles and  $L$  the number of lattice sites). Four phases are present: a metallic phase (M) or repulsive Luttinger liquid, a gapless superconducting (SC) phase, a singlet-superconducting phase with spin gap (SG + SS), and phase-separation (PS). The number given to each line stands for the value of the Luttinger parameter  $K_\rho$ .

hole-rich and an electron-rich part. The number given to each line stands for the value of the Luttinger parameter  $K_\rho$ , with  $K_\rho < 1.0$  in M and  $K_\rho > 1.0$  in both superconducting phases. The determination of  $K_\rho$  will be discussed in Sec. 4.1.

In order to characterize the phases and to find the boundaries between them, we computed directly the energy gap to triplet excitations and measure the density-density correlation function,

$$N_{ij} = \langle n_i n_j \rangle - \langle n_i \rangle \langle n_j \rangle, \quad (4.2)$$

the spin-spin correlation function,

$$S_{ij} = \langle S_i^z S_j^z \rangle, \quad (4.3)$$

the pairing correlation function

$$P_{ij} = \langle \Delta_i^\dagger \Delta_j \rangle, \quad (4.4)$$

where

$$\Delta_i^\dagger = \frac{1}{\sqrt{2}} (\tilde{c}_{i,\downarrow}^\dagger \tilde{c}_{i+1,\uparrow}^\dagger - \tilde{c}_{i,\uparrow}^\dagger \tilde{c}_{i+1,\downarrow}^\dagger) \quad (4.5)$$

for singlet pairing, and

$$\Delta_i^\dagger = \tilde{c}_{i,\uparrow}^\dagger \tilde{c}_{i+1,\uparrow}^\dagger \quad (4.6)$$

for triplet pairing. Finally, we also considered the complex conjugate of the equal-time one-particle Green's function,

$$G_{ij}^\dagger = \langle \tilde{c}_j^\dagger \tilde{c}_i \rangle, \quad (4.7)$$

that will be needed for computing the momentum distribution function. The corresponding structure factors are obtained by Fourier transformation,

$$X(k) = \frac{1}{L} \sum_{i,j=1}^L e^{ik(x_i - x_j)} X_{ij}, \quad (4.8)$$

Although the systems considered lack translational invariance due to open boundary conditions, for the large system sizes considered here, we could not observe any artifact introduced by this procedure.

## 4.1 Metallic phase

In order to characterize this phase, we compute the Luttinger parameter  $K_\rho$ , with  $K_\rho < 1$  ( $K_\rho > 1$ ) for a repulsive (attractive) interaction, and  $K_\rho = 1$  corresponds to the case which reproduces the same critical exponents as in the free case (see the discussion on page 20 concerning Eq. (2.11).) In order to obtain  $K_\rho$ , we consider the structure factor for the density correlations which displays a linear behavior with a slope proportional to  $K_\rho$  in the limit  $k \rightarrow 0$  [3, 53, 54],

$$N(k) \rightarrow K_\rho |k| a / \pi \text{ for } k \rightarrow 0, \quad (4.9)$$

that results from Fourier transforming the first term in Eq. (4.12) below. Here  $a$  is the lattice constant (we set  $a = 1$ ). Figure 4.2 shows  $N(k)$  for  $n = 0.5$ ,  $J = 2.0$  and  $L = 40, 80, 120, 160$ , and

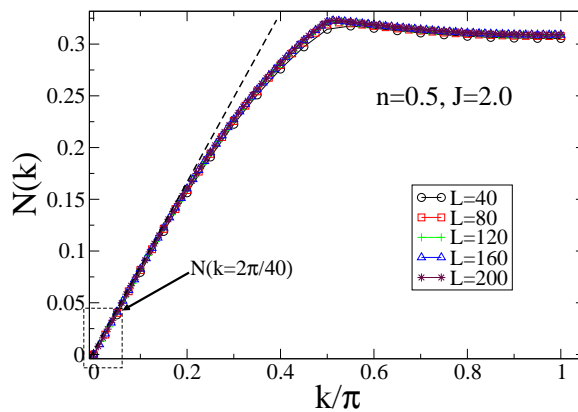


Figure 4.2: Structure factor  $N(k)$  of the density-density correlation function for  $n = 0.5$ ,  $J = 2.0$  and  $L = 40, 80, 120, 160$ , and  $200$ .

200. We observe a clear linear behavior for small  $k$ , with  $N(k = 0) = 0$  due to the conservation of the total particle number.

Although  $N(k)$  appears to be almost independent of the lattice size, a more precise value of the slope is obtained by extrapolating the value of  $N(k)$  at the point  $k = 2\pi/40$ , that is the smallest wavevector in our smallest system, to  $L \rightarrow \infty$ . Using this last value and  $N(k = 0) = 0$  we obtain the slope and then we can extract  $K_\rho$  in the thermodynamic limit using Eq. (4.9). This extrapolation is shown in Fig. 4.3.

We repeated this procedure for different values of  $n$  and  $J$ .  $K_\rho$  as function of  $J$  for different densities  $n$  is plotted in Fig. 4.4. Note that  $K_\rho \rightarrow 0.5$  when  $J \rightarrow 0$  for all densities, which is in agreement with the results obtained for the  $U/t \rightarrow \infty$  Hubbard model [55]. It can also be observed that, for  $K_\rho > 1$ ,  $K_\rho$  increases quite fast with the interaction constant  $J$  and it actually should diverge in the phase-separated region.

The critical exponents  $K_\rho$  at the supersymmetric point  $J = 2$  and for all densities were exactly obtained by means of the Bethe-Ansatz [56]. In Fig. 4.5 we compare our DMRG results with this exact solution, and observe a very good agreement between both. The deviations at very low (very high) densities point to the necessity of having larger systems for such very dilute cases, with a rather small number of particles (holes) to be able to properly describe a phase. They lead however, to barely noticeable shifts in the phase diagram.

From the data set presented in Fig. 4.4 we can extract all the points which fulfill  $K_\rho(n, J) = \text{const.}$  These are curves which separate regions with different Luttinger parameters. The different regions and curves are plotted in Fig. 4.6. The red (dashed) line ( $K_\rho(n, J) = 1$ ) denotes the boundary

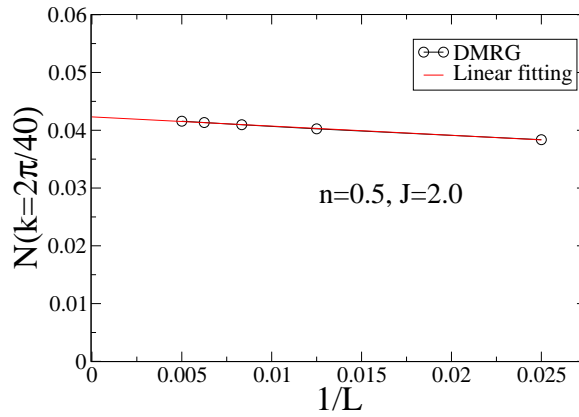


Figure 4.3: Extrapolation to the thermodynamic limit of  $N(k = 2\pi/40)$  for  $n = 0.5$  and  $J = 2.0$ .

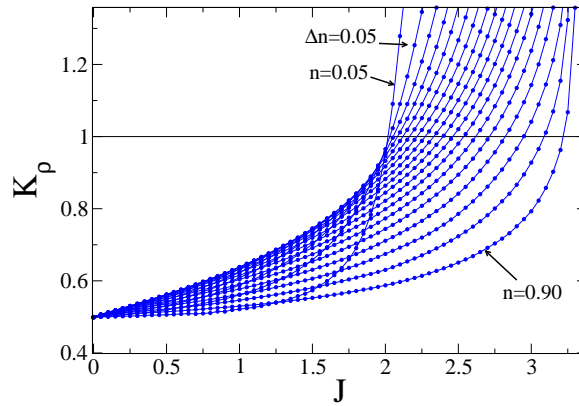


Figure 4.4:  $K_\rho$  as function of  $J$  for different densities  $n$ .

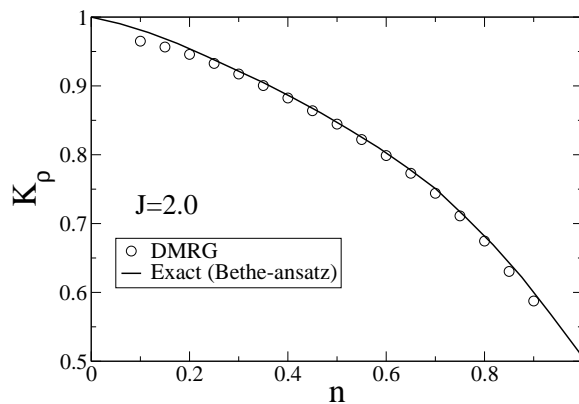


Figure 4.5:  $K_\rho$  as function of the density  $n$  for  $J = 2$  (supersymmetric point).

between the metallic phase and the superconducting phases. This line and few others were also plotted in the phase diagram (Fig. 4.1). Note that the density of lines increases with  $J$  showing the fast growth of  $K_\rho$ .

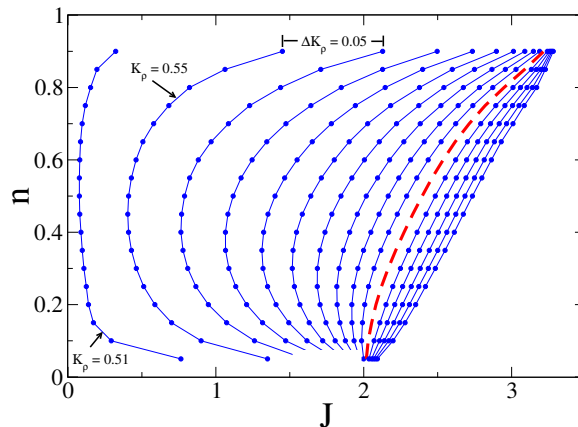


Figure 4.6: Regions with different Luttinger parameters  $K_\rho(n, J)$ . Each curve corresponds to a constant value of  $K_\rho$ . The red (dashed) line ( $K_\rho(n, J) = 1$ ) denotes the boundary between the metallic phase and the superconducting phases. Note that the density of lines increases with  $J$  showing the fast growth of  $K_\rho$ .

## 4.2 Singlet-superconductivity and spin-gap phase

The possibility of a region with a spin gap was first analyzed by Ogata *et al.* [32] for the low density limit, where a gas of singlet bound pairs may form. They compared the ground-state energy of a system containing four particles to twice the energy of a system with only two particles. The energy for the last situation is  $2(-J - 4/J)$ , where the expression  $-J - 4/J$  is obtained by solving exactly the Hamiltonian (1.1) for two particles. We compare here the ground-state energy per particle for 4, 6, and 8 particles obtained numerically with DMRG to that of a gas of bound pairs (Fig. 4.7), using 1000 lattice sites. We observe a region,  $2.0 < J < 3.0$ , where energies are the same within an error of  $10^{-5}$ . At least from energy considerations, this is an indication of the possibility of the formation of a gas of singlet bound pairs and consequently of the existence of a spin gap at very low densities. Moreover, no evidence for the formation of more complex entities can be seen.

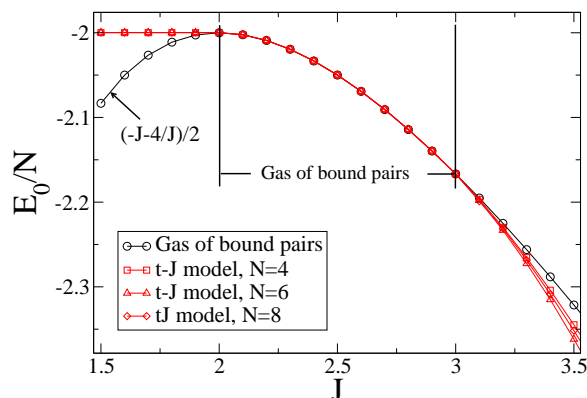


Figure 4.7: Energy comparison between systems containing four, six and eight particles and a gas of singlet bound pairs. We observe a region  $2.0 < J < 3.0$  where all energies are the same within an error of  $10^{-5}$ . This opens the possibility of the formation of a gas of singlet bound pairs and consequently of the existence of a spin gap at very low densities.

A more precise estimate can be obtained by measuring directly the spin gap  $\Delta E_S$ . The spin

excitation energy from a singlet to a triplet state is given by the energy difference

$$\Delta E_S = E_0(N, S_{tot}^z = 1) - E_0(N, S_{tot}^z = 0), \quad (4.10)$$

where the subindex 0 means that we take the lowest energy eigenvalue within the sector with given quantum numbers  $N$  and  $S_{tot}^z$ . In order to go to the thermodynamic limit we plot  $\Delta E_S$  as a function of  $1/L$  and we extrapolate to  $1/L \rightarrow 0$  using  $L = 40, 80, 120, 160$ , and  $200$ . Figure 4.8 shows  $\Delta E_S$  vs  $1/L$  at  $n = 0.2$  and for  $J = 2.0, 2.7$  and  $2.9$ . The extrapolations to the thermodynamic limit are performed with third-order polynomials. While for  $J = 2$ , where the system is still in the metallic regime the gap extrapolates to zero, for  $J = 2.7$  and  $2.9$  a finite gap can be clearly seen.

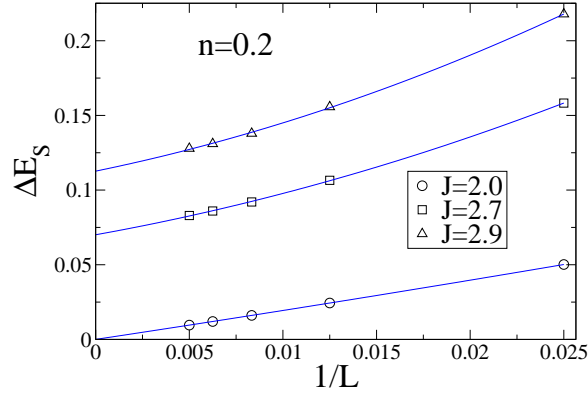


Figure 4.8:  $\Delta E_S$  vs  $1/L$  for  $n = 0.2$  and various values of  $J$ . For  $J = 2$ , where the system is still in the metallic phase, the spin gap extrapolates to zero in the thermodynamic limit.

Proceeding in the same manner for different values of  $n$  and  $J$ , we can obtain the spin gap in the thermodynamic limit (Fig. 4.9). For  $J < 2$  (metallic phase) we observe that the spin gap is zero for all densities. For  $J > 2$  a finite spin gap emerges that increases as the density diminishes. For definiteness,  $J_c$  is defined in our case as the value of  $J$  for which  $\Delta E_S > 10^{-4}t$ , this value being the range on which  $\Delta E_S$  fluctuates around zero before it definitively increases as a function of  $J$  for a given density. In this manner we have obtained the lowest boundary of the spin-gap phase in the phase diagram (Fig. 4.1).

We present also in Fig. 4.10 the spin gap as a function of  $n$  for  $J = 2.1 - 2.8$ . Note that  $\Delta E_S$  smoothly closes to zero when the density is increased.  $\Delta E_S$  attains its largest values as  $J$  increases for the limit of vanishing densities, reaching  $\Delta E_S \approx J/20$ . Since in a one-dimensional quantum system superconductivity cannot set in due to the Mermin-Wagner theorem, such a finite value of the gap gives the energy scale at which pairs form, signaling the existence of preformed pairs in this regime. A further increase of  $J$  leads to phase separation, that we discuss next. A detailed analysis of the transition to phase separation, centering on the possibility of clusters with more than one pair is presented in Sec. 4.4.4.

### 4.3 Phase separation

In this phase the attraction among the particles is so strong that they start to form antiferromagnetic domains, such that the system separates into particle- and hole rich regions. In the limit  $J \rightarrow \infty$  all the particles join in a single island, which can be described by the Heisenberg model forming an electron solid phase, a denomination proposed by Chen and Moukouri [34], where the kinetic

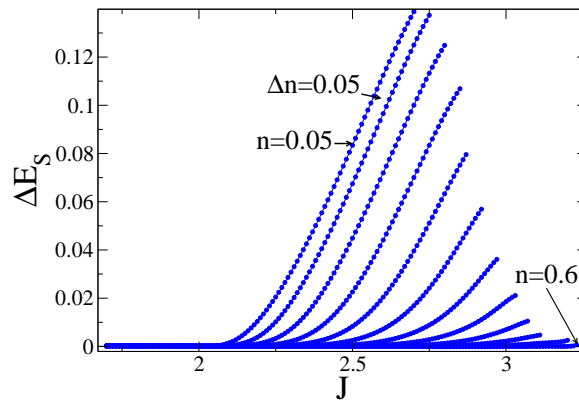


Figure 4.9: Spin gap  $\Delta E_S$  in the thermodynamic limit as a function of  $J$  and for different densities  $n$ . For  $J < 2$  (metallic phase) the spin gap is zero for all densities. For  $J > 2$  a finite spin gap emerges with a value that increases for diminishing densities. We can observe a small but finite spin gap up to  $n = 0.55$ .

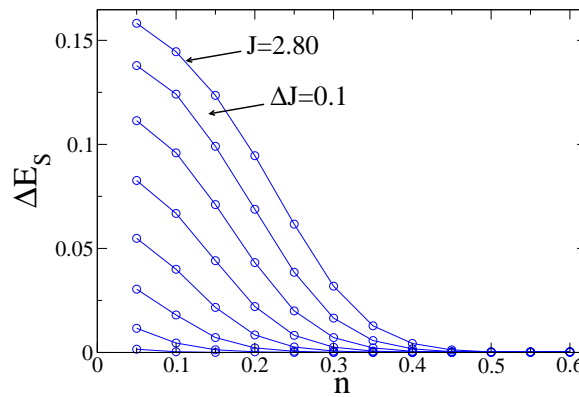


Figure 4.10: Spin gap  $\Delta E_S$  in the thermodynamic limit as a function of  $n$  for  $J = 2.1 - 2.8$ .

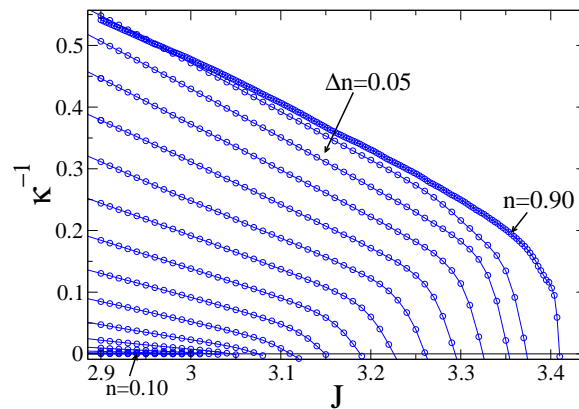


Figure 4.11: Inverse of the compressibility  $\kappa^{-1}$  as a function of  $J$  for  $n = 0.1 - 0.9$  with  $\Delta n = 0.05$ .

fluctuations are strongly quenched and only spin fluctuations remain. We first consider the inverse of the compressibility that vanishes at the onset of phase-separation.

At zero temperature the expression for the inverse compressibility is given by

$$\begin{aligned}\kappa^{-1}(n) &= n^2 \frac{\partial^2 e_0(n)}{\partial n^2} \\ &\approx n^2 \frac{[e(n + \Delta n) + e(n - \Delta n) - 2e(n)]}{\Delta n^2},\end{aligned}\quad (4.11)$$

where  $e_0(n) = E_0/L$  is the energy density per site, and the second line gives the approximation for finite ( $\Delta n = 0.05$ ) changes in the density.

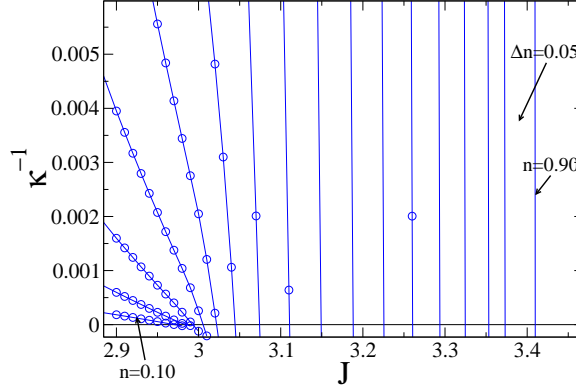


Figure 4.12: Zoom of Fig. 4.11. The points  $(n, J_c)$  where  $\kappa^{-1} = 0$  define the boundary of the phase-separated phase (infinite compressibility).

For the extrapolation of  $e(n)$  we use  $L = 40, 80, 120, 160$  and a third-order polynomial fitting. Figure 4.11 shows  $\kappa^{-1}$  vs  $J$  for different densities. At low densities  $\kappa^{-1}$  is vanishingly small, making the extraction of  $J_c$  very difficult in that region. In order to see more clearly the critical value  $J_c(n)$  where  $\kappa^{-1}$  vanishes, we display a zoom of Fig. 4.11 in Fig. 4.12. In this manner we found the boundary of the phase-separated phase in Fig. 4.1. Note that, in comparison to other studies [27, 28, 32], the phase separation boundary is shifted to higher values of  $J$ .

## 4.4 Correlation functions and density in real space

In order to provide a more detailed characterization of the different phases in the phase diagram determined in the previous section, we consider here the structure factors Eqs. (4.2) - (4.8). We also take into account the analytical results of the correlation functions studied in Ch. 2.4 for the LL and LE cases [3] setting  $K_\sigma = 1$  due to the spin rotational invariance present in the  $t$ - $J$  model.

### 4.4.1 Structure factors

The structure factors obtained by means of the static DMRG are shown in Figs. 4.13-4.16 for  $L = 200$  and for different values of  $n$  and  $J$ .

Figure 4.13 displays the structure factor  $N(k)$  for the density-density correlation function, that for a LL is as follows (see Eq. (2.18)):

$$\begin{aligned}\langle n(r)n(0) \rangle &= \frac{K_\rho}{(\pi r)^2} + A_1 \frac{\cos(2k_F r)}{r^{1+K_\rho}} \ln^{-3/2}(r) \\ &\quad + A_2 \cos(4k_F r) r^{-4K_\rho},\end{aligned}\quad (4.12)$$

where  $A_1$  and  $A_2$  depend in general on the parameters of the model. For each density we have chosen values of  $J$  within one of the phases. For  $J = 1$ , a LL phase is realized for all densities, such that a  $4k_F$  ( $k_F = n\pi/2$ ) anomaly typical for a repulsive LL can be observed. As shown by

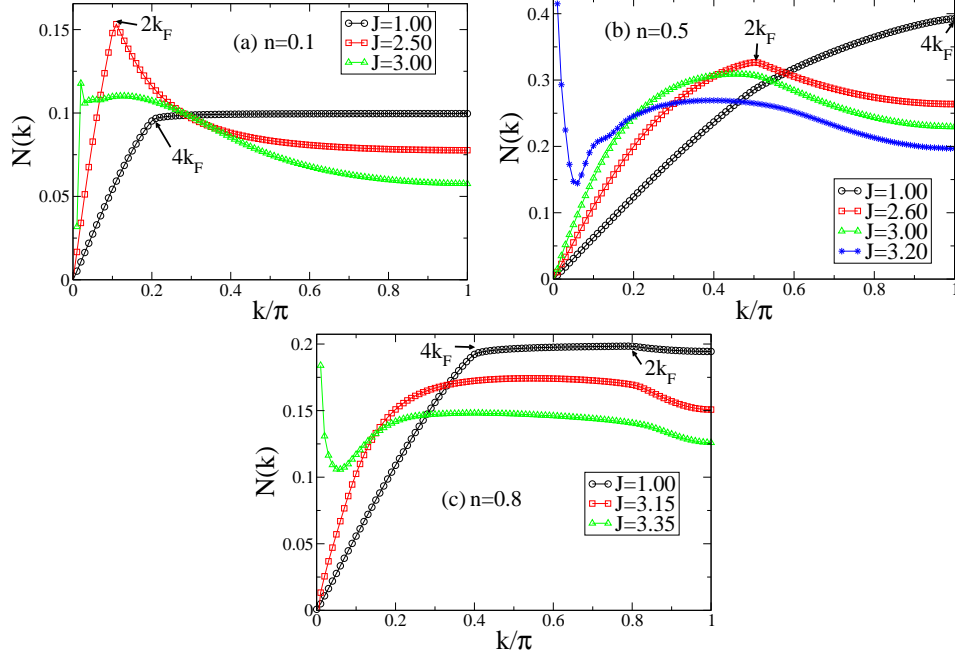


Figure 4.13: Structure factor  $N(k)$  for the density-density correlation function for  $L = 200$  and for different values of  $n$  and  $J$ . The location of  $2k_F$  and  $4k_F$  correspond to the ones resulting from folding them back to the sector  $k > 0$  in the first Brillouin zone.

Eq. (4.12), it is strongest for the smallest values of  $K_\rho$ , that are essentially achieved for all densities for  $J \leq 1$ , as shown by Fig. 4.4. As  $J$  increases, the  $4k_F$  anomaly is suppressed, and a  $2k_F$  cusp is formed, signaling a  $2k_F$  charge density wave due to the tendency towards pairing that is enhanced by  $J$  [3, 57]. However, going closer to the boundary to phase separation (see the curves for  $J = 3$  in Fig. 4.13 (b), and for  $J = 3.15$  in Fig. 4.13 (c)), the singularity is rounded, and increasing  $J$  even more, such that phase-separation is reached, leads to the development of a singularity in  $N(k)$  around  $k = 0$ . That is, the system starts to develop an instability towards long-wavelength charge fluctuations signaling the appearance of phase-separation. However, since in the finite system simulations,  $N(k = 0) = 0$  for all cases due to the conservation of total particle number, such a singularity can only be followed up to the smallest non-vanishing value of momentum for a given system size. Except for the cases, where the system enters the phase separated phase,  $N(k)$  goes continuously to zero, as  $k \rightarrow 0$ , such that  $K_\rho$  can be extracted, as discussed in Sec. 4.1. In both superconducting phases,  $K_\rho > 1$ , as expected, and increases as one goes deeper into the spin-gap phase.

In Fig. 4.14 the structure factor  $S(k)$  for the spin-spin correlation function, is shown. The spin-spin correlation function for a LL is given by (see Eq. (2.21))

$$\langle S^Z(r)S^Z(0) \rangle = \frac{1}{(\pi r)^2} + B_1 \frac{\cos(2k_F r)}{r^{1+K_\rho}} \ln^{1/2}(r). \quad (4.13)$$

The tendency to antiferromagnetism in the  $t$ - $J$  model can be observed at  $J = 1$  for all densities, as revealed by a sharp cusp at  $2k_F$  in  $S(k)$ , corresponding to quasi-long range order in the magnetic

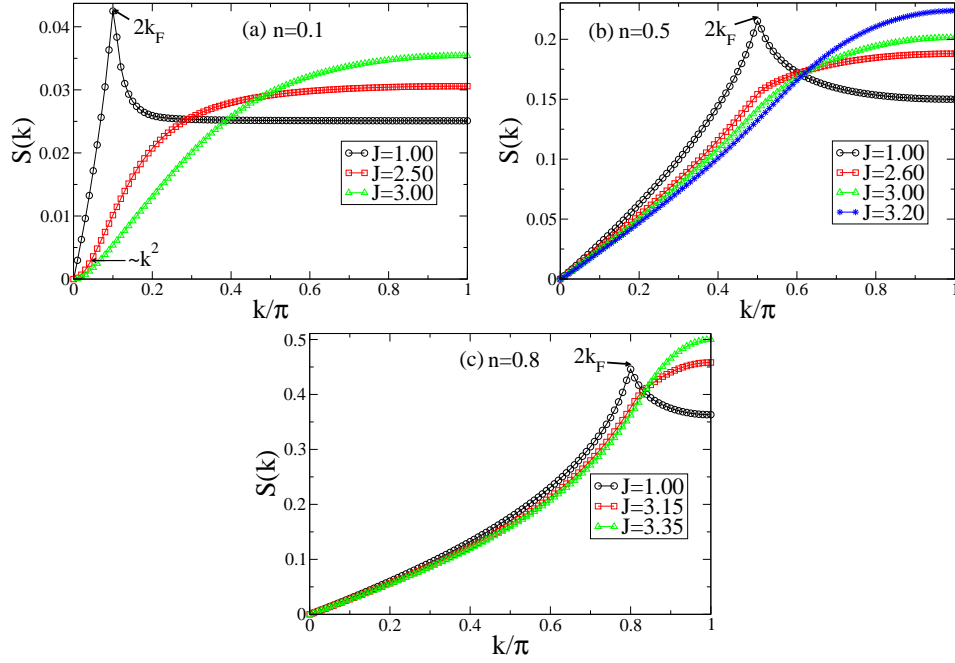


Figure 4.14: Structure factor  $S(k)$  for the spin-spin correlation function for  $L = 200$  and for different values of  $n$  and  $J$ .

channel. However, on increasing  $J$ , such that the system enters the superconducting phase, the sharp peak is suppressed. For densities below  $n = 0.6$ , a spin gap develops, such that on entering this Luther-Emery (LE) phase, the singularity at  $2k_F$  is completely suppressed due to the exponential decay of the spin-spin correlation function [3]. In this case, the corresponding structure factor has a quadratic behavior at small  $k$ 's [27]. This fact can be clearly observed only at  $J = 2.5$  and  $n = 0.1$ , where the spin gap is well developed. As shown in Fig. 4.9, the spin gap at  $J = 3$  for a density  $n = 0.5$  is extremely small ( $\Delta E_S \sim 10^{-3}$ ), such that extremely large systems would be required to show such a behavior. On increasing  $J$  a maximum at  $k = \pi$  develops due to the tendency to form antiferromagnetic islands in the phase-separated region. However, while the charge structure factor already shows clear signals of phase-separation (Fig. 4.13),  $S(k)$  displays only a broad maximum around  $k = \pi$  not yet indicative of antiferromagnetic quasi-long range order. A larger value of  $J$  is necessary in order to achieve such a state, as suggested by the curves corresponding to the largest value of  $J$  in Fig. 4.14. Hence, the onset of phase-separation and the formation of an antiferromagnetic island do not occur simultaneously, as already observed in an earlier quantum Monte Carlo study [57]. We will discuss the formation of antiferromagnetic islands in more detail in Sec. 4.4.4.

In Fig. 4.15 the structure factor  $P_S(k)$  for the singlet-pair-pair correlation function is shown. The corresponding correlation function in the LL sector is given by (Eq. (2.22))

$$\begin{aligned} \langle \Delta_S^\dagger(r) \Delta_S(0) \rangle &= C_0 r^{-(1+1/K_\rho)} \\ &+ C_1 \cos(2k_F r) r^{-(K_\rho+1/K_\rho)}, \end{aligned} \quad (4.14)$$

and in the LE phase by (Eq. (2.29))

$$\begin{aligned} \langle \Delta_S^\dagger(r) \Delta_S(0) \rangle &= C'_0 r^{-1/K_\rho} \\ &+ C'_1 \cos(2k_F r) r^{-(K_\rho+1/K_\rho)}, \end{aligned} \quad (4.15)$$

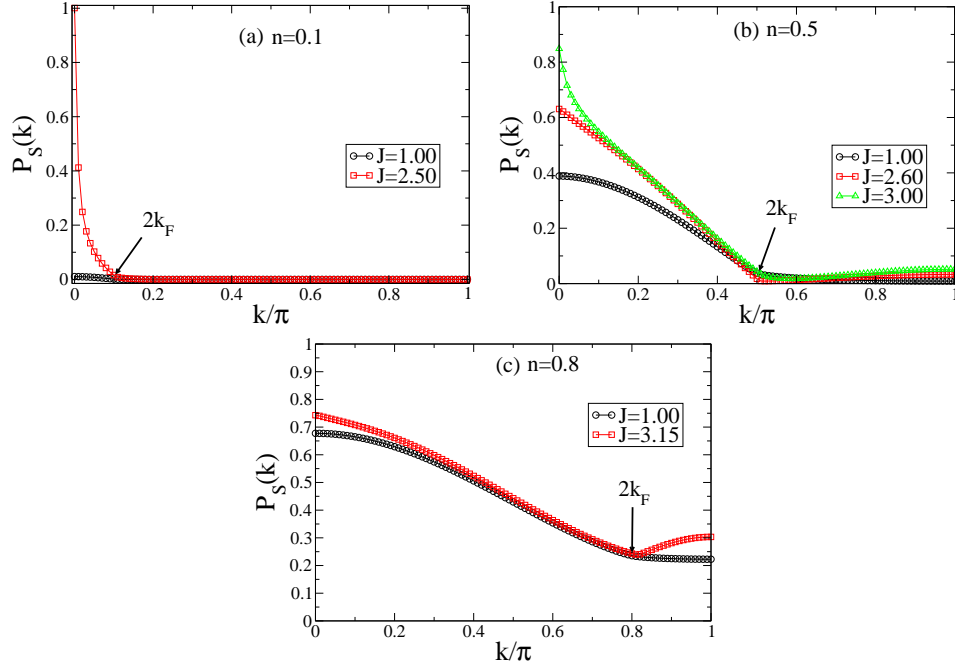


Figure 4.15: Structure factor  $P_S(k)$  for the singlet-pair-pair correlation function for  $L = 200$  and for different values of  $n$  and  $J$ .

where we have ignored logarithmic corrections. Noticing the different powers appearing in Eqs. (4.14) and (4.15), and taking into account that  $K_\rho > 1$  in the superconducting phases, it can be seen that while  $P_S(k)$  does not present a divergence in the LL sector, it will have a diverging contribution at  $k = 0$  in the LE case. Such a behavior can be seen in Fig. 4.15. Within the spin-gap phase (Fig. 4.15 (a),  $J = 2.5$  and Fig. 4.15 (b),  $J = 3$ ), a strong increase is observed for  $k \rightarrow 0$ , indicating the onset of quasi-long range order in this channel. (singlet superconductivity). While increasing  $J$  and  $n$  an enhancement of  $P_S(k = \pi)$  is also produced in the LL phase, the curves display only a rounded maximum in this case. We observe also a  $2k_F$  anomaly in  $P_S(k)$  that correlates with the  $2k_F$  singularities in  $N(k)$ , displayed in Figs. 4.13. We will discuss these correlation functions further in Secs. 4.4.2 and 4.4.3, where they will be confronted with other possible orderings like triplet pairing and charge-density wave (CDW) formation.

In Fig. 4.16 the momentum distribution function  $n(k)$  is shown. In the metallic phase an edge develops in  $n(k)$  that evolves into a singularity in the thermodynamic limit, and hence, defines a Fermi surface, in the way expected for a LL. A weak anomaly at  $3k_F$  can be observed, as revealed by the derivative of  $n(k)$  shown in the insets in Fig. 4.16. As was analytically shown by Ogata and Shiba [11] for the Hubbard model, this singularity in  $n(k)$  is related to the fact that one electron close to  $k_F$  can be excited to a state close to  $3k_F$  together with an electron-hole pair excitation having its momentum near  $-2k_F$ . In Fig. 4.16 the  $3k_F$  anomaly disappears as  $J$  increases, in agreement with previous DMRG studies [34].

For  $n = 0.1$  and  $J = 2.5$ , which corresponds to a point in the spin-gap phase, we observe that the Fermi surface is destroyed. For the higher densities in Figs. 4.16 (b) and (c), such a flattening of  $n(k)$  around  $k_F$  cannot be observed because the spin gap for such parameter values is very small. An interesting feature seen for such densities is the increase of  $n(k)$  for  $k > k_F$ , contrary to what is expected in a weakly correlated metal. Such a behavior is indicative of the presence of spectral

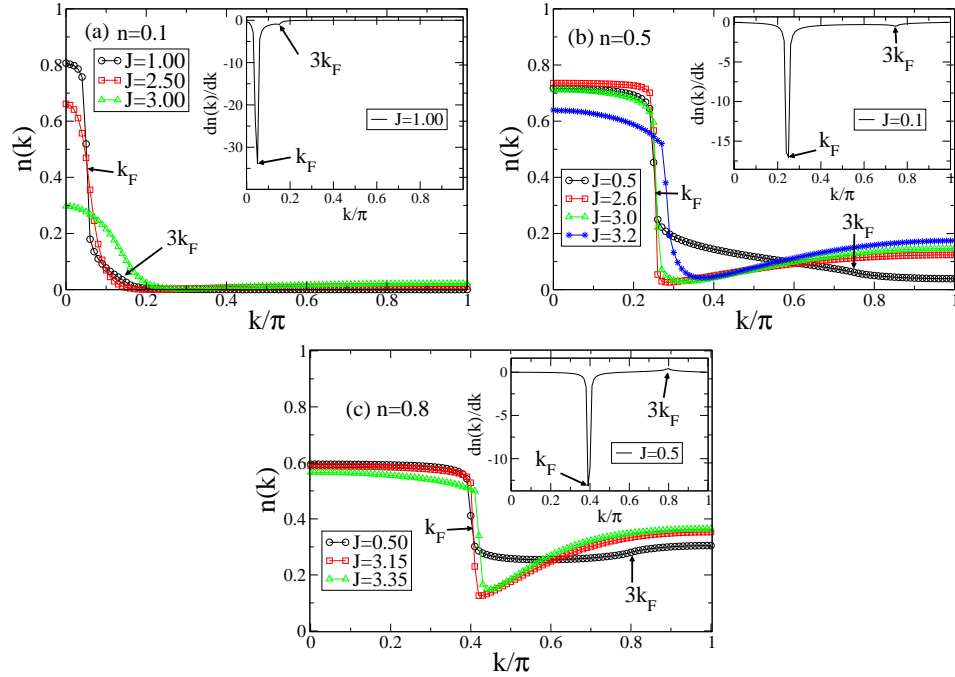


Figure 4.16: Momentum distribution function  $n(k)$  for  $L = 200$  and for different values of  $n$  and  $J$ .

weight below the Fermi energy for wavevectors  $k > k_F$ , as was already observed in previous quantum Monte Carlo simulations [58]. As we explained in the chapter of Luttinger liquids this spectral weight is due to the effect of interactions between density fluctuations with different chirality mediated by the anomalous dimension  $K_\rho$ . On the contrary, for  $n = 0.1$  and  $J = 2.0$  (where  $K_\rho \approx 1.0$ )  $n(k)$  has a shape closer to the momentum distribution in the free case.

#### 4.4.2 Gapless superconducting phase

In this section we examine closer the pairing correlation functions, both for singlet as well as for triplet pairing. The long-distance behavior of the correlation function for singlets was already given in Eq. (4.14) and for triplet pairing is as follows (Eq. (2.23)):

$$\begin{aligned} \langle \Delta_T^\dagger(r) \Delta_T(0) \rangle &\sim D_0 r^{-(1+1/K_\rho)} \\ &+ D_1 \cos(2k_F r) r^{-(K_\rho+1/K_\rho+2)}, \end{aligned} \quad (4.16)$$

where the operator  $\Delta_T$  corresponds to triplet superconducting pairing (see Eq. (4.6)). Here we have ignored logarithmic corrections.

In the gapless superconducting phase, since there is no gap to triplet states, and the leading power-law is the same for both singlet and triplet channels, the question may arise about the relative strength of singlet- (SS) and triplet-superconductivity (TS), as already pointed out by Pruschke and Shiba [59].

Figure 4.17 shows the behavior of both correlation functions in real space as compared to the asymptotic forms given in Eqs. (4.14) and (4.16). In Fig. 4.17 (a) a comparison is given with Eq. (4.14), where the constants  $C_0$  and  $C_1$  were adjusted through a least-square fit, while the value for  $K_\rho$  was taken from the determination detailed in Sec. 4.1 ( $K_\rho = 1.12$  for the parameter values in Fig. 4.17). In order to be able to display the power-law behavior of  $P_S(x)$ , we use a doubly logarithmic

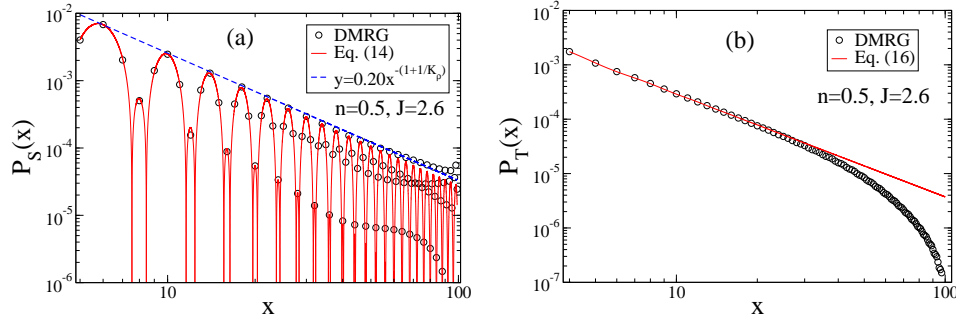


Figure 4.17: Singlet  $P_S(x)$  and triplet  $P_T(x)$  correlation functions for  $n = 0.5$ ,  $J = 2.6$  and  $L = 200$ . For the singlet case we plot  $|P_S(x)|$ . The straight lines correspond to power-laws determined by  $K_\rho$ . Both the singlet and triplet channel have the same exponent.

scale, and actually plot the modulus of  $P_S(x)$ , since the  $2k_F$  oscillations lead to sign changes of the correlation function. The dashed line through the maxima makes furthermore evident, that the power-law decay can be well described by the power of the first term in Eq. (4.14). Deviations are observed for  $x > 60$ , possibly due to boundary effects. On the other hand, Fig. 4.17 shows that the decay of  $P_T$  can be well described by the same power-law as for  $P_S(x)$ , with deviations that start at  $x > 30$ . While there are certainly boundary effects, Fig. 4.18 shows that their incidence on

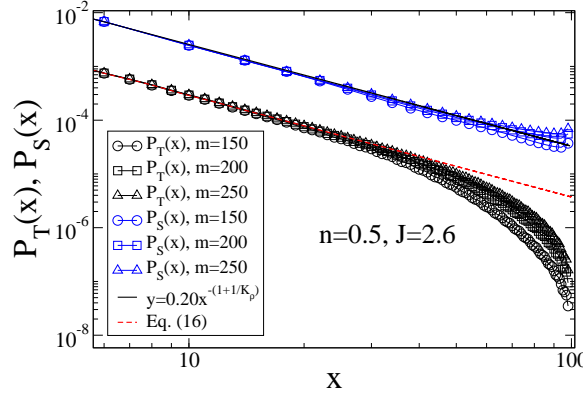


Figure 4.18: Singlet  $P_S(x)$  and triplet  $P_T(x)$  correlation functions for  $n = 0.5$ ,  $J = 2.6$ ,  $L = 200$  and  $m = 150, 200, 250$ . We observe at long distances that on a double-logarithmic scale,  $P_T(x)$  becomes more linear upon increasing  $m$ , i.e. the spurious exponential decay introduced by the DMRG cutoff decreases. Note, however, that  $P_S(x)$  becomes less linear at long distances when increasing  $m$ . We associate this behavior with the open boundary conditions used.

the correlation functions changes by increasing the precision of the DMRG runs. There we display the results for both correlation functions when the number  $m$  of states kept in the reduced density matrix is increased. While  $P_T(x)$  approaches the power-law at larger distances,  $P_S(x)$  departs from it. At the highest accuracy used, both depart from the predicted power-laws for  $x > 50$ . We associate this behavior with the open boundary conditions used and with the spurious exponential decay introduced by the DMRG cutoff.

In Fig. 4.19 we also show both singlet and triplet pair correlations in momentum space. The amplitude of  $P_S(k = 0)$  for the singlet case is one order of magnitude larger than  $P_T(k = 0)$  for the triplet case. Since  $P_S(k = 0)$  gives the number of pairs with momentum zero, it is clear that

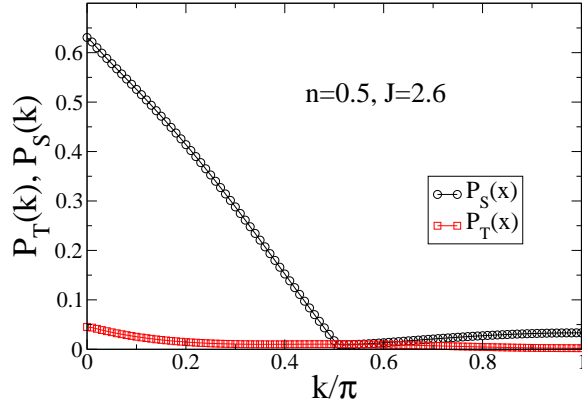


Figure 4.19: Triplet and singlet pair-pair structure factors for  $n = 0.5$ ,  $J = 2.6$  and  $L = 200$ .

singlet superconductivity dominates. The LL theory also predicts SS as the dominant order due to logarithmic corrections, however, within our precision and for the system sizes under study, we were not able to observe them.

#### 4.4.3 Competing orders in the spin-gap phase. Charge density wave vs singlet superconductivity

The peaks of Fig. 4.13 (a) at  $2k_F$  and Fig. 4.15 (a) at  $k = 0$  for  $J = 2.5$  show that CDW and SS are competing orders in the spin-gap phase. On entering this phase, electrons pair into singlets, such that the spin-spin and triplet pair-pair correlation functions are exponentially suppressed. While the singlet-pair-pair correlation function has the long-distance behavior given by Eq. (4.15), the density-density correlation function in the LE phase behaves as (Eq. (2.28))

$$\langle n(r)n(0) \rangle = A_0 r^{-2} + A_1 \cos(2k_F r) r^{-K_\rho}. \quad (4.17)$$

According to these expressions and since in the spin-gap region  $K_\rho > 1$ , then SS should be the dominant order. This is in fact the case shown in Fig. 4.20 where we observe that  $P_S(x)$  has the

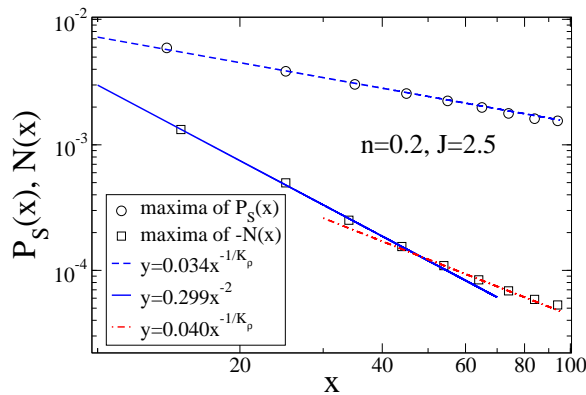


Figure 4.20: Maxima of  $P_S(x)$  and  $-N(x)$  in real space for  $L = 200$ ,  $n = 0.2$  and  $J = 2.5$  on a log-log scale. the power-laws are determined by  $K_\rho$  through Eqs. (4.15) and (4.17).

slowest decay. The parameters for this figure are  $n = 0.2$  and  $J = 2.5$ , i.e. deep in the spin-gap region. Due to the  $2k_F$  oscillations, only the maxima of the functions are plotted. The different lines

(dashed one for  $P_S(x)$  and full and dashed-dot lines for  $N(x)$ ) correspond to the powers appearing in the first term of Eq. (4.15), and the powers appearing in Eq. (4.17) for  $N(x)$ . The latter shows a crossover from a behavior at short distances dominated by the first term in Eq. (4.17) to the long-distance behavior determined by the power of the second term. For the parameters considered here we obtained from  $N(k \rightarrow 0)$ , as given by Eq. (4.9),  $K_\rho = 1.48$ . In this case  $P_S(k = 0)$  diverges

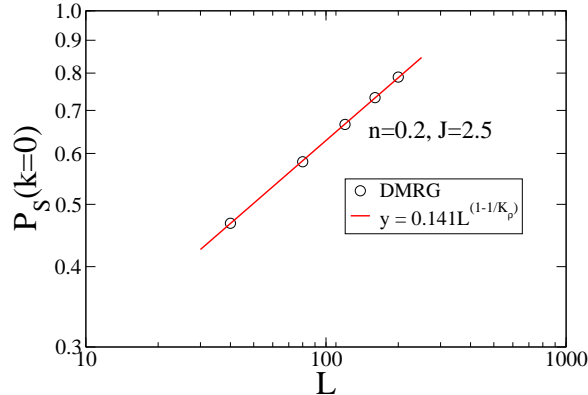


Figure 4.21: Scaling of  $P_S(k = 0)$  in the thermodynamic limit for  $n = 0.2$  and  $J = 2.5$  (spin-gap phase).

in the thermodynamic limit, as shown by Fig. 4.21 with an exponent determined by  $K_\rho$ , however, the system being one-dimensional, no true long-range order is present, since  $P_S(k = 0)/L$  vanishes in the thermodynamic limit. Nevertheless, as shown in Fig. 4.10, the spin gap increases as the density decreases, reaching a sizable value on approaching phase separation ( $\Delta E_S \sim 0.15t$ ). Hence, singlets bind at a finite temperature scale below the spin gap.

Another interesting aspect of this phase is that due to open boundary conditions, a change in the periodicity of the Friedel oscillations in the density can be directly observed, as shown in Fig. 4.22. This can be seen as a  $2k_F$  CDW coexisting with a superconducting state in the spin-gap phase.

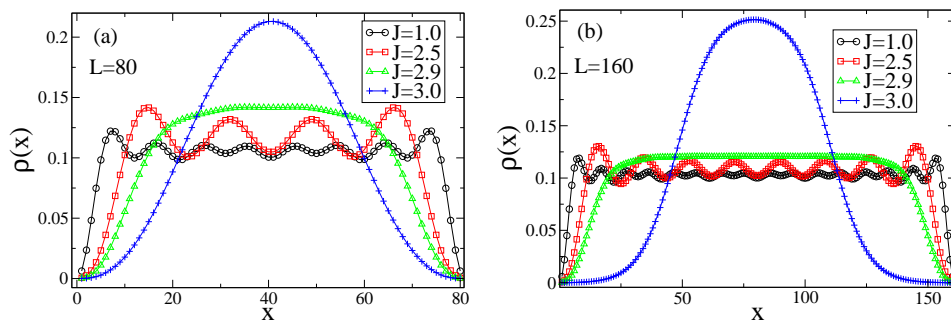


Figure 4.22: Density in real space  $\rho(x)$  for  $n = 0.1$  and (a):  $L = 80$ , (b):  $L = 160$ . In the metallic regime ( $J = 1.0$ ) we have one peak per particle due to Friedel oscillations. When  $J$  is increased the particles start to form pairs. This happens in the spin-gap region ( $J = 2.5$ ). Increasing  $J$  even more the particles tend to be confined in a region smaller than the system size (phase separation).

However, following the arguments related to Fig. 4.7, and the fact that the leading singularity is related to SS, these density oscillations can be understood as due to bound pairs, which because of the constraint of the  $t$ - $J$  model behave as hard-core bosons. Hence, the density of the hard-core

bosons in one dimension will show the same oscillations as the density of the equivalent Jordan-Wigner fermions, corresponding to the number of pairs in the system. As an example we show in Fig. 4.22 the density profiles for a density  $n = 0.1$  and values of  $J$  corresponding to the repulsive LL ( $J = 1$ ) and the spin-gap ( $J = 2.5$ ) phases, and two values of  $J$  on entering the phase separation, for two different system sizes (Fig. 4.22 (a):  $L = 80$  and Fig. 4.22 (b):  $L = 160$ ). In both cases, the number of oscillations is halved, corresponding to Friedel oscillations for half the number of particles.

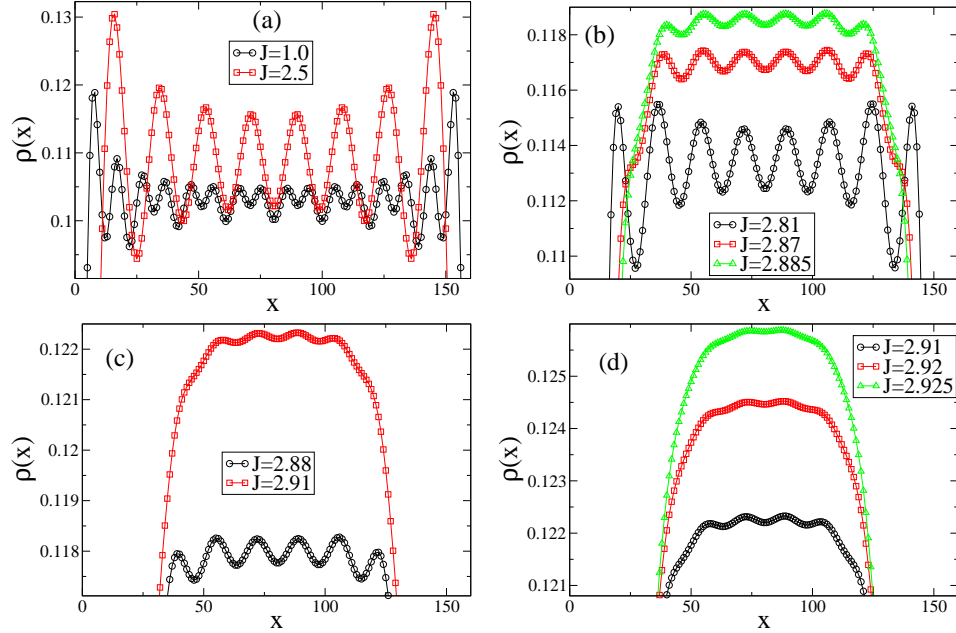


Figure 4.23: Density in real space  $\rho(x)$  for  $n = 0.1$ ,  $L = 160$  and different values of  $J$ . In Fig. 4.23(a) we observe the pairing of particles. In the other figures only particles at the boundaries of the particle-rich region merge into one loose cloud but the particles in the middle do not cluster further.

Since the coupling driving the pairing mechanism is the nearest neighbor exchange  $J$ , it could be argued [32] that before entering phase separation, clustering in groups with more than two fermions may exist. In order to answer this question we observe how the modulations of  $\rho(x)$ , displayed in Fig. 4.23, change when we increase  $J$  by very small amounts before phase-separation is reached. There, we clearly see how a loosely bound cloud forms at the border of the particle rich region, but pairs remain as such in the middle of that region. Starting with 16 electrons on 160 sites, we can see the formation of pairs on entering the spin-gap region, such that 8 pairs are clearly visible (Fig. 4.23 (a)). Going up to the point where density oscillations corresponding to two pairs are still visible (Fig. 4.23 (d)), we see that the rest of the pairs merged on the sides of the particle rich region, until phase-separation is reached. Note that the density oscillations in Figs. 4.23 are on a very small scale and are not noticeable at the scale used in Figs. 4.22. Once in the phase-separated region, a density distribution results, where a cloud at the center of the system appears, leaving an appreciable number of empty sites, as shown in Figs. 4.22. Hence, clusters with more than a pair do not form a uniform phase, and in particular, a state with four bound electrons does not form. Still inside the phase-separated region, appreciable changes of the density as a function of  $J$  take place. This will be the subject of the next section.

## 4.4.4 Phase separation and electron solid phase

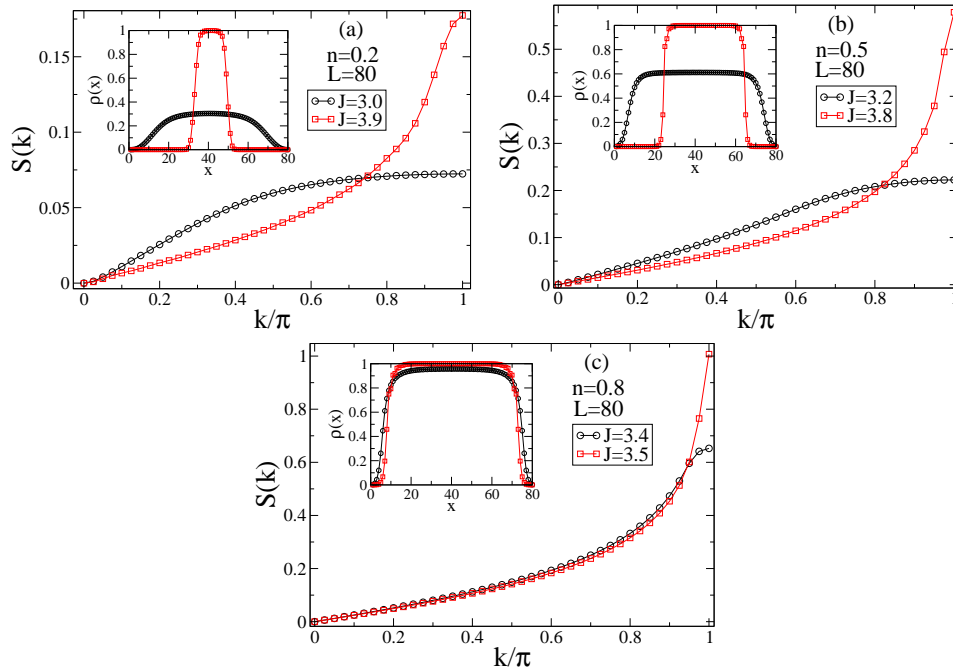


Figure 4.24: Magnetic structure factor  $S(k)$  in the phase-separated region for values of  $J$  close to the boundary and at the value, where a peak at  $k = \pi$  emerges. Insets: the corresponding density profiles

As shown in Fig. 4.22 at values of  $J$  just after the phase boundary ( $J = 3$ ), particles merge into a single island, occupying only part of the available space. However, as shown by the magnetic structure factor in Fig. 4.14, for values of  $J$  inside phase-separation, and close to the boundary, a broad maximum is seen at  $k = \pi$ , but no sharp peak indicative of the formation of a spin chain. Therefore, the naïve picture of a compact region does not apply yet. Figure 4.24 shows  $S(k)$  at three different densities for the values of  $J$  where the system enters phase-separation and the one at which a sharp maximum can be observed at  $k = \pi$ . The insets display also the corresponding density profiles, making evident that when  $S(k)$  has a sharp maximum at the antiferromagnetic wavevector, an island with density  $n = 1$  is formed. Unfortunately, since the formation of such islands implies that there are many almost degenerate states very close to the ground state, namely those connected by translation, is not possible to perform a careful finite-size analysis to determine the boundary to such a phase in the thermodynamic limit. In fact, in Figs. 4.24 it can be seen that the density profiles reaching  $n = 1$  break spontaneously reflexion symmetry about the central bond, an artifact due to the many degenerate states mentioned above.

The difference in density profiles shown in Figs. 4.24 makes also evident that by having an expanded cloud, most probably with pairs inside, as discussed in the previous section, still kinetic energy is present in the cloud that is quenched only when  $J$  reaches a large enough value. Since we are limited in the sizes of the systems we can simulate, we cannot determine with confidence a critical value of  $J$ , where the system forms an electron solid [34]. It was argued [34] that in this case  $J_c$  should be independent of the band filling  $n$ , since the only requirement is to form an island with  $n = 1$ . We observe in our simulations a weak dependence on the density, but our results are limited to  $L = 80$ , the largest size where meaningful results can be obtained in this region. Placing the location of the

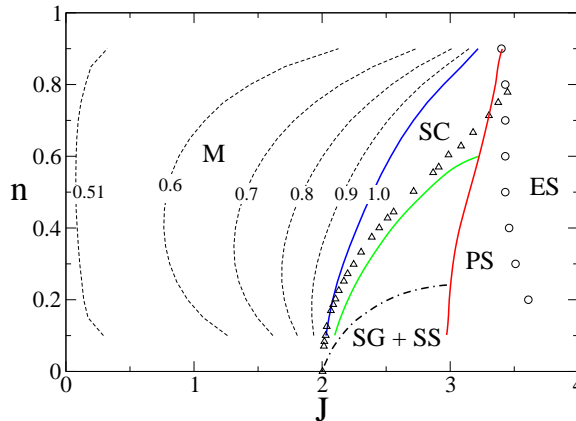


Figure 4.25: Phase diagram of Fig. 4.1 including the electron solid phase (ES). The circles denote the position at which a peak in  $S(k)$  appears at  $k = \pi$ , and at the same time, the phase separated island reaches a density  $n = 1$ . Triangles reproduce the results of Ref. [29] and the dashed-dot line those of Ref. [28].

value of  $J$ , where the island with  $n = 1$  forms for  $L = 80$  at different densities, leads to an almost density independent value, as shown in Fig. 4.25. The largest deviations are observed at the lowest densities. Although the number of particles is possibly too low to make a definite statement, it could be argued that at low densities the formation of the electron solid leads to an appreciable loss of kinetic energy, that has to be compensated by a larger value of  $J_c$ . The same can be argued in the high density region, such that being limited to small systems may lead to lower values of  $J_c$ , since, as displayed in Fig. 4.24 (c), for very few holes the loss in kinetic energy with open boundary conditions can be negligible.

Figure 4.25 also displays the differences in the results for the onset of the spin-gap region that were obtained on the basis of a variational calculation combined with the power method [28] on the one hand, and a RG analysis complemented by exact diagonalizations of systems with up to 30 sites [29], on the other hand. While the agreement with the latter results is in general quite good, the largest deviations appear as the onset line approaches the phase-separation line. This can be possibly due to the fact that the RG analysis did not take explicitly into account the appearance of phase-separation, that in general leads to a strong finite size dependence. On the other hand, a precise determination with DMRG becomes extremely demanding at low densities ( $n \leq 0.1$ ), due to the need of very large systems in order to have a large enough number of particles to faithfully represent a phase. The large disagreement with the results of Ref. [28] could point to the difficulties of the power method to deal with fermionic systems at high density, due to the strong increase of the dimension of the required Hilbert space.

# Chapter 5

## Real-Time Dynamics

In this chapter we study the time evolution of a wavepacket, corresponding to a fermion with spin up injected into the ground state of the  $t$ - $J$  model, by means of t-DMRG [13, 26], in order to investigate the phenomenon of spin and charge fractionalization in one dimension at low and high energies considering a strongly correlated system. We use the exact results for the one-particle spectral function at the supersymmetric (SUSY) point  $J = 2t$  obtained by means of the Bethe-Ansatz solution [8, 36, 60] in order to interpret our numerical results. These exact results will help us to understand the different portions into which the injected wavepacket splits. Before going into the real-time dynamics results let us first briefly explain how we obtain the Bethe-Ansatz results. We refer the reader to the original references [8, 36, 60–63] for more details about the Bethe-Ansatz method.

### 5.1 Bethe-Ansatz

#### 5.1.1 Dispersion relations

At the supersymmetric (SUSY) point <sup>1</sup>  $J = 2t$  the 1D  $t$ - $J$  model can be solved exactly using Bethe-Ansatz [8, 36, 60]. The Bethe-Ansatz solution is expressed in terms of two independent degrees of freedom,  $c$  and  $s$ , related to two different kinds of pseudoparticles [60]. In the low energy case or Luttinger Liquid (LL) regime the  $c$  ( $s$ ) pseudoparticle carries only charge (spin) and it is called holon (spinon). However, in general these two degrees of freedom might contain contributions from both, charge and spin, as we will see later on in our numerical simulations. We consider only the zero magnetization case. The  $c$  and  $s$  energy dispersions are given by

$$\epsilon_c(q) = 4t \int_{-B}^B dr 8r \frac{[\bar{\Phi}_{s,c}(r, r_c^0(q)) - \bar{\Phi}_{s,c}(r, Q)]}{(1 + (2r)^2)^2}, \quad (5.1)$$

$$\epsilon_s(q) = -\frac{4t}{1 + (2r_s^0(q))^2} + 4t \int_{-B}^B dr 8r \frac{[\bar{\Phi}_{s,s}(r, r_s^0(q)) - \bar{\Phi}_{s,c}(r, B)]}{(1 + (2r)^2)^2}, \quad (5.2)$$

where  $q \in [-(\pi - k_F), (\pi - k_F)]$ ,  $k_F = \pi n/2$ ,  $n = N/L$ , with  $N$  the number of electrons and  $L$  the number of lattice sites. The ground-state rapidities  $r_\alpha^0(q)$  (with  $\alpha = c, s$ ) are defined in terms of their inverse functions

---

<sup>1</sup>For this value of  $J$  the 1D  $t$ - $J$  Hamiltonian can be written in terms of projection operators that form a basis of the supersymmetric  $SU(2|1)$  Lie algebra [64].

$$\begin{aligned}
q_c^0(r) &= 4 \int_{-B}^B dr' \frac{\bar{\Phi}_{s,c}(r', r)}{1 + (2r')^2}, \quad r \in [-\infty, \infty], \\
q_s^0(r) &= 2 \arctan(2r) + 4 \int_{-B}^B dr' \frac{\bar{\Phi}_{s,s}(r', r)}{1 + (2r')^2}, \quad r \in [-\infty, \infty].
\end{aligned} \tag{5.3}$$

The functions  $\bar{\Phi}_{\alpha,\alpha'}(r, r')$  are the phase shifts defined in terms of the following self-consistent integral equations

$$\bar{\Phi}_{s,c}(r, r') = -\frac{1}{\pi} \arctan(2[r - r']) + \int_{-B}^B dr'' G(r, r'') \bar{\Phi}_{s,c}(r'', r') \tag{5.4}$$

and

$$\begin{aligned}
\bar{\Phi}_{s,s}(r, r') &= \frac{1}{\pi} \arctan(r - r') - \frac{2}{\pi^2} \int_{-Q}^Q dr'' \frac{\arctan(2[r'' - r'])}{1 + (2[r - r''])^2} \\
&\quad + \int_{-B}^B dr'' G(r, r'') \bar{\Phi}_{s,s}(r'', r').
\end{aligned} \tag{5.5}$$

The kernel  $G(r, r')$  reads,

$$\begin{aligned}
G(r, r') &= -\frac{1}{\pi} \frac{1}{1 + (r - r')^2} + \frac{4}{\pi^2} \int_{-Q}^Q dr'' \frac{1}{1 + (2[r - r''])^2} \frac{1}{1 + (2[r'' - r'])^2} \\
&= -\frac{1}{\pi} \frac{1}{1 + (r - r')^2} \left[ 1 - \frac{1}{2} \left( t(r) + t(r') + \frac{l(r) - l(r')}{2(r - r')} \right) \right],
\end{aligned} \tag{5.6}$$

where

$$\begin{aligned}
t(r) &= \frac{1}{\pi} \sum_{j=\pm 1} (j) \arctan(2[r + jQ]), \\
l(r) &= \frac{1}{\pi} \sum_{j=\pm 1} (j) \ln(1 + (2[r + jQ])^2).
\end{aligned} \tag{5.7}$$

In the thermodynamic limit the ground state corresponds to symmetrical compact occupancies of both  $\alpha = c, s$  momentum bands (5.1), (5.2) with Fermi momentum  $q_{F\alpha}$  given by

$$q_{Fc} = (\pi - 2k_F), \quad q_{Fs} = (\pi - k_F), \tag{5.8}$$

respectively. The momentum-ground-state occupancies  $q \in [-q_{Fc}, q_{Fc}]$  and  $q \in [-q_{Fs}, q_{Fs}]$  refer to rapidity ranges  $r \in [-Q, Q]$  and  $r \in [-B, B]$ , respectively, such that

$$r_c^0(\pm q_{Fc}) = \pm Q, \quad r_s^0(\pm q_{Fs}) = \pm B, \tag{5.9}$$

where  $Q$  and  $B$  might be obtained by solving self-consistently the normalization conditions given by the following integral equations

$$\begin{aligned}
\pi - 2k_F &= 4 \int_{-B}^B dr \frac{\bar{\Phi}_{s,c}(r, Q)}{1 + (2r)^2}, \\
\pi - k_F &= 2 \arctan(2B) + 4 \int_{-B}^B dr \frac{\bar{\Phi}_{s,s}(r, B)}{1 + (2r)^2}.
\end{aligned} \tag{5.10}$$

We rather proceed solving Eqs. (5.4) and (5.5) assuming that  $Q$  and  $B$  are known and then we use Eqs. (5.10) and  $k_F = \pi n/2$  to know the corresponding electronic density  $n$ . In Fig. 5.1 we show the resulting dispersion relations for different values of  $n$ . The ground-state energy reference is defined such that  $\epsilon_\alpha(\pm q_{F\alpha}) = 0$  and the momentum range is given by  $q \in [-(\pi - k_F), (\pi - k_F)]$ .

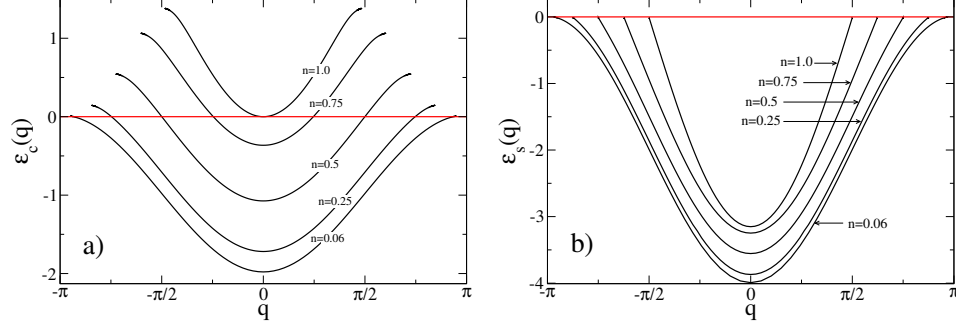


Figure 5.1: Solution of the dispersion relations (5.1) and (5.2) for different electronic densities  $n$ . The ground-state energy reference is defined such that  $\epsilon_\alpha(\pm q_{F\alpha}) = 0$  and the momentum range is given by  $q \in [-(\pi - k_F), (\pi - k_F)]$ .

We define corresponding  $c$  and  $s$  band velocities as,

$$\begin{aligned} v_\alpha(q) &\equiv \partial \epsilon_\alpha(q) / \partial q, \\ v_\alpha &\equiv v_\alpha(q_{F\alpha}), \quad \alpha = c, s. \end{aligned} \quad (5.11)$$

Note from Fig. 5.1 that in the limit  $n \rightarrow 1$ , we have  $v_c \rightarrow 0$  and  $v_s$  is finite. This is consistent with the fact that for  $n = 1$ , due to the non-double occupancy constraint, the charge degree of freedom is frozen and only spin transport is possible at low energies. According to the Bethe-Ansatz, the number  $N_{a_\alpha}$  of discrete momentum values and the number  $N_\alpha$  of pseudoparticles occupying the bands  $\alpha = c, s$  are given by

$$\begin{aligned} N_{a_c} &= (L - N_\uparrow), & N_{a_s} &= (L - N_\downarrow), \\ N_c &= (L - N), & N_s &= (L - N_\uparrow), \end{aligned} \quad (5.12)$$

respectively.  $N_\uparrow$  stands for the number of particles with spin up. Note from these equations that for  $n = 0$ , we have that  $N_c = N_{a_c} = L$ , that is, the  $c$  band is completely full. For  $n = 1$ , we have that  $N_c = 0$ , that is, the  $c$  band is completely empty. Note also that the Bethe-Ansatz formalism inverts the role of particles and holes. Since we are working at zero magnetization ( $N_\uparrow = N_\downarrow$ ), the  $s$  band is always full ( $N_s = N_{a_s}$ ). All these last remarks can be also observed in Fig. 5.1.

### 5.1.2 One-electron addition spectral function dispersion lines

While performing electron-injection experiments or inverse-photoemission experiments one of the quantities to be considered is the one-electron addition spectral function which is defined by

$$A(k, \omega) = \sum_i |\langle \psi_i, N+1 | c_k^\dagger | \psi_0, N \rangle|^2 \delta(\omega - \epsilon_i), \quad (5.13)$$

where  $|\psi_i, N\rangle$  are eigenstates of the Hamiltonian with  $N$  number of electrons and  $\epsilon_i = E_i^{N+1} - E_0^{N+1}$  is the excitation energy. The subindex 0 refers to the ground state.  $A(k, \omega)$  represents the

probability of finding the system in any of its eigenstates with energy  $\omega$  after adding one electron with momentum  $k$  into the system.

According to Eqs. (5.12), when one more electron with spin up is added into the chain, the quantum numbers  $N_c$  and  $N_s$  are decreased by one, that is, one pseudohole is created on each band. Since  $N$  and  $N_\uparrow$  are conserved quantities,  $N_c$  and  $N_s$  are also conserved. Therefore, the resulting state after the electron addition can be written as a linear combination of excitations involving energy eigenstates generated by removal of one  $c$  pseudoparticle and one  $s$  pseudoparticle; and pseudo particle-hole excitations in each band. In the case under study, most of the  $A(k, \omega)$  spectral weight results from considering the first case of excitation. In this case, the corresponding one-electron spectrum is of the form,

$$\begin{aligned}\omega(k) &= -\epsilon_c(q_c) - \epsilon_s(q_s), \quad k = \pm 2k_F - q_c - q_s, \\ q_c &\in [-(\pi - 2k_F), (\pi - 2k_F)], \quad q_s \in [-(\pi - k_F), (\pi - k_F)].\end{aligned}\quad (5.14)$$

The momentum  $\pm 2k_F$  in the  $k$  expression of Eq. (5.14) refers to two excitation branches which emerge due to a collective shake-up effect of all  $c$  band momentum values. This shake-up effect is associated with a collective shift  $\pm\pi/L$  of all the corresponding  $c$  and/or  $s$  band momentum values that occurs during a transition to an excited state.

The two most important spectral lines are what we called the  $c$  and  $s$  branch lines. The  $c$  line is generated by fixing the  $s$  hole in its Fermi surface (i.e. at  $\pm q_{Fs}$ ) while the momentum  $q_c$  of the  $c$  hole is free to change. Similarly, the  $s$  line is generated by fixing the  $c$  hole in its Fermi surface (i.e. at  $\pm q_{Fc}$ ) while the momentum  $q_s$  of the  $s$  hole is free to change. The sign  $\pm$ , which refers to the chirality of the pseudo-hole in the Fermi surface, together with the  $\pm$  sign coming from the collective shake-up will produce four different branches per degree of freedom. The spectral function has above these lines a power-law behavior with an exponent that can be computed using the pseudofermion dynamical theory (PDT) [60, 65–67] in a similar manner as it was done in a previous study of the Hubbard model [65]. For such calculation, the PDT theory considers contributions to the spectral function coming from a tower of pseudo particle-hole excitations in each band. For the  $t$ - $J$  model the exponent  $\zeta_c^l$  for the  $c$  line is given by

$$\begin{aligned}\zeta_c^l(k) &= -1 + \sum_{\alpha=c,s} \sum_{\iota=\pm 1} \left( -\iota \frac{\xi_{\alpha s}^0}{2} \mp \frac{(\xi_{\alpha c}^1 - l \xi_{\alpha s}^1)}{2} - \Phi_{\alpha,c}(\iota q_{F\alpha}, q_c) \right)^2, \\ k &= \pi \pm (2k_F - l k_F) - q_c, \quad q_c \in [-(\pi - 2k_F), (\pi - 2k_F)],\end{aligned}\quad (5.15)$$

and for the  $s$  line,

$$\begin{aligned}\zeta_s^l(k) &= -1 + \sum_{\alpha=c,s} \sum_{\iota=\pm 1} \left( -\iota \frac{\xi_{\alpha c}^0}{2} \pm (1-l) \frac{\xi_{\alpha c}^1}{2} - \Phi_{\alpha,s}(\iota q_{F\alpha}, q_s) \right)^2, \\ k &= \pi \pm (l-1)(\pi - 2k_F) - q_s, \quad q_s \in [-(\pi - k_F), (\pi - k_F)].\end{aligned}\quad (5.16)$$

The sign,  $l = \pm$ , is defined such that, when the chirality of the pseudohole in its Fermi surface and the sign of the collective shake-up are equal (opposite),  $l = -1$  ( $l = 1$ ). The parameters  $\xi_{\alpha\alpha'}^\gamma$  can be obtained using the expression

$$\xi_{\alpha\alpha'}^\gamma = \delta_{\alpha,\alpha'} + \sum_{\iota=\pm 1} (\iota)^\gamma \Phi_{\alpha,\alpha'}(q_{F\alpha}, \iota q_{F\alpha'}), \quad (5.17)$$

where  $\gamma = 0, 1$ . The phase shifts are given by

$$\Phi_{\alpha,\alpha'}(q, q') = \bar{\Phi}_{\alpha,\alpha'}(r_\alpha(q), r_{\alpha'}(q')), \quad (5.18)$$

where  $\bar{\Phi}_{s,c}(r, r')$  and  $\bar{\Phi}_{s,s}(r, r')$  are given in Eqs. (5.4) and (5.5), respectively, and  $\bar{\Phi}_{c,c}(r, r')$  and  $\bar{\Phi}_{s,s}(r, r')$  can be determined by

$$\bar{\Phi}_{c,c}(r, r') = \frac{2}{\pi} \int_{-B}^B dr'' \frac{\bar{\Phi}_{s,c}(r'', r')}{1 + (2[r - r''])^2}, \quad (5.19)$$

and

$$\bar{\Phi}_{s,s}(r, r') = -\frac{1}{\pi} \arctan(2[r - r']) + \frac{2}{\pi} \int_{-B}^B dr'' \frac{\bar{\Phi}_{s,s}(r'', r')}{1 + (2[r - r''])^2}. \quad (5.20)$$

Since we are interested in the dynamics of a wavepacket injected to the chain, we will focus only on those lines with negative exponent, i.e. where the spectral function is singular and therefore it has there its highest weight. By solving the above equations of the exponents, we have obtained that the lines with negative exponents are those where the sign of the shake-up and the chirality of the hole at the Fermi surface have opposite sign, i.e. for  $l = 1$ . Therefore, only two branches per degree of freedom have to be considered. Then for  $l = 1$ , the  $c$  branch lines spectra are of the form,

$$\begin{aligned} \omega_c(k) &= -\epsilon_c(q_c), \quad q_c \in [-(\pi - 2k_F), (\pi - 2k_F)], \\ k &= \pi \pm k_F - q_c, \end{aligned} \quad (5.21)$$

and the  $s$  branch lines spectra are

$$\begin{aligned} \omega_s(k) &= -\epsilon_s(q_s), \quad q_s \in [-(\pi - k_F), (\pi - k_F)], \\ k &= \pi - q_s, \end{aligned} \quad (5.22)$$

where the dispersion relations  $\epsilon_\alpha(q)$  were obtained in the previous section and  $k$  is the momentum of the incoming electron. Note that for the  $c$  lines there is no energy contribution coming from the  $s$  pseudoparticles because in this case  $q_s$  has been fixed to its Fermi momenta, i.e.  $\epsilon_s(q_s = \pm q_{Fs}) = 0$ . Similarly the  $s$  lines have no energy contribution from the  $c$  pseudoparticles.

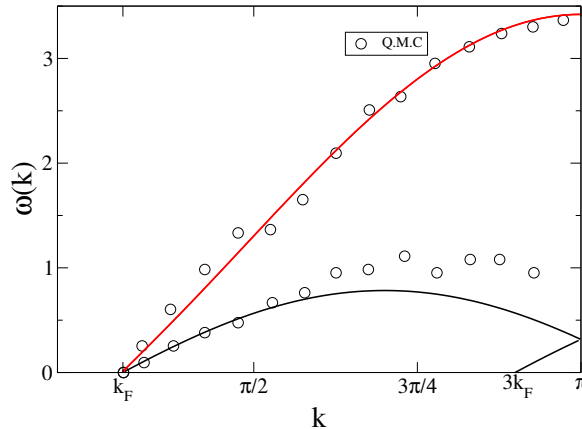


Figure 5.2: Lines where  $A(k, \omega)$  have divergences according to the Bethe-Ansatz solution for  $n = 0.6$ . The black line stand for the  $c$  line and the red line for the  $s$  line (see the tex for explanation). The black circles corresponds to the main two features observed in a previous QMC study [58].

In Fig. 5.2 we show an example of the most important spectral lines given by the Bethe-Ansatz for  $n = 0.6$ . The black line stands for the  $c$  line and the red line for the  $s$  line. The black line going

from  $k_F$  to  $\pi$  corresponds to excitations where the  $s$  hole fixed at its Fermi surface has positive chirality, that is,  $q = +q_{Fs}$ . For the black line going from  $3k_F$  to  $\pi$ , the chirality of that  $s$  hole is negative, that is,  $q = -q_{Fs}$ . In the  $s$  line the two kind of chiralities of the  $c$  hole at its Fermi surface are present. This is because  $k = \pi - q_s$  and  $\omega_s(k)$ , in Eq. (5.22), do not depend explicitly on  $l$  and on the shake-up sign (and therefore also on the chirality), because this dependency has been eliminated by putting  $l = 1$  into Eq. (5.16). The black circles corresponds to the main two features observed in a previous Quantum Monte Carlo (QMC) study of the  $t$ - $J$  model [58]. We observe that these two QMC features are in very good agreement with the Bethe-Ansatz spectral lines indicating that, in fact, only the  $c$  and  $s$  lines are the important spectral lines to be taken into account. The presence of this two main features are also a signal that the system might be separated into two independent degrees of freedom.

Considering that for the  $c$  lines the  $s$  hole has fixed momentum  $\pm q_{Fs}$  whereas the momentum  $q_c$  of the  $c$  hole can vary, we can derive that

$$\frac{\partial\omega(k)}{\partial k} = -\frac{\partial\epsilon_c(q_c(k))}{\partial q_c} \frac{\partial q_c}{\partial k} = \frac{\partial\epsilon_c(q_c(k))}{\partial q_c} = v_c(q_c(k)), \quad (5.23)$$

i.e. the velocity of the  $c$  hole is just the slope of the black lines in Fig. 5.2, while the  $s$  hole in its Fermi surface moves with its Fermi velocity  $\partial\epsilon_s(q_{Fs})/\partial q_s$ .

Similarly to the  $c$  lines, for the  $s$  lines we have that

$$\frac{\partial\omega(k)}{\partial k} = -\frac{\partial\epsilon_s(q_s(k))}{\partial q_s} \frac{\partial q_s}{\partial k} = \frac{\partial\epsilon_s(q_s(k))}{\partial q_s} = v_s(q_s(k)), \quad (5.24)$$

i.e. the velocity of the  $s$  hole is just the slope of the red lines in Fig. 5.2 while the  $c$  hole in its Fermi surface moves with its Fermi velocity  $\partial\epsilon_c(q_{Fc})/\partial q_c$ . In the next section we will compare these velocities with those obtained by the t-DMRG in order to identify the different parts into which the added electron is split.

## 5.2 Time dependent DMRG simulations

In the previous section we collected all the necessary information for obtaining the most important branches of the one-electron spectral function  $A(k, \omega)$  which we will use for the interpretation of our numerical simulations. However,  $A(k, \omega)$  does not show direct information on the charge and spin of the two different elementary excitations,  $c$  and  $s$  pseudoparticles. It is well known that close to  $k_F$  the Luttinger Liquid (LL) theory predicts total spin-charge separation [3] where there are two independent modes, one carrying only charge (holon) and another one carrying only spin (spinon). The question arises whether this picture is still valid for higher energies. In this section we present evidences at high energies and for the  $t$ - $J$  model (Eq. (1.1)) that indicate deviations from this LL picture.

In order to investigate the charge of the elementary excitations we carry out a kind of theoretical experiment using the t-DMRG method explained in Sec. 3.2. We start with the system in the ground state and then we inject one electron with spin up into the chain in the form of a gaussian wavepacket. Then we let the system evolve and we measure the charge and spin densities, relative to the ground state, in real time. As we explain in detail in Appendix B.1.1, in the case that the system consists of only non-interacting particles, we see a wavepacket propagating with the group velocity given by the slope of the dispersion relation of such particles. In the case of an interacting system the wavepacket will split into more than one wavepacket corresponding to different excitations of the system.

To create a gaussian wavepacket state  $|\psi\rangle$  centered at  $x_0$ , width  $\Delta_x$  and with average momentum  $k_0$ , we apply the operator  $\psi^\dagger$  to the ground state  $|G\rangle$ :

$$|\psi\rangle \equiv \psi^\dagger|G\rangle = \sum_i \varphi_i \tilde{c}_{i\sigma}^\dagger|G\rangle, \quad (5.25)$$

with

$$\varphi_i = A e^{-(x_i-x_0)^2/2\Delta_x} e^{ik_0x_i}, \quad (5.26)$$

where  $\tilde{c}_{i\sigma}^\dagger$  is the creation operator (in real space) projected onto the space of non-double occupancy.  $A$  is just a constant which is fixed by normalizing  $|\psi\rangle$ .  $|\psi\rangle$  belongs to the subspace with  $N+1$  particles.

To evolve in real time we just apply the evolution operator

$$|\psi(\tau)\rangle = e^{-iH\tau}|\psi\rangle. \quad (5.27)$$

In order to visualize the evolution in real time we measure the spin and charge density relative to the ground state as a function of time  $\tau$ ,

$$\rho_\alpha(x, \tau) \equiv \langle\psi(\tau)|n_{i\alpha}|\psi(\tau)\rangle - \langle G|n_{i\alpha}|G\rangle, \quad (5.28)$$

where  $\alpha = c, s$ ,  $n_{ic} = n_{i\uparrow} + n_{i\downarrow}$ ,  $n_{is} = n_{i\uparrow} - n_{i\downarrow}$ , and  $x = x_i$ . Here  $n_{i\alpha}$  are electronic density operators. We chose energy units such that the hopping constant  $t = 1$ . Most of the numerical results were carried out using the following parameters:  $L = 160$  lattice sites, 600 DMRG vectors (this translates into errors of the order of  $10^{-4}$  in the spin and charge density up to times of  $50t$ ) and  $\Delta_x = 5$  lattice sites (which corresponds to a width  $\Delta_k \sim 0.06\pi$  in momentum space).

### 5.2.1 Validation of our t-DMRG code

Before presenting our main results for the  $t$ - $J$  model, let us start by considering some exact cases that we can use to compare and to validate our computational code. The first case is that of non-interacting spinless fermions in a lattice described by the Hamiltonian

$$H = -t \sum_{i=1}^{L-1} \left( c_i^\dagger c_{i+1} + \text{h.c.} \right), \quad (5.29)$$

where  $c_i^\dagger$ ,  $c_i$  are canonical fermionic operators and we use open boundary conditions. In Fig. 5.3 we show our main results.

The wavepacket propagates ballistically with constant velocity (see Fig. 5.3(b)), as it is expected for a non-interacting system. Note from Fig. 5.3(a) that the only effect of the band curvature is to increase the width of the wavepacket with time and no splitting of the wavepacket is observed. In order to have a quantitative comparison with the exact result, we recall the exact expression of the dispersion relation (energy band) given by

$$\epsilon(k) = -2t \cos(ka), \quad (5.30)$$

where  $a$  is the lattice constant (that we set to  $a = 1$ ). The group velocity  $v_g$  is just given by the derivative of Eq. (5.30) with respect to  $k$ ,

$$v_g(k) = 2ta \sin(ka). \quad (5.31)$$

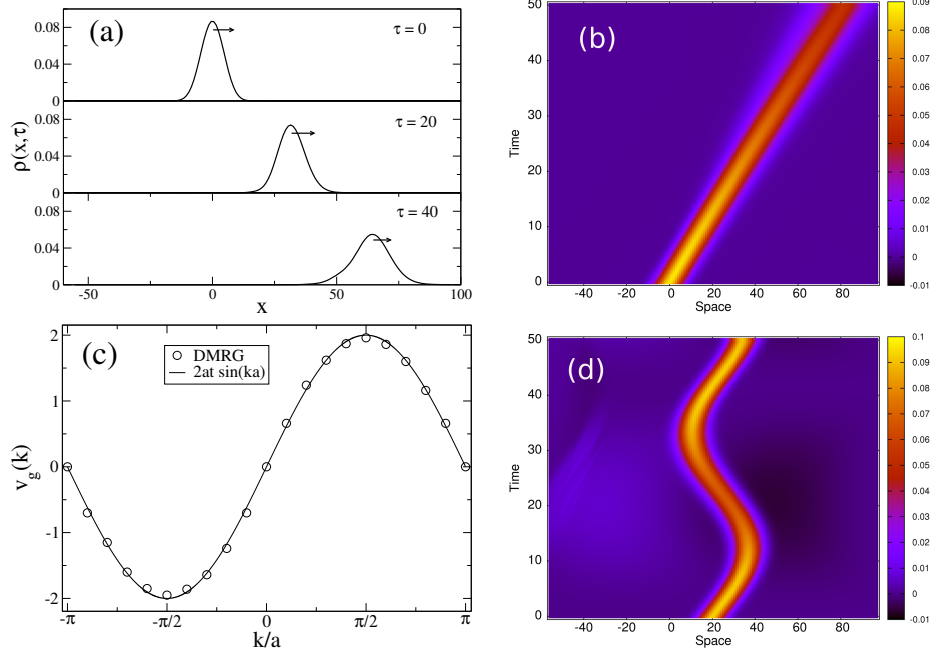


Figure 5.3: Non-interacting spinless fermions for  $L = 160$ . (a): Charge density relative to the ground state for  $n = 0.6$ ,  $k = 0.7\pi$  for different times  $\tau$ . Note that the only effect of the band curvature is to increase the width of the wavepacket with time. (b): as in (a) but here the charge density is represented by the color scale. We observe a ballistic propagation with constant velocity. (c): group velocity as a function of  $k$  measured using wavepackets with  $k > k_F$ . Our DMRG results are in very good agreement with the exact solution. (d): as in (b) but for  $E = 0.15$  (linear potential),  $L = 160$ ,  $n = 1/L$  and  $k = 0.6\pi$ . Contrary to the classically expected constant acceleration the motion of the electron is oscillatory (Bloch oscillations).

By measuring the position of the maximum of the wavepacket we can determine the group velocity from our simulations and compare with the exact result (5.31). In Fig. 5.3(c) we in fact observe that our DMRG results are in very good agreement with the exact solution. It is important to remark that the measurements of these group velocities were done using wavepackets with momentum  $k > k_F$  (with  $k_F = \pi n$ ) and with a width in momentum space such that there is no overlap with the Fermi sea, otherwise some components of the wavepacket would be annihilated.

It is interesting to add a linear potential (constant electric field) of the form  $E \sum_i x_i c_i^\dagger c_i$  to see if we can observe the theoretically predicted Bloch oscillations [68, 69]. In Fig. 5.3(d) we observe such a oscillations with a period of  $\sim 42$  (in units of  $1/t$ ) which is consistent with the exact value given by  $2\pi/E$ . The Bloch oscillations are due to the fact that the dispersion relation corresponds to a band bounded in energy (Eq. (5.30)) that is a harmonic function (in this case, a cosine function). Since all possible momenta are equivalent to those restricted to the first Brillouin zone, and given that the velocity of the electron changes with respect to  $k$  according to Eq. (5.31), the linear increase (or decrease) of the momentum  $k$ , as a consequence of the electric field, generates the oscillations in the velocity and position. Note that, while for a free electron in continuous space and under the action of a constant electric field a constant acceleration is expected, for an electron in a lattice the motion is oscillatory. This is a pure quantum mechanical result that has been experimentally observed, for example, in ultra-cold atoms in optical lattices [70] and in semiconductor superlattices [71].

As a second test we consider two limiting cases of the  $t$ - $J$  model. The first case corresponds to the low density limit at the supersymmetric point ( $J = 2t$ ) which is equivalent to free electrons [8]. This is consistent with Fig. 5.4(a) where no additional splitting of the wavepacket is observed and the spin and charge velocities are the same, i.e. there is no spin-charge separation. The second case corresponds to the limit  $J \rightarrow 0$  which is equivalent to the strong repulsive Hubbard model. It is well known that complete spin-charge separation is present at all energies for the Hubbard model [9,10] (this is possible because the exact wavefunction of the Bethe-Ansatz can be factorized into two independent parts, charge and spin, respectively). We can observe in Fig. 5.4(b) that the spin and charge densities are completely decouple from each other which is in agreement with the Hubbard model. As we will see later the left-propagating wavepacket is just a low energy effect described by the LL theory. Therefore we conclude that all these successful tests are a good indication that our

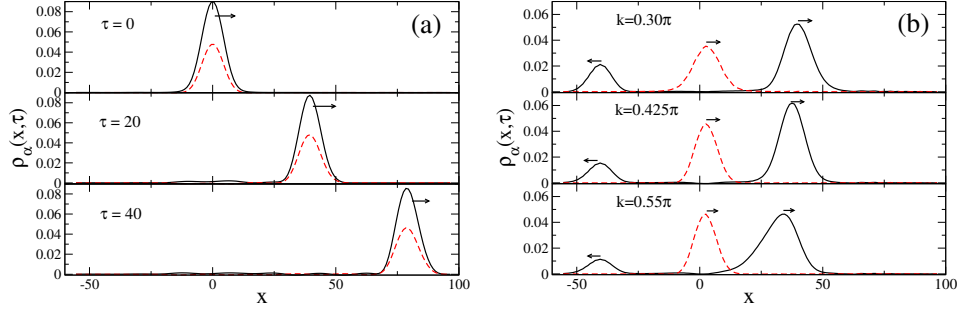


Figure 5.4: Charge (black-full line) and the spin (red-dashed line) densities given by Eq. (5.28). (a): Low density limit exemplified using the parameters  $J = 2t$ ,  $n = 0.1$  and  $k = 0.5\pi$  for different times. (b):  $J = 0.1$ ,  $n = 0.5$  for different  $k$  at  $\tau = 20$ . This picture is consistent with the  $J \rightarrow 0$  limit (strong repulsive Hubbard model).

$t$ -DMRG code produces reliable results.

### 5.2.2 Supersymmetric point $J = 2$

In order to compare the results of our simulations with the one-electron spectral lines we consider first the supersymmetric (SUSY) point  $J = 2$  where we know the exact solution previously explained in the first section of this chapter.

#### Low-energy results

As we have already explained in Sec. 2.6, for a LL with spin rotational invariance a right-propagating electron injected to the chain splits into three different objects: two counter-propagating objects carrying only charge given by the fraction  $Q = (1 \pm K)/2$  (where  $K$  is the so called Luttinger parameter and  $\pm$  stands for right and left propagation, respectively), and one right-propagating object carrying only spin (called spinon) and, in general, with different velocity of the charge objects (spin-charge separation). In Fig. 5.5 we show the real-time dynamics of the right-propagating wavepacket injected to the chain at  $\tau = 0$  with physical momentum close to  $k_F$  and for two different electronic densities. Note that consistently with the LL theory we also observe the above-mentioned three different wavepackets. However, in both cases we observe that the spin mode also carries a fraction of charge which is more visible for  $n = 0.6$ . This is due to the fact that the injected wavepacket has a finite width  $\Delta k$  in momentum space making difficult to reach the perfect low-energy limit  $k = k_F$  and therefore there are still small but visible high energy contributions. We

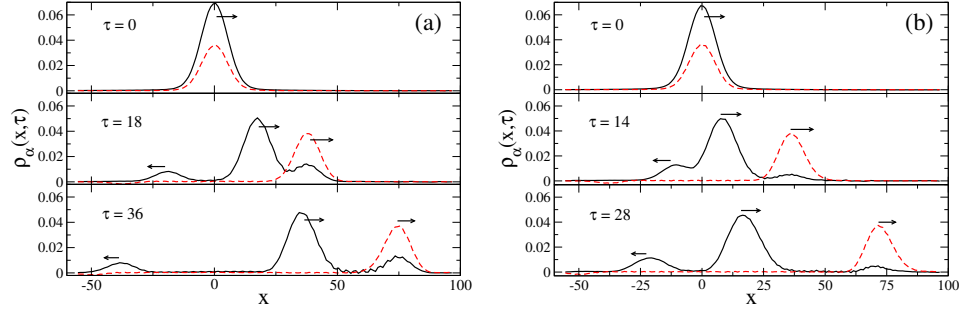


Figure 5.5: Charge (black-full line) and spin (red-dashed line) densities given by Eq. (5.28) at different times. (a):  $n = 0.6$  and  $k = 0.35\pi$ . (b):  $n = 0.8$  and  $k = 0.45\pi$ . The arrows signal the direction of motion of each wavepacket.

know from the exact solution [36] that in the low density limit  $n \rightarrow 0$  the SUSY  $t$ - $J$  model is a gas of free fermions and in the high density limit  $n \rightarrow 1$  it is the Heisenberg model; in the first case there is no spin-charge separation, while in the second case there is complete separation of these degrees of freedom. Therefore it is expected that while decreasing the density a tendency to electron recombination can be observed. This is the reason why the fraction of charge carried by the spin mode is more visible at  $n = 0.6$  than at  $n = 0.8$ . In principle, this charge should completely vanish at  $k = k_F$  and  $\Delta k \rightarrow 0$  (i.e. for a more extended wavepacket in real space) but a numerical test of this fact demands an increase in the system size which goes beyond our computational capabilities and a decrease of the system size that makes not possible the resolution of the wavepackets. If we measure the amount of charge of the left propagating wavepacket and we use  $Q = (1 \pm K)/2$  to extract the LL parameter  $K$ , we obtain  $K \sim 0.8$  for  $n = 0.6$  and  $K \sim 0.7$  for  $n = 0.8$  which are in good agreement with the parameters obtained in Sec. 4.1.

### High-energy results

In the previous section we have observed that our numerical simulations near the Fermi momentum are consistent with the facts predicted by the Luttinger Liquid theory. In this section we investigate what occurs for momenta higher than  $k_F$ . In Figs. 5.6 and 5.7 we show our high-energy results for

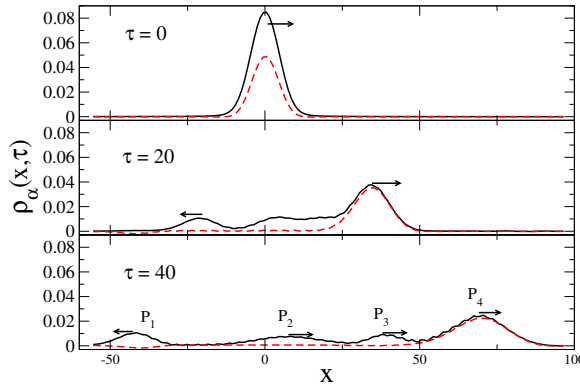


Figure 5.6: Charge (black-full line) and the spin (red-dashed line) densities given by Eq. (5.28) at different times for  $n = 0.6$  and  $k = 0.70\pi$ .

$n = 0.6$  and  $k = 0.70\pi$ . In Fig. 5.6 both charge and spin densities are plotted at three different times.

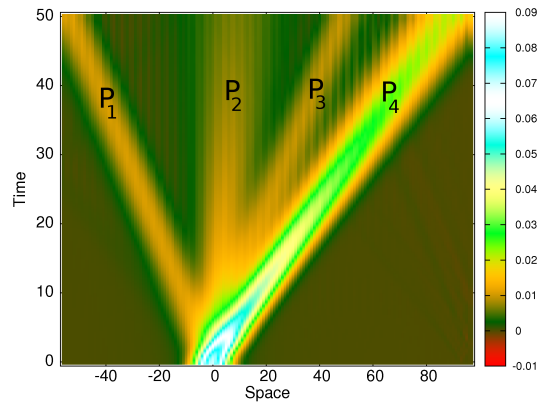


Figure 5.7: Charge density (color scale) as function of time and space for  $n = 0.6$  and  $k = 0.70\pi$ . We clearly observe the ballistic transport of the different wavepackets meaning that they are excited eigenmodes of the system.

In Fig. 5.7 only the charge density (color scale) as function of space and time is plotted. We clearly identify in the charge degree of freedom four different wavepackets  $P_i$  which propagate ballistically (see Fig. 5.7), meaning that they are excited eigenmodes of the model under consideration. In contrast to the low-energy case, a deviation from the LL theory can be seen in Fig. 5.6, where now the right propagating wavepacket is split into three new parts  $P_2$ ,  $P_3$  and  $P_4$ . In order to understand this splitting we plot in Fig. 5.8 the derivative  $v(k) = \partial\omega(k)/\partial k$  of the spectral lines of Fig. 5.2 and the velocities of the different wavepackets identified in Fig. 5.7: triangles ( $P_1$ ), diamonds ( $P_2$ ), squares ( $P_3$ ) and circles ( $P_4$ ).

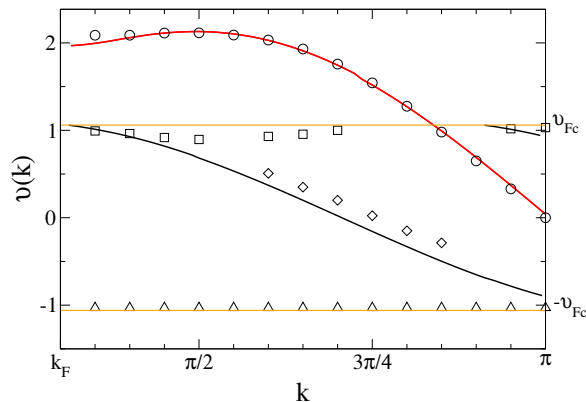


Figure 5.8: Derivative  $v(k) = \partial\omega(k)/\partial k$  of the Bethe-Ansatz spectral lines of Fig. 5.2. We also plot the velocities of the different wavepackets identified in Fig. 5.7: triangles ( $P_1$ ), diamonds ( $P_2$ ), squares ( $P_3$ ) and circles ( $P_4$ ). The orange horizontal lines stand for the Fermi velocity  $v_{Fc} = \partial\epsilon_c(q_{Fc})/\partial q$  given by the Bethe-Ansatz solution.

The velocity of each  $P_i$  is extracted by measuring the position of the maximum of the wavepacket at the most convenient time, i.e. at that time where we can resolve  $P_i$  and where the spreading of one wavepacket does not destroy the other wavepackets. This is not always the case for the  $P_2$  and  $P_3$  wavepackets and for this reason there are less squares and diamonds than circles in Fig. 5.8. The orange horizontal lines stand for the Fermi velocity  $v_{Fc} = \partial\epsilon_c(q_{Fc})/\partial q$  given by the Bethe-Ansatz solution.

At  $J = 2t$ , we know from the Bethe-Ansatz that only two different kinds of particles are involved in any excitation: the  $c$  and  $s$  pseudoparticles. As we explained before, what we called  $s$  lines (red lines in Figs. 5.2 and 5.8) involve one  $c$  hole with fixed momentum  $q_{Fc}$  and one  $s$  hole with momentum  $q_s$  determined in terms of  $k$  by  $q_s = \pm 2k_F - q_{Fc} - k$ . As it is explained in the appendix B.1.2, in the case of spectral line with significant spectral weight we observe a wavepacket propagating with velocity  $v_s(q_s(k)) = \partial \epsilon_s(q_s(k))/\partial q_s$  that according to Eq. (5.24) is equal to  $\partial \omega(k)/\partial k$ . This is the reason why the velocity of the wavepacket  $P_4$  (circles) is in very good agreement with the  $s$  line (red line) in Fig. 5.8 and it can be associated with the  $s$  pseudoparticle. Using the same argument for the  $c$  line, we can associate the wavepacket  $P_2$  (diamonds) with the  $c$  pseudoparticle.

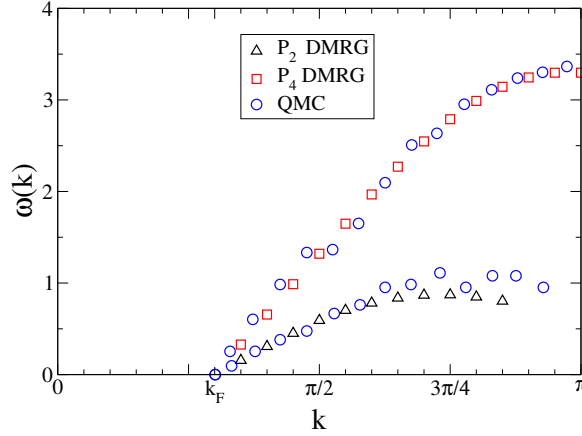


Figure 5.9: Locus of the highest weight features of the electron addition part of the spectral function of the  $t$ - $J$  model from quantum Monte Carlo results [58] and the energies obtained by integrating the velocities of the wavepackets  $P_2$  and  $P_4$ .

In Fig. 5.9 we show a comparison of the dispersion relations obtained from quantum Monte Carlo (QMC) simulations for the one-dimensional  $t$ - $J$  model [58] and that obtained from t-DMRG by integrating the velocities of the wavepacket  $P_2$  and  $P_4$  between  $k_F$  and  $k$  with the zero of energy at  $k_F$ . While the dispersions obtained in QMC simulations can be well reproduced by the velocities obtained from these wavepackets from t-DMRG (in spite of the discretization errors in integrating the velocities and the uncertainties from the analytic continuation in QMC), no direct access to the wavepackets  $P_1$  and  $P_3$  is possible from the spectral function. However, according to the PDT theory [60, 65–67], there is finite and significant spectral weight above the  $s$  line due to excitations involving low-energy pseudo particle-holes in the  $c$  band, in addition to the removal of the one pseudoparticle at  $q = q_{Fc}$  generated after the addition of the electron. Since these excitations in the  $c$  band are low-energy excitations, we can use the LL theory [2] to explain the low-energy modes of the system. This would explained the appearance of the wavepackets  $P_1$  and  $P_3$  for  $k > k_F$ .

If we use the same analysis but for the case of the  $c$  line, where now we would have particle-holes in the  $s$  band, we could argue that two counter-propagating wavepackets with velocities  $\pm v_{Fs}$  should be also visible (Note from Fig. 5.1 that the  $s$  band is not flat and therefore we can still linearize as in the LL theory). In fact, in Fig. 5.6 below the wavepacket  $P_1$  we observe a small valley in the spin density propagating with velocity  $-v_{Fs}$ . However, according to the LL theory [2] this valley should not be present because for a system with spin rotational invariance  $K_\sigma = 1$  (LL parameter for the spin degree of freedom) and therefore  $Q_{\sigma,-} = (1 - K_\sigma)/2 = 0$  (see Eq. (2.35)). This can also be explained from the fact that at zero magnetization the  $s$  band is completely full and there is no space for particle-hole creation. The presence of this valley in the spin density indicates that

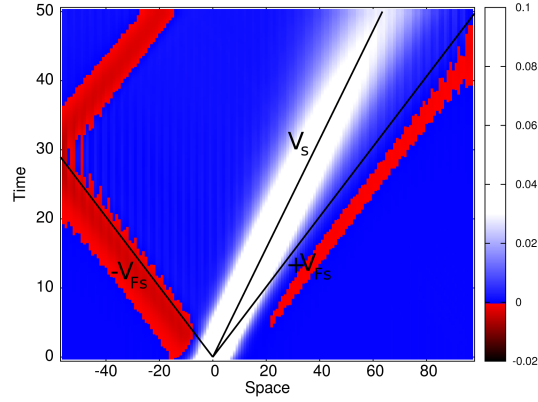


Figure 5.10: Time evolution of  $\rho_s(x_i, \tau)$  for a wavepacket initially at  $x = 0$ , with momentum  $k = 0.8\pi$ , at density  $n = 0.6$ , and  $J = 2t$ . The depressions in spin density (red) have a slope in a time-space diagram corresponding to the Fermi velocity  $v_{Fs}$  of  $\epsilon_s$ .  $v_s$  denotes the velocity of the wavepacket  $P_4$  similar to Fig. 5.6, that contains most of the spin density.

$K_\sigma \gtrsim 1$ . A more clear picture of this situation is shown in Fig. 5.10. Previous studies [72], [73], [74] claim that this is just a finite size effect that vanishes logarithmically with the system size.

To close this section let us consider another important effect that we observe at high energy concerning the charge carried by the spin mode. As we observe in Fig. 5.11(a) the amount of this charge increases with the momenta  $k$ . In a more quantitative manner, we measure in Fig. 5.11(b) the charge of the different wavepackets  $P_i$  as a function  $k$ . Note that the total charge  $Q_{total}$  is conserved. Due to the overlap between  $P_2$  and  $P_3$  we could compute only the sum of their charges  $Q_{P_2} + Q_{P_3}$ . The charge  $Q_{P_1}$  of the left propagating wavepacket is almost constant and it is consistent with the low energy results explained in the previous section. We observe that by increasing  $k$  the charge  $Q_{P_2} + Q_{P_3}$  decreases, while the charge  $Q_{P_4}$  carried by the spin mode increases. We interpret this as a tendency to electron recombination at high energies. However, this recombination is not total because there is still a fraction of charge going to the left without accompanying spin.

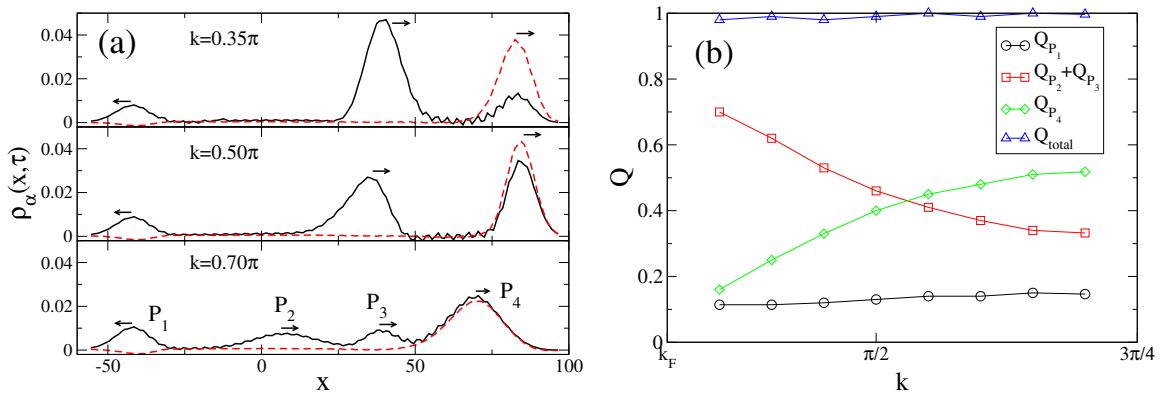


Figure 5.11: (a): Charge (black-full line) and the spin (red-dashed line) densities given by Eq. (5.28) for  $J = 2t$ ,  $n = 0.6$ , at time  $\tau = 40$ , for different values of the momentum  $k$  of the injected fermion. (b): Charge  $Q$  of the different wavepackets  $P_i$  as a function of  $k$ . Due to the overlap between  $P_2$  and  $P_3$  we could compute only the sum of their charges  $Q_{P_2} + Q_{P_3}$ .

### 5.2.3 Away from the supersymmetric point $J = 2$

The results of the previous sections show the existence of two different quasiparticles that were also predicted by the Bethe-Ansatz solution at the integrable point  $J = 2$ . The question arises whether these two modes are still visible out of the integrable point. In Fig. 5.12 we show different cases where the same features present at  $J = 2$  are also observed. In Fig. 5.13 we measure the group velocity of each wavepacket. As in the SUSY case, we observe that different modes follow a similar behavior as that predicted by the Bethe-Ansatz results (full lines) with the difference that the velocities are slightly modified. Since the coupling constant  $J$  favors the formation of nearest neighboring singlet-electron pairs, and since for  $J = 0$  the spin band is completely flat (because the ground state is degenerate in the spin degrees of freedom), it is expected that by increasing  $J$  the velocity of the spin mode increases, while the velocity for the charge modes decreases. This is also observed in Fig. 5.13 where for  $J < 2$  ( $> 2$ ) most of the charge modes (triangles and squares) have a larger (smaller) velocity in comparison to those of the  $J = 2$ . We cannot conclude the same for the charge mode given by the diamonds because the velocity of this latter is more difficult to determine due to the overlapping with the other wavepacket. The opposite occurs for the spin mode (circles), i.e. for  $J < 2$  ( $> 2$ ) this has a larger (smaller) velocity in comparison to those of the  $J = 2$ .

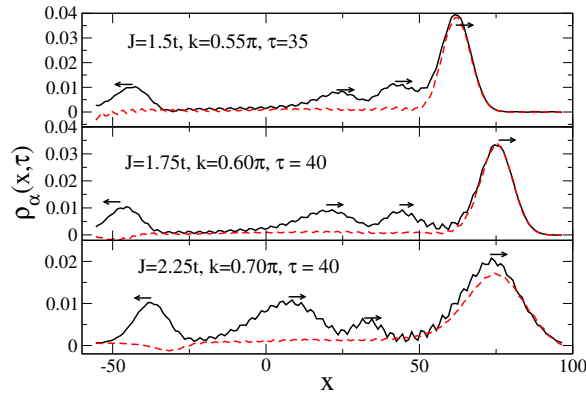


Figure 5.12: Fractionalized wavepackets for different values of  $J/t$  away from the SUSY point, at a density  $n = 0.6$ . As in the SUSY case, charge fractionalizes into four pieces, while spin does not, and carries an appreciable amount of charge.

In the previous cases, that is near the SUSY point, the spin velocity  $v_s$  is larger than the charge velocity  $v_c$ . By decreasing  $J$  we expect a regime where  $v_s$  is smaller than  $v_c$ . In Fig. 5.14 one example of the dynamics in this regime is shown corresponding to  $J = 1.0$  and  $n = 0.5$ . For  $k = 0.3\pi$  (close to  $k_F$ ) the usual low energy spin-charge separation is observed with  $v_s < v_c$  in this case. By increasing  $k$  (and therefore the energy of the pseudoparticles), we observe that the right propagating spin mode starts to fractionalize into two parts, one carrying almost no charge and another co-moving with the charge mode. By increasing even more  $k$  the low-energy spin mode disappears almost completely and there is only spin co-moving with the charge mode. As in the SUSY point, we interpret this as tendency to electron recombination. We have observed a similar behavior at the SUSY point where the spin mode increases its charge by increasing  $k$ . In other words, for  $J = 2.0$  the fastest mode is the  $s$  pseudoparticle while for  $J = 1.0$  the fastest mode is the  $c$  pseudoparticle. Hence the fastest pseudoparticle, i.e. that with highest energy, has the tendency to recombine into an electron. However, this recombination is not total because still a fraction of charge goes to the left without accompanying spin.

Summarizing we have observed by means of our numerical simulations of the real-time evolution of

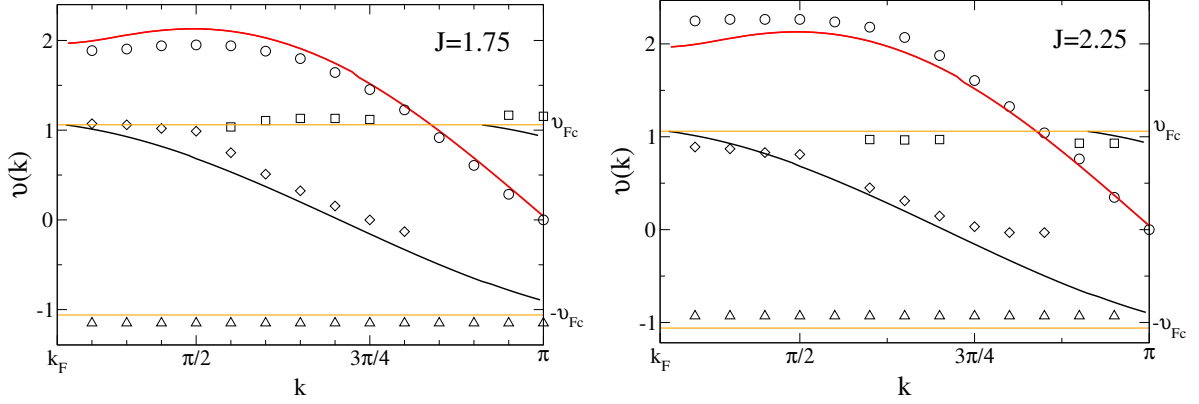


Figure 5.13: As in Fig. 5.8 but for  $J = 1.75$  and  $J = 2.25$ . The full lines still correspond to the Bethe-Ansatz results for the SUSY point  $J = 2.0$ .

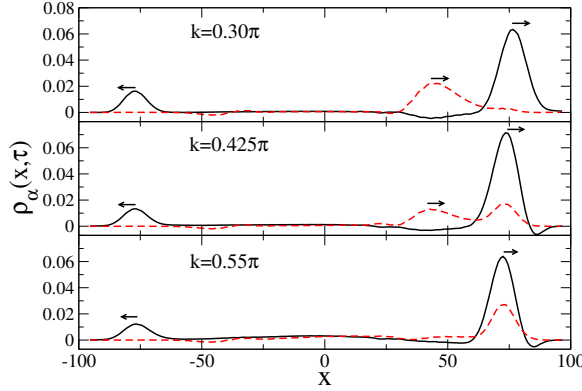


Figure 5.14: Fractionalized wavepackets at  $J/t = 1$ ,  $n = 0.5$ ,  $\tau = 50$  and  $L = 200$ . In this case, where  $v_s < v_c$ , fractionalization of the spin density is observed at higher energies ( $k = 0.425\pi$ ).

an electron injected into a  $t$ - $J$  one-dimensional chain that at low energies our results are consistent with the Luttinger Liquid theory which predicts complete spin-charge separation and charge fractionalization into two chiral modes. At high energies we observe new degrees of spin and charge fractionalization that can be interpreted in terms of the  $c$  and  $s$  pseudoparticle described by the Bethe-Ansatz even away of the integrable point  $J = 2$ . We also observe that by increasing the momenta  $k$  of the injected electron the fastest pseudoparticle starts to take on more charge or spin in order to try to recombine into an electron. Before closing this chapter it is important to remark that all the new fractionalization of the wavepacket observed in the  $t$ - $J$  model are neither an effect of the band curvature nor of the forbidden double occupancy, as we have already shown in Figs. 5.3(a) and 5.4(b), respectively.



## Chapter 6

# Summary and Conclusions

The most important result of this work is the observation of evidences of new kinds of spin a charge fractionalization in one-dimensional systems by means of time-dependent DMRG (Density Matrix Renormalization Group) numerical simulations that go beyond the well known Luttinger Liquid (LL) paradigm [3].

In order to understand the novelties of our results that differ from the well established LL characteristics, we have dedicated Ch. 2 to a brief explanation of this theory. In few words, the LL theory describes the low energy physics of any one-dimensional system. We can name some of its important features: the excitations consist of bosonic modes of charge and spin, both with a linear dispersion and propagating with different velocities (spin-charge separation); the long-distance behavior of all correlations is described by an anomalous exponent (i.e. there are additional contributions to the exponents calculated using mean-field theory) which depends only on two parameters,  $K_\rho$  and  $K_\sigma$ , the first one for the charge and the second one for the spin, respectively, also called Luttinger parameters, which can determine the different phases of a 1D system like charge density wave (CDW), spin density wave (SDW), singlet superconductivity (SS) and triplet superconductivity (TS); chiral separation which states that an electron injected to the 1D chain can be split into counter-propagating modes,  $\pm$ , with charges and spin given by  $Q_{\rho,\pm} = (1 \pm K_\rho)/2$  and  $Q_{\sigma,\pm} = (1 \pm K_\sigma)/2$ , respectively.

The LL theory is valid only in the low energy limit. It can be derived by considering a linearized dispersion and low energy excitations around the Fermi points. In order to investigate 1D systems in a wider range of energies, we have used the DMRG algorithm explained in Ch. 3. The DMRG method is just a very efficient way of reducing the Hilbert space such that important physical quantities can be still computed with very high precision for larger system sizes in comparison to exact diagonalization or the Lanczos method [31]. The criteria for the truncation of the Hilbert space is based on the eigenvectors and eigenvalues of the so called reduced density matrix. In Ch. 3 we have presented the most important technicalities concerning the static DMRG and the time-dependent DMRG (also denoted as t-DMRG), in order to give the reader a flavor of all the effort involved around this method.

In Ch. 4 we used the static DMRG in order to investigate the ground-state properties of the 1D  $t$ - $J$  model [33]. The main new contribution to this issue is the direct measurement of a finite spin gap in a appreciable region of the phase diagram giving indications of the existence of preformed pairs in the  $t$ - $J$  model. Preformed pairs is an important and currently debated issue, because it is one of the suggested mechanism to explain the pseudogap phase present in high- $T_c$  superconductors. Our results show that the formation of these pairs is visible in the real-space density. A finite spin gap

might also have important experimental implications in the sense that the preformed pairs could be experimentally realized at low but finite temperatures by means of, e.g, cold atoms in optical lattices. Our determination of the spin gap have also solved a controversy posed by previous studies [27–29] concerning the size of this phase. We have also re-determined the phase diagram, firstly obtained by Ogata et al [32], containing four different phases: a metallic phase (M) or repulsive LL, a gapless superconducting (SC) region, a singlet-superconducting phase with spin gap (SG + SS), and phase-separation (PS), where the system separates into a hole-rich and an electron-rich part. These phases were obtained by means of energy and correlation measurements after extrapolating to the thermodynamic limit, using system sizes of the order of 200, which means a significant improvement in the determination of the phase diagram in comparison to Ogata’s diagram with a maximum of 16 lattice sites. Finally, we have obtained an approximate boundary for an additional phase, proposed by Chen and Moukouri [34], called electron solid, where all electrons collapse into a single antiferromagnetic island described by the Heisenberg model.

The main results of our work are presented in Ch. 5 where we show evidences of new types of charge and spin fractionalization that are not described by the LL theory. Our t-DMRG simulations consist of the real-time evolution of one right-propagating electron with spin up and momentum  $k$  injected to  $t$ - $J$  chain in the form of a gaussian wavepacket. Since the model under consideration is an 1D interacting system, where electron are not anymore well defined quasiparticles, a splitting of an initial wavepacket into different coherent and incoherent parts is expected. Fortunately, in our simulation of the  $t$ - $J$  model the incoherent parts, if there is any, are not visible. This fact has allowed us to investigate the phenomenon of fractionalization and elementary excitation in this model. For  $k \sim k_F$ , i.e. at low energies, our results are consistent with those predicted by the LL theory where we observe chiral fractionalization of the charge into two counter-propagating wavepackets while the spin does not fractionalize due to the spin rotational invariance. For  $k > k_F$ , i.e. at high energies, additional wavepackets to those predicted by the LL theory are observed. In order to understand the origin of these modes we have used the exact Bethe-Ansatz solution at the supersymmetric (SUSY) point  $J = 2t$ , whose excitations are described in terms of two different pseudofermions, the  $c$  and  $s$  pseudoparticles, respectively. Each of these pseudoparticles has its own dispersion relation and pseudo Fermi sea and therefore any excitation is generated by addition and/or removal of these pseudoparticles. Two main spectral lines of the one-particle spectral function result from this picture: one  $c$  branch, generated by one  $s$  hole with momentum fixed at the Fermi surface of the  $s$  band, and one  $c$  hole with arbitrary momentum; and one  $s$  branch, generated by one  $c$  hole with momentum fixed at its Fermi surface and one  $s$  hole with arbitrary momentum. The derivative of these spectral lines corresponds to the group velocity  $v_\alpha$  (with  $\alpha = c, s$ ) of pseudoparticles that we can in fact identify in our simulations (see  $P_2$  and  $P_4$  in Figs. 5.7 and 5.8). There are additional modes that cannot be directly associated with the slope of these spectral lines and that move with the pseudo Fermi velocity ( $P_1$  and  $P_3$ ). However, we know from the PDT theory [60, 65–67] that there is finite spectral weight above the spectral lines due to low-energy pseudo particle-holes excitations and the two pseudoholes at their Fermi surface. Since they are low-energy excitations, the LL theory [2] can explain the presence of these additional modes even for  $k > k_F$ .

The analysis in terms of pseudoparticles is in principle valid at the SUSY point. However, similar features are observed going away from the SUSY point, inside the regime where  $v_s > v_c$  (see Figs. 5.12 and 5.13). These results might indicate that this picture of pseudoparticle could serve as starting point for the development of a general framework of 1D interacting systems at all energies. In the vicinity of the SUSY point,  $J = 2$ , we have that the velocity  $v_s$  of the  $s$  pseudoparticle is larger than the velocity  $v_c$  of the  $c$  pseudoparticle and we also observe that the  $s$  pseudoparticle carries not only spin but an appreciable amount of charge which increases with the momentum  $k$

of the injected electron while the  $c$  pseudoparticle carries only charge. By decreasing  $J$  we reach a regime where now  $v_c > v_s$  and the roles of  $c$  and  $s$  seem to be inverted. In that case we observe that the  $c$  pseudoparticle carries charge and an appreciable amount of spin which increases with  $k$ , while the  $s$  pseudoparticle carries almost only spin. In other words, the fastest pseudoparticle is taking on more of its complementary degree of freedom when the energy increases. We interpret this fact as a tendency to electron recombination at high energies, which is not total because there is still an independent fraction of charge traveling with opposite velocity and without carrying spin.

It is important to remark that, in contrast to the spinons and holons of the LL theory, at high energies these pseudoparticles are not necessarily associated with pure charge or pure spin degrees of freedom but they can be composed of a mixture of them, as it is the case of the  $s$  pseudoparticle which carries both spin and charge (see the wavepacket  $P_4$  in Fig. 5.11). This is also an important new result of our work because information about the charge and spin of these pseudoparticles cannot be easily obtained either from the Bethe-Ansatz or from the one-particle spectral function.

Summarizing, from our t-DMRG results at high energies, we can conclude the following facts, which go beyond the LL paradigm: charge fractionalization into more than two pieces; spin fractionalization when  $v_s < v_c$  for a system with spin rotational invariance (i.e.  $K_\sigma = 1$ ); one excitation (wavepacket  $P_4$ ) carrying both charge and spin, indicating that the picture of pure spin-charge separation is not in general valid at high energies.



# Appendices



# Appendix A

## DMRG Method

In this appendix we develop in more details some feature of the DMRG algorithm. In the first section we present a proof that the eigenvectors of the reduced density matrix with the largest eigenvalues is the basis that optimizes the truncated state. In the second section we show, using the singular value decomposition (SVD), that the truncated state can be written in terms of the eigenvectors of the reduced density matrix of each part, such that one can realize the upper bound of the entanglement between both parts.

### A.1 Optimization of the wave function

These calculations were originally presented in the reference [13]. Let us start remembering Eq. (3.1),

$$|\psi\rangle = \sum_i^{d_F} \sum_j^{d_R} \psi_{ij} |i\rangle |j\rangle, \quad (\text{A.1})$$

where  $d_F$  ( $d_R$ ) is the dimension of the left (right) subspace and  $\psi_{ij}$  are complex coefficients. In order to reduce the Hilbert space of the problem we start defining a truncated state

$$|\tilde{\psi}\rangle = \sum_{\alpha}^m \sum_j^{d_R} a_{\alpha j} |\alpha\rangle |j\rangle, \quad (\text{A.2})$$

with  $m \leq d_F$  and the vectors  $|\alpha\rangle = \sum_i u_{\alpha i} |i\rangle$  come from a change of basis in the left part. Our purpose is to find a new basis  $|\alpha\rangle$  that produces a truncated state (A.2) which is the best representation of the exact state  $|\psi\rangle$ . For this reason the state  $|\psi\rangle$  is denoted as the target state. In more quantitative words, we have to find  $|\alpha\rangle$  such that the distance  $\| |\tilde{\psi}\rangle - |\psi\rangle \|$  is minimum. This problem can be solved using the singular value decomposition (SVD), as it was done originally by White [42]. However, here we will consider the solution by Schollwöck [13] and the SVD will be taken into account only in the next section. For simplicity let us assume real coefficients  $a_{\alpha j}$ . We have to minimize

$$\| |\tilde{\psi}\rangle - |\psi\rangle \|^2 = 1 - 2 \sum_{\alpha i j} \psi_{ij} a_{\alpha j} u_{\alpha i} + \sum_{\alpha j} a_{\alpha j}^2 \quad (\text{A.3})$$

with respect to  $a_{\alpha j}$  and  $u_{\alpha i}$ . By taking the partial derivative of Eq. (A.3) with respect to  $a_{\alpha j}$  and

equalizing this to zero (stationary condition in  $a_{\alpha j}$ ), we obtain that

$$\sum_i \psi_{ij} u_{\alpha i} = a_{\alpha j}. \quad (\text{A.4})$$

By substituting this last equation into Eq. (A.3), we find that

$$\| |\tilde{\psi}\rangle - |\psi\rangle \|^2 = 1 - \sum_{\alpha i i'} u_{\alpha i} \rho_{i i'} u_{\alpha i'}, \quad (\text{A.5})$$

where we have defined the matrix elements  $\rho_{i i'}$  of the reduced density as

$$\rho_{i i'} = \sum_j \psi_{ij} \psi_{i'j}. \quad (\text{A.6})$$

The last sum in Eq. (A.5) can be written in the eigenbasis of  $\rho$  and then the norm (A.5) becomes

$$\| |\tilde{\psi}\rangle - |\psi\rangle \|^2 = 1 - \sum_{\alpha=1}^m \nu_{\alpha}^2, \quad (\text{A.7})$$

where  $\nu_i$  are the eigenvalues of  $\rho$ . Therefore, the distance (A.7) between the truncated and the exact state is minimized by choosing the  $m$  eigenvectors of  $\rho$  with the largest eigenvalues. This is the reason why the eigenvectors of the reduced density matrix is the most effective basis for representing the target state  $|\psi\rangle$ .

## A.2 Optimization of the entanglement

In this section we deal with the question, whether Eq. (A.1) can be rewritten in another basis such that an upper bound for the entanglement between the left and the right parts can be found. These results are also presented in the reference [13]. When we speak of bipartite entanglement we refer to the fact that the wave function cannot be written as a simple product of the left and right part. This is one of the main characteristic features of quantum systems. Let us start by assuming, without losing generality, that  $d_F \geq d_R$ . The coefficients  $\psi_{ij}$  can be considered as matrix of dimension  $(d_F \times d_R)$ . Singular value decomposition (SDV) [75] assures that  $\psi = U D V^T$ , where  $U$  is an orthonormal  $(d_F \times d_R)$ -dimensional matrix,  $D$  is a  $(d_R \times d_R)$ -dimensional diagonal matrix with non-negative elements  $D_{\alpha\alpha} = \sqrt{w_{\alpha}}$  and  $V^T$  is a unitary matrix of dimension  $(d_R \times d_R)$ . Therefore we can write  $\psi = U D V^T$  as

$$|\psi\rangle = \sum_{i=1}^{d_F} \sum_{\alpha=1}^{d_R} \sum_{j=1}^{d_R} U_{i\alpha} \sqrt{w_{\alpha}} V_{\alpha j}^T |i\rangle |j\rangle = \sum_{\alpha=1}^{d_R} \sqrt{w_{\alpha}} \left( \sum_{i=1}^{d_F} U_{i\alpha} |i\rangle \right) \left( \sum_{j=1}^{d_R} V_{\alpha j}^T |j\rangle \right). \quad (\text{A.8})$$

Since the matrices  $U$  and  $V^T$  are orthonormal, the vectors  $|w_{\alpha}^F\rangle = \sum_i U_{i\alpha} |i\rangle$  and  $|w_{\alpha}^R\rangle = \sum_j V_{\alpha j}^T |j\rangle$  form an orthonormal basis of the left and right part, respectively. Hence, we obtain the so called Schmidt decomposition

$$|\psi\rangle = \sum_{\alpha=1}^{N_{\text{Schmidt}}} \sqrt{w_{\alpha}} |w_{\alpha}^F\rangle |w_{\alpha}^R\rangle. \quad (\text{A.9})$$

Note that the number of coefficients was reduced from  $(d_F \times d_R)$  to  $N_{\text{Schmidt}} \leq d_R$ . Relaxing the constraint  $d_F \geq d_R$ , we have that  $N_{\text{Schmidt}} \leq \min(d_F, d_R)$ . If we use Eq. (A.9) to compute the

reduced density matrices  $\rho_{\text{left}} = \text{Tr}_{\text{right}}|\psi\rangle\langle\psi|$  and  $\rho_{\text{right}} = \text{Tr}_{\text{left}}|\psi\rangle\langle\psi|$ , where  $\text{Tr}_{\text{left}}$  traces out the left part, we obtain

$$\rho_{\text{left}} = \sum_{\alpha=1}^{N_{\text{Schmidt}}} w_{\alpha} |w_{\alpha}^F\rangle\langle w_{\alpha}^F|, \quad (\text{A.10})$$

$$\rho_{\text{right}} = \sum_{\alpha=1}^{N_{\text{Schmidt}}} w_{\alpha} |w_{\alpha}^R\rangle\langle w_{\alpha}^R|. \quad (\text{A.11})$$

From these two last equations we deduce that, in fact, the vectors  $|w_{\alpha}^F\rangle$  and  $|w_{\alpha}^R\rangle$  correspond to the eigenvectors of  $\rho_{\text{left}}$  and  $\rho_{\text{right}}$ , respectively, and  $\sqrt{w_{\alpha}}$  corresponds to the eigenvalues. It is interesting to note that even when the left and right parts are different, their corresponding reduced density matrices have the same eigenvalues. We can also note from Eq. (A.9) that the number of non-zero eigenvalues is a measure of the entanglement. In other words, if there is only one eigenvalue different from zero, then we see that  $|\psi\rangle$  is a simple product of the left and right part and no entanglement is present between these two parts; this is not the case when the number of non-zero eigenvalues is larger than one, therefore, there is entanglement.



## Appendix B

# Creating the Gaussian Wavepacket

During our time-dependent simulations the injected electron has the form of a gaussian wavepacket with nearly well defined momentum. In an interacting system this wavepacket might split into other wavepackets. The aim of this appendix is to investigate the different mechanism which might produce such splitting.

To create a gaussian wavepacket state  $|\psi\rangle$  centered at  $x_0$ , width  $\Delta_x$  and with average momentum  $k_0$ , we apply the operator  $\psi^\dagger$  to the ground state  $|G\rangle$ :

$$|\psi\rangle \equiv \psi^\dagger |G\rangle = \sum_i \varphi_i c_i^\dagger |G\rangle$$

with

$$\varphi_i = C e^{-(x_i - x_0)^2 / 2\Delta_x} e^{ik_0 x_i} \quad (\text{B.1})$$

where  $c_i^\dagger$  is the creation operator in real space (for simplicity we consider spinless fermions).  $C$  is just a constant which is fixed by normalizing  $|\psi\rangle$ .

By Fourier transform, we can also obtain the operator  $\psi^\dagger$  in momentum representation:

$$|\psi\rangle \equiv \psi^\dagger |G\rangle = \sum_k \varphi_k c_k^\dagger |G\rangle$$

with

$$\varphi_k = A e^{-(k - k_0)^2 / 2\Delta_k} e^{-ikx_0}, \quad (\text{B.2})$$

where  $A$  is a normalization constant. The relation between the two different widths is  $\Delta_x = 1/\Delta_k$ . In order to visualize the wavepacket we can measure the charge density relative to the ground state,

$$\langle \psi | n_i | \psi \rangle - \langle G | n_i | G \rangle$$

where  $n_i = c_i^\dagger c_i$ .

### B.1 Evolution of the wavepacket

Given the state of the system  $|\psi\rangle$  at time equal zero, the state  $|\psi(t)\rangle$  at a further time  $t$  can be determined by the application of the evolution operator  $e^{-iHt}$ , as follows

$$|\psi(t)\rangle = e^{-iHt} |\psi\rangle.$$

In order to understand the possible mechanism splitting of the wavepacket, we will consider the two following cases:

### B.1.1 The state $c_k^\dagger|G\rangle$ as a linear combination of wavepackets

First, let us assume that  $c_k^\dagger|G\rangle = |\phi_k\rangle$  is an eigenstate with energy  $E_k = E_0 + \epsilon(k)$ .

$$\begin{aligned} \Rightarrow |\psi(t)\rangle &= e^{-iHt}|\psi\rangle = e^{-iHt} \sum_k \varphi_k |\phi_k\rangle \\ &= \sum_k \varphi_k e^{-iE_k t} |\phi_k\rangle = e^{-iE_0 t} \sum_k \varphi_k e^{-i\epsilon(k)t} |\phi_k\rangle, \end{aligned} \quad (\text{B.3})$$

where  $|\psi(t)\rangle$  and  $\varphi_k$  are given in Eq. (B.2). Now let us assume that  $\Delta_k$  is small enough such that we can approximate the dispersion relation  $\epsilon(k) \sim \epsilon(k_0) + v_g k$ , where  $v_g = \partial\epsilon(k)/\partial k$  is the group velocity. Using Eq. (B.2) and this approximation we obtain

$$\begin{aligned} |\psi(t)\rangle &= e^{-iE_0 t} \sum_k \varphi_k e^{-i\epsilon(k)t} |\phi_k\rangle \\ &= e^{-iE_0 t} A \sum_k e^{-(k-k_0)^2/2\Delta_k} e^{-ikx_0} e^{-iv_g k t} e^{-i\epsilon(k_0)t} |\phi_k\rangle \\ &= C \sum_k e^{-(k-k_0)^2/2\Delta_k} e^{-ikx(t)} |\phi_k\rangle, \end{aligned} \quad (\text{B.4})$$

where  $x(t) = x_0 + v_g t$  and we have absorbed all phase factors in the normalization constant  $C$ . Therefore, comparing with Eq. (B.2), Eq. (B.4) corresponds to a wavepacket with position  $x_0 + v_g t$ , i.e. propagating with velocity  $v_g$  and keeping the same width  $\Delta_k$  for all times. Quadratic terms in the dispersion relation would contribute to the change of the width  $\Delta_k$  and as a consequence  $\Delta_x$  would also change with time, as it is in fact the case of non-relativistic fermions.

Now let us assume that  $c_k^\dagger|G\rangle$  is a linear combination of eigenstates,

$$c_k^\dagger|G\rangle = \sum_i A_i |\phi_k^i\rangle,$$

with energies  $E_k^i = E_0 + \epsilon_i(k)$ .

At this point it is important to remark that, since  $c_k^\dagger|G\rangle$  is a state with well defined momentum  $k$ ,  $|\phi_k^i\rangle$  must have the same momentum  $k \forall i$ .

$$\begin{aligned} \Rightarrow |\psi(t)\rangle &= e^{-iHt} \sum_k \varphi_k \sum_i A_i |\phi_k^i\rangle \\ &= \sum_k \varphi_k \sum_i A_i e^{-iHt} |\phi_k^i\rangle \\ &= \sum_k \varphi_k \sum_i A_i e^{-iE_k^i t} |\phi_k^i\rangle \\ &= \sum_i e^{-iE_0 t} A_i \sum_k \varphi_k e^{-i\epsilon_i(k)t} |\phi_k^i\rangle \\ &= \sum_i e^{-iE_0 t} A_i e^{-i\epsilon_i(k_0)t} \sum_k e^{-(k-k_0)^2/2\Delta_k} e^{-ikx_i(t)} |\phi_k^i\rangle \end{aligned} \quad (\text{B.5})$$

where  $x_i(t) = x_0 + v_{gi}t$ , with  $v_{gi} = \partial\epsilon_i(k)/\partial k$  and we have again assumed that  $\Delta_k$  is small enough such that  $\epsilon_i(k) \sim \epsilon_i(k_0) + v_{gi}k$ . Therefore, Eq. (B.5) is just a linear combination of wavepacket states  $|\psi_i(t)\rangle$ ,

$$\Rightarrow |\psi(t)\rangle = \sum_i C_i |\psi_i(t)\rangle$$

with

$$|\psi_i(t)\rangle = \sum_k e^{-(k-k_0)^2/2\Delta_k} e^{-ikx_i(t)} |\phi_k^i\rangle \quad \text{and} \quad C_i = e^{-iE_0 t} A_i e^{-i\epsilon_i(k_0)t}.$$

In the case of the  $t$ - $J$  model, we can see in the one-particle spectral function that the spectral weight is mainly concentrated on two points, one on the  $s$  line and another on the  $c$  line, for a given momentum  $k$ . Then,  $c_k^\dagger|G\rangle$  is a linear combination of mainly two eigenstate and then we should be able to observe at least two different wavepacket during the evolution. However, we will see in the next case that linear combinations is not the only source of splitting and that is the reason why we see more than two wavepackets in our simulations.

### B.1.2 The state $c_k^\dagger|G\rangle$ as a two parametric eigenstate of $H$

Let us assume that all the eigenstates of the Hamiltonian can be written as  $|\psi_c, \psi_s\rangle$ , i.e. as the tensor product of two degrees of freedom  $c$  and  $s$  (this is, in fact, the case of the  $t$ - $J$  model at the supersymmetric point according to the Bethe-Ansatz solution). In general, the state  $c_k^\dagger|G\rangle$  is a linear combination of eigenstates, as we have seen in the previous section. For simplicity, let us consider only one component given by,

$$c_k^\dagger|G\rangle = A(q_c, q_s) |\psi_c, \psi_s\rangle$$

with energy

$$E_k = E_0 + \epsilon_c(q_c) + \epsilon_s(q_s),$$

and momentum conservation relation  $k = q_c + q_s$ .  $A(q_c, q_s)$  is a complex number which depends on  $q_c$  and  $q_s$ .

Then we apply the same recipe as in the previous sections: assuming that  $\Delta_k$  is small enough such that  $\epsilon_\alpha(q_\alpha) \sim \epsilon_\alpha(q_{\alpha 0}) + v_{g\alpha}q_\alpha$  with  $\alpha = c, s$  and  $v_{g\alpha} = \partial\epsilon_\alpha(q_\alpha)/\partial q_\alpha$  we have

$$\begin{aligned} |\psi(t)\rangle &= e^{-iHt} \sum_k \varphi_k A(q_c, q_s) |\psi_c, \psi_s\rangle \\ &= e^{-iE_0 t} \sum_k \varphi_k e^{-i(\epsilon_c(q_c) + \epsilon_s(q_s))t} A(q_c, q_s) |\psi_c, \psi_s\rangle \end{aligned} \quad (\text{B.6})$$

At this point it is not obvious which kind of wavepacket we will observe because all depends on the form of  $A(q_c, q_s)$ . However, we can consider two cases where we can say something.

The first case is to assume that  $A(q_c, q_s)$  is non-zero only on the  $s$  line, that is, where  $q_c$  is constant and  $q_s$  is free to change. Therefore, for a given  $k$  and  $q_c$ , then  $q_s$  is determined by  $q_s = k - q_c$ . Then

$$|\psi(t)\rangle = C \sum_k e^{-(k-k_0)^2/2\Delta_k} e^{-ikx_s(t)} A(q_c, q_s(k)) |\psi_c, \psi_s\rangle \quad (\text{B.7})$$

where  $x_s(t) = x_0 + v_{gs}t$ . All the constant phase factors were absorbed into the constant  $C$ . Hence, in Eq. (B.7) we have a wavepacket propagating with the velocity  $v_{gs}$ .

The second case is just the opposite;  $A(q_c, q_s)$  is non-zero only on the  $c$  line, that is, where  $q_s$  is fixed and  $q_c$  is free to change. This will produce a wavepacket propagating with the velocity  $v_{gc}$ . Therefore, the fact that the system can be separated into two (or more) degrees of freedom would be another possible mechanism of splitting of the initial wavepacket, additional to the above-explained mechanism due to linear combinations.

# Bibliography

- [1] R. B. Laughlin, Phys. Rev. Lett **50**, 1395 (1983).
- [2] K.-V. Pham, M. Gabay, and P. Lederer, Phys. Rev. B **61**, 16397 (2000).
- [3] T. Giamarchi, *Quantum Physics in One Dimension* (Clarendon Press, Oxford, 2004).
- [4] J. G. Bednorz and Z. K. A. Müller, Phys. B **64**, 189 (1986).
- [5] D. J. Klein and W. A. Seitz, Phys. Rev. B **10**, 3217 (1974).
- [6] J. E. Hirsch, Phys. Rev. Lett **54**, 1317 (1985).
- [7] F. C. Zhang and T. M. Rice, Phys. Rev. B **37**, 3759 (1988).
- [8] P. A. Bares, G. Blatter, and M. Ogata, Phys. Rev. B **44**, 130 (1991).
- [9] E. H. Lieb and F. Y. Wu, Phys. Rev. Lett **20**, 1445 (1968).
- [10] F. H. L. Essler, V. E. Korepin, and K. Schoutens, Phys. Rev. Lett **67**, 3848 (1991).
- [11] M. Ogata and H. Shiba, Phys. Rev. B **41**, 2326 (1990).
- [12] S. R. White, Phys. Rev. Lett **69**, 2863 (1992).
- [13] U. Schollwöck, Rev. Mod. Phys. **77**, 259 (2005).
- [14] C. Kim, A. Y. Matsuura, Z.-X. Shen, N. Motoyama, H. Eisaki, S. Uchida, T. Tohyama, and S. Maekawa, Phys. Rev. Lett **77**, 4054 (1996).
- [15] R. Claessen, M. Sing, U. Schwingenschlögl, P. Blaha, M. Dressel, and C. S. Jacobsen, Phys. Rev. Lett **88**, 096402 (2002).
- [16] T. Lorenz, M. Hofmann, M. Gruninger, A. Freimuth, G. S. Uhrig, M. Dumm, and M. Dressel, Nature **418**, 614 (2002).
- [17] H. Steinberg, G. Barak, A. Yacoby, L. N. Pfeiffer, K. W. West, B. I. Halperin, and K. L. Hur, Nature Phys. **4**, 116 (2008).
- [18] G. Barak, H. Steinberg, L. N. Pfeiffer, K. W. West, L. Glazman, F. von Oppen, and A. Yacoby, Nature Phys. **6**, 489 (2010).
- [19] C. Blumenstein, J. Schäfer, S. Mietke, A. Dollinger, M. Lochner, X. Y. Cui, L. Patthey, R. Matzdorf, and R. Claessen, Nature Phys. **7**, 776 (2011).
- [20] H. Moritz, T. Stöferle, M. Köhl, and T. Esslinger, Phys. Rev. Lett **91**, 250402 (2003).

- 
- [21] I. Bloch, *Nature Phys.* **1**, 23 (2005).
- [22] A. Imambekov and L. I. Glazman, *Science* **323**, 228 (2009).
- [23] A. Imambekov and L. I. Glazman, *Phys. Rev. Lett* **102**, 126405 (2009).
- [24] T. L. Schmidt, A. Imambekov, and L. I. Glazman, *Phys. Rev. Lett* **104**, 116403 (2010).
- [25] A. Shashi, L. I. Glazman, J.-S. Caux, and A. Imambekov, *Phys. Rev. B* **84**, 045408 (2011).
- [26] S. R. White and A. E. Feiguin, *Phys. Rev. Lett* **93**, 076401 (2004).
- [27] Y. C. Chen and T. K. Lee, *Phys. Rev. B* **47**, 11548 (1993).
- [28] C. S. Hellberg and E. J. Mele, *Phys. Rev. B* **48**, 646 (1993).
- [29] M. Nakamura, K. Nomura, and A. Kitazawa, *Phys. Rev. Lett* **79**, 3214 (1997).
- [30] U. Schollwöck, *Ann. Phys.* **326**, 96 (2011).
- [31] K. J. Lanczos, *Res. Natl. Bur. Stand* **45**, 225 (1950).
- [32] M. Ogata, M. U. Luchini, S. Sorella, and F. F. Assaad, *Phys. Rev. Lett* **66**, 2388 (1991).
- [33] A. Moreno, A. Muramatsu, and S. R. Manmana, *Phys. Rev. B* **83**, 205113 (2011).
- [34] L. Chen and S. Moukouri, *Phys. Rev. B* **53**, 1866 (1996).
- [35] P. A. Bares and G. Blatter, *Phys. Rev. Lett* **64**, 2567 (1990).
- [36] P. A. Bares, J. M. P. Carmelo, J. Ferrer, and P. Horsch, *Phys. Rev. B* **46**, 14624 (1992).
- [37] L. D. Landau, *Sov. Phys. JEPT* **3**, 920 (1957).
- [38] J. Voit, *Phys. Rev. B* **47**, 6740 (1993).
- [39] O. M. Auslaender, H. Steinberg, A. Yacoby, Y. Tserkovnyak, B. I. Halperin, K. W. Baldwin, L. N. Pfeiffer, and K. W. West, *Science* **308**, 88 (2005).
- [40] F. D. M. Haldane, *Phys. Rev. Lett* **47**, 1840 (1981).
- [41] V. Meden and K. Schühammer, *Phys. Rev. B* **46**, 15753 (1992).
- [42] S. R. White, *Phys. Rev. B* **48**, 10345 (1993).
- [43] J. Eisert, M. Cramer, and M. B. Plenio, *Rev. Mod. Phys* **82**, 277 (2010).
- [44] J. D. Bekenstein, *Phys. Rev. D* **7**, 2333 (1973).
- [45] M. Srednicki, *Phys. Rev. Lett.* **71**, 666 (93).
- [46] C. G. Callan and F. Wilczek, *Phys. Lett. B* **333**, 55 (1994).
- [47] M. B. Plenio, J. Eisert, J. Dreissig, and M. Cramer, *Phys. Rev. Lett* **94**, 060503 (2005).
- [48] G. Vidal, J. I. Latorre, E. Rico, and A. Kitaev, *Phys. Rev. Lett.* **90**, 227902 (2003).
- [49] J. I. Latorre, E. Rico, and G. Vidal, *Quant. Inf. Comp.* **4**, 48 (2004).

- 
- [50] J. K. Cullum and R. A. Willoughby, *Lanczos Algorithms for large symmetric Eigenvalue Computation* (Birkhäuser, Boston, 1985), Vol. II, Programs.
- [51] J. Dukelsky, M. A. Martín-Delgado, T. Nishino, and G. Sierra, *Europhys. Lett* **43**, 457 (1998).
- [52] D. Gobert, C. Kollath, U. Schollwöck, and G. Schütz, *Phys. Rev. E* **71**, 036102 (2005).
- [53] R. T. Clay, A. W. Sandvik, and D. K. Campbell, *Phys. Rev. B* **59**, 4665 (1999).
- [54] S. Ejima, F. Gebhard, and S. Nishimoto, *Europhys. Lett* **70**, 492 (2005).
- [55] H. J. Schulz, *Phys. Rev. Lett* **64**, 2831 (1990).
- [56] N. Kawakami and S.-K. Yang, *Phys. Lett.* **65**, 2309 (1990).
- [57] F. F. Assaad and D. Würtz, *Phys. Rev. B* **44**, 2681 (1991).
- [58] C. Lavallo, M. Arikawa, S. Capponi, F. F. Assaad, and A. Muramatsu, *Phys. Rev. Lett* **90**, 216401 (2003).
- [59] T. Pruschke and H. Shiba, *Phys. Rev. B* **46**, 356 (1992).
- [60] J. M. P. Carmelo, L. M. Martelo, and K. Penc, *Nucl. Phys. B* **737**, 237 (2006).
- [61] R. J. Baxter, *Exactly Solved Models of Statistical Mechanics* (Academic Press, New York, 1982).
- [62] V. E. Korepin, A. G. Izergin, and N. M. Bogoliubov, *Quantum Inverse Scattering Method and Correlation Functions* (Cambridge University Press, Cambridge, 1993).
- [63] M. Takahashi, *Thermodynamics of One-Dimensional Solvable Models* (Cambridge University Press, Cambridge, 1999).
- [64] P. B. Wiegmann, *Phys. Rev. Lett* **60**, 821 (1988).
- [65] J. M. P. Carmelo, K. Penc, and D. Bozi, *Nucl. Phys. B* **725**, 421 (2005).
- [66] J. M. P. Carmelo, K. Penc, and D. Bozi, *Nucl. Phys. B* **737**, 351 (2006).
- [67] J. M. P. Carmelo, , and K. Penc, *Eur. Phys. J. B* **51**, 477 (2006).
- [68] F. Bloch, *Z. Phys.* **52**, 555 (1929).
- [69] C. Zener, *Proc. R. Soc. London A* **145**, 523 (1934).
- [70] M. B. Dahan, E. Peik, J. Reichel, Y. Castin, and C. Salomon, *Phys. Rev. Lett.* **76**, 4508 (1996).
- [71] R. Morandotti, U. Peschel, J. S. Aitchison, H. S. Eisenberg, and Y. Silberberg, *Phys. Rev. Lett.* **83**, 4756 (1999).
- [72] S. Söffing, I. Schneider, and S. Eggert, <http://arxiv.org/abs/1204.0003> (2012).
- [73] T. Giamarchi and H. J. Schulz, *Phys. Rev. B* **39**, 4620 (1989).
- [74] I. Affleck, D. Gepner, H. J. Schulz, and T. Ziman, *Phys. A* **22**, 511 (1989).
- [75] W. H. Press, B. P. Flannery, S. A. Teukolsky, and W. T. Vetterling, *Numerical Recipes: The Art of Scientific Computing* (Cambridge University Press, New York, 1986).



# Acknowledgments

Firstly, I would like to thank Prof. Dr. Alejandro Muramatsu for his excellent mentoring, support and patience throughout my PhD work and for giving me the opportunity to come to Germany to work with him. I really appreciate that.

Secondly, I would like to thank Prof. José Carmelo for his help and very important collaboration concerning the Bethe-Ansatz solution.

I would like to thank our secretary, Ms. Ildiko Poljak, for her pleasant conversations and for offering me her support in all sort of bureaucratic issues (especially for taking care of the Reisekostenabrechnung).

I would like to thank my future wife, Mihaela Marchis, for accompanying me in the good and bad moments and giving me help and advice.

Although they are not here physically, I would like to thank my parents, Mireya and Alex, for supporting me during all my life.

I would like to thank all people that directly or indirectly have contributed during the development of this work.

I would like to thank to my friends, Fernando Marino, Zi Yang Meng and Mohammad Rezai, for our fruitful conversations about physics and philosophy.

I would like to thank the SFB/TRR21 for the financial support and the HLRS Stuttgart and the NIC Jülich supercomputer centers for the allocation of CPU time.

At last but not at least, I would like to thank all people of our institute for their friendly discussions, especially during the lunch and coffee breaks.



# Curriculum Vitae

Surname: Moreno

First name: Alexander

Nationality: Venezuelan

Date of birth: November 16<sup>th</sup>, 1981

Place of birth: Caracas, Venezuela

Marital status: unmarried

1994-1999: High school: U. E. Teresiano school. Guacara. Venezuela.

1999-2005: Diploma at the Simón Bolívar University (USB). Caracas, Venezuela.

Diploma work: *Non-linear Models in Econophysics*.

Publication: Journal of Bifurcation and Chaos, Vol **16**, n° 10, 2006.

Supervisors: Prof. Luis E. Guerrero (USB) and Jorge A. González (Instituto Venezolano de Investigaciones Científicas).

2006-2008: Master of Science at the University of Stuttgart. Stuttgart, Germany.

Master thesis: *Ground State Properties of the 1D t-J model with DMRG*.

Supervisor: Prof. Dr. Alejandro Muramatsu (University of Stuttgart).

2008-2013: PhD work at the University of Stuttgart. Stuttgart, Germany.

*Charge and Spin Fractionalization in Strongly Correlated 1D Systems*.

Publications: Phys. Rev. B **87**, 075101 (2013); Phys. Rev. B **83**, 205113 (2011).

Supervisor: Prof. Dr. Alejandro Muramatsu (University of Stuttgart).